Structure and Electronic Gap State Density at Organic Semiconductor Interfaces

Dissertation
der Mathematisch-Naturwissenschaftlichen Fakultät
der Eberhard Karls Universität Tübingen
zur Erlangung des Grades eines
Doktors der Naturwissenschaften
(Dr. rer. nat)

vorgelegt von
Jan Hagenlocher
aus
Kirchheim u.T.

Tübingen
2021

Gedruckt mit Genehmigung der Mathematisch-Naturwissenschaftlichen Fakultät der Eberhard Karls Universität Tübingen.

Tag der mündlichen Qualifikation:	03.02.2023
Dekan:	Prof. Dr. Thilo Stehle
1. Berichterstatter:	Prof. Dr. Frank Schreiber
2. Berichterstatter:	apl. Prof. Dr. Heiko Peisert

Deutsche Zusammenfassung

Die letzten Jahrzehnte waren Zeuge eines beträchtlichen Forschungsaufwands in der Materialwissenschaft der organischen Halbleiter, welcher zu einem enormen Fortschritt im Bereich der organischen elektronischen Bauteile geführt hat. Hocheffiziente organische Leuchtdioden (OLEDs) haben Marktreife erreicht und sind dabei, der Standard in der Displaytechnologie zu werden. Auch organische Photovoltaikzellen (OPVs) eröffnen einzigartige Vorteile gegenüber ihren anorganischen Gegenstücken. Besonders die Möglichkeit chemisch die strukturellen, optischen und elektronischen Eigenschaften den Bedürfnissen anzupassen, macht organischen Halbleiter auch in Zukunft zu vielversprechenden Materialien für verschiedenste (opto-)elektronische Anwendungen.
Während frühe Bauteile aus nur einer aktiven Lage zwischen zwei Elektroden aufgebaut waren, weisen moderne und effizientere Bauteile mehrere übereinandergeschichtete Lagen verschiedener organischer Materialien auf. Die Funktionalität dieser komplexen Heterostrukturen leitet sich großteils von der relativen Angleichung der Energie von Molekülorbitalen einer Lage in Beziehung zur Molekülorbitalenergie in allen anderen ab. Dabei spielen besonders die Energien der höchsten besetzten Orbitale (HOMOs, engl.: *highest occupied molecular orbitals*) und die der niedrigsten unbesetzten Orbitale (LUMOs, engl.: *lowest unoccupied molecular orbitals*) eine Rolle. Trotz der signifikanten Relevanz für technologische Anwedungen und trotz des ungebrochenen wissenschaftlichen Interesses, fehlt bis heute ein Modell, welches diese Energieniveauanpassung an organischen Grenzflächen zuverlässig und quantitativ vorhersagen kann.
Ein Grund für die komplizierten elektronischen Eigenschaften organischer Materialien im Allgemeinen und für Heterostrukturen im Besonderen liegt in ihrer strukturellen Komplexität. Organische Moleküle bilden meist polykristalline Filme, in denen die Bestandteile durch relativ schwache van-der-Waals-Wechselwirkungen zusammengehalten werden. Zusammen mit der anisotropen molekularen Form führt dies zu Dünnfilmstrukturen und Filmmorphologien, welche hochgradig anisotrop sind und vom Substrat, sowie von den gewählten Wachstumsgegebenheiten abhängen.
Vor einigen Jahren wurde ein Modell, welches die strukturellen Eigenschaften - besonders im Hinblick auf die strukturellen Defekte der Filme - mit der elektronischen Energieniveauangleichung in Verbindung bringt, vorgeschlagen. Verantwortlich für eine Verschiebung sind dabei zusätzliche elektronische Zustände innerhalb der Energielücke zwischen HOMO und LUMO. Diese sogenannten Lückenzustände (engl. *gap states*) entstehen dabei durch kleine Abweichungen der Moleküle aus ihrer optimalen Lage,

welche die Energielandschaft empfindlich stören können. Abhängig von der relativen Position der HOMO- und LUMO-Niveaus, sowie der dazugehörigen Lückenzustandsdichte zur Fermienergie des Substrates werden Elektronen entweder zum oder vom Substrat übertragen und führen zu den oben beschriebenen Verschiebungen der Energieniveaus. Da die Lückenzustandsdichte mit strukturellen Parametern korreliert ist, lassen sich also auf diesem Wege elektronische Eigenschaften kontrollieren.
Der spezifische Ursprung der Lückenzustände und ihre Auswirkung auf die Energieniveauangleichung in organischen Dünnfilmen einzelner Komponenten sowie in komplexeren (planaren) Heterostrukturen ist das Hauptthema dieser Arbeit.
Im Folgenden wird ein kurzer Überblick über die Inhalte gegeben. Kapitel eins beinhaltet eine Einführung in die, für das Verständnis dieser Arbeit, relevanten Themen und Zusammenhänge. Im zweiten Kapitel werden die wichtigsten Aspekte der Theorie der organischen Halbleiter, ihre elektronischen Eigenschaften sowie Überlegungen zum kontrollierten Filmwachstum vorgestellt. Kapitel drei und vier beinhalten die Beschreibung der verwendeten Materialien und die eingesetzten experimentellen Methoden. Das fünfte Kapitel umfasst die Ergebnisse und Erkentnisse, welche im Rahmen dieser Arbeit gewonnen werden konnten. Diese sind wie folgt organisiert:

- *Kapitel 5.1.1 Studie zur strukturellen Herkunft der Lückenzustände in organischen Halbleitern.* Jeweils vier prototypische organische Halbleiter werden bei unterschiedlichen Substrattemperaturen (Tieftemperatur, Raumtemperatur und Hochtemperatur) durch molekulare Gasphasenabscheidung aufgebracht. Strukturelle Defekte werden je nach Größenordnung und Wirkungsrichtung unterschieden und durch eine Kombination verschiedener Röntgenstrukturuntersuchungsmethoden sowie Messungen mit einem Rasterkraftmikroskop genauer untersucht. Die Ergebnisse werden mit der erhaltenen Dichte der Lückenzustände aus hochsensitiven Ultraviolettphotoelektronenspektroskopiemessungen verglichen. Es lässt sich ein Zusammenhang zwischen der Dichte der elektronischen Zustände und der Dichte der in der Ebene wirkenden Defekte herstellen.

- *Kapitel 5.1.2 Lückenzustände induziert durch strukturelle Dotierung.* In diesem Kapitel wird die Defektdichte durch die Mischung zweier sterisch kompatibler Moleküle ([5]- und [6]Phenacene) kontrolliert. Diese vermischen sich auf molekularer Ebene und bilden einen Mischkristall mit statistischer Besetzung, dabei werden Punktdefekte induziert. Auch in diesem System lässt sich ein Zusammenhang zwischen Defektdichte und Lückenzustandsdichte finden.

- *Kapitel 5.2 Lückenzustände und die Energieniveauangleichung in Heterostrukturen.* Organische Heterostrukturen verschiedener Donor-Akzeptor-Kombinationen werden untersucht. Durch die Variation der Substrattemperatur während des Wachstums der unteren Lage kann der Grad der Kristallinität der unteren und,

durch einen Templatingeffekt, der oberen Lage kontrolliert werden. Die beobachtete Verschiebung der Energieniveaus korreliert mit der Lückenzustandsdichte und der Austrittsarbeit der unteren Lage, da beide Eigenschaften definieren, wie viele Ladungsträger übertragen werden. Außerdem wird die Herkunft der transferierten Ladungsträger genauer untersucht.

- *Kapitel 5.3 Dickenabhängige Energieniveauangleichung in [6]Phenacene/PFP Heterostrukturen.* Im letzten Ergebnisskapitel wird der Einfluss der Orientierung der Moleküle und der Lückenzustandsdichte in Heterostrukturen mit [6]Phenacene und PFP dickenabhängig untersucht. Dafür werden Echtzeitröntgenmessungen mit inkrementellen Photoelektronenspektroskopiemessungen kombiniert, um einen umfassenden Einblick in die Struktur und elektronischen Eigenschaften vom Beginn bis zum Ende des Wachstums der Heterostruktur zu bekommen.

Kapitel sechs fasst die Ergebnisse der Arbeit zusammen und gibt einen Ausblick auf sich ergebende Fragestellungen und Implikationen für die Anwendung in optoelektronischen Bauteilen.

Contents

Deutsche Zusammenfassung i

1 Motivation and Outline 1

2 Fundamental Concepts 7
2.1 Electronic structure and interface energetics . . . 7
2.1.1 π-conjugation and molecular orbitals . . . 9
2.1.2 Electronic structure of organic thin films . . . 11
2.1.2.1 Effect of disorder on the state distribution . . . 12
2.1.3 Interface energetics and energy-level alignment . . . 18
2.1.4 Electrostatic model of the ELA . . . 21
2.1.4.1 ELA at the organic-organic heterointerface . . . 25
2.2 Electronic investigation: photoelectron spectroscopy . . . 27
2.3 Growth and structure formation of organic thin films . . . 29
2.3.1 Intermolecular interactions . . . 29
2.3.2 Equilibrium considerations . . . 29
2.3.3 Dynamical description of growth . . . 31

3 Materials 35
3.1 Pentacene (PEN) . . . 35
3.2 Perfluoropentacene (PFP) . . . 36
3.3 Buckminsterfullerene (C60) . . . 37
3.4 [5]- and [6]Phenacene . . . 38
3.5 α-Sexithiophene (6T) . . . 39
3.6 Substrate . . . 40

4 Experimental methods and techniques 41
4.1 Sample preparation . . . 41
4.1.1 Procedure for substrate cleaning and preparation . . . 41
4.1.2 Organic molecular beam deposition . . . 41
4.1.3 Ultra-high vacuum . . . 43
4.2 X-ray scattering and organic thin films . . . 43
4.2.1 X-ray diffraction . . . 44
4.2.2 X-ray reflectivity . . . 45

4.2.3 Rocking scans . . . 48
4.2.4 Grazing incidence X-ray diffraction . . . 48
4.2.5 X-ray sources and experimental setup . . . 50
4.2.6 X-ray scattering experiments in situ and in real-time . . . 50
4.3 Atomic force microscopy . . . 51
4.4 Ultraviolet photoelectron spectroscopy . . . 53
4.4.1 Experimental setup at the Institute for Molecular Science, Okazaki, Japan . . . 53
4.4.2 Experimental setup at Soochow University, China . . . 54

5 Results and Discussion 55
5.1 On the origin of gap states in molecular semiconductors . . . 56
5.1.1 Gap states induced by temperature variation . . . 57
5.1.1.1 Structural characterization . . . 58
5.1.1.2 Structural defects . . . 63
5.1.1.3 Electronic properties - gap state density and ELA . . . 70
5.1.1.4 Summary and conclusion . . . 75
5.1.2 Gap states induced by structural doping . . . 77
5.1.2.1 Structural properties . . . 78
5.1.2.2 Electronic properties . . . 82
5.1.2.3 Summary and conclusion . . . 85
5.2 Gap states and energy-level alignment in heterostructures . . . 86
5.2.1 PFP and C60 as top layer . . . 88
5.2.1.1 Structural characterization and in-plane defects . . . 88
5.2.1.2 Electronic properties of PFP/C60 on donor molecules . 91
5.2.1.3 Energy-level alignment of top acceptor layers . . . 94
5.2.1.4 Summary and Conclusion . . . 97
5.2.2 PFP as bottom layer . . . 99
5.2.2.1 Structural characterization . . . 99
5.2.2.2 Electronic properties and ELA . . . 100
5.2.2.3 Summary and conclusion . . . 102
5.3 Thickness-dependent energy-level alignment in [6]Phenacene/PFP heterostructures . . . 103
5.3.1 Structural characterization . . . 103
5.3.2 Thickness-dependent electronic structure . . . 108
5.3.2.1 [6]Phenacene . . . 108
5.3.2.2 PFP on [6]Phenacene . . . 109
5.3.3 Summary and conclusion . . . 112

6 Conclusion and Outlook 115
6.1 Results on the origin of gap states . . . 115

6.2 Results on the energy-level alignment in organic heterostructures 116
6.3 Results on the thickness-dependent energy-level alignment in heterostructures 117
6.4 Outlook 118

Acronyms **120**

List of contributions **122**

Publications **123**

Acknowledgements **127**

1 Motivation and Outline

Since the first description of electronic conductivity in organic molecules, the field of organic electronics has been remarkably prolific and seen steady development leading to an ever-increasing number of applications and devices [1, 2]. Today, available devices range from fully functional organic light emitting diodes (OLEDs) [3–5], field effect transistors (OFETs) [6–8], photovoltaic cells (OPVs) [9–11], memory cells [12, 13] and various sensing devices [14–16], which have been demonstrated and, partly, are well-established in the consumer market. The benefits of using organic semiconductors (OSCs) as an alternatives to their inorganic counterparts include their light weight, flexibility and a low cost thin film fabrication process, e.g. simple vacuum sublimation, inkjet-printing or spin-coating [17–19]. Additionally, the chemically tunability allows to control the electronic and structural properties which is especially attractive for device design [20] as the use of a particular molecular moiety and/or combinations of organic molecules allows the realization of materials with defined functions and ranges of use [21, 22].

While the composition of early devices featured only one or two organic layers deposited on and between conducting electrodes, modern devices architectures often exhibit multiple layers [25–27]. Each layer in such a heterostructure is characterised by the energies of the so-called frontier molecular orbitals and is attributed a specific function that derives mainly from the energy level positions relative to those in all other layers [28, 29]. Depending on the selection of organic compounds and their respective orbital energies, transport, blocking or confinement layers may be formed [30]. As an example, a typical OLED is shown in Fig.1.1(a), where the electron and hole transport layers (ETL/HTL) are in direct contact with the electrodes and the emission layer (EL) is sandwiched between them. Upon applying an external driving voltage, charge carriers (i.e. electrons and holes) are injected into the ETL and HTL and meet in the center, where they radiatively recombine and photons are emitted. For the device to work efficiently, the highest occupied molecular orbital (HOMO) of the ETL should lie at a lower energy than the HOMO of the emitter material and, inversely, the lowest unoccupied molecular orbital (LUMO) should ideally lie above the LUMO in the emitter material for the HTL. As a result, a driving force for both charge carriers to accumulate preferentially in the EL is imposed. Moreover, the fundamental gaps, that is, the energy distance between HOMO and LUMO in the transport layers should be picked to exceed that of the EL. Doing so, one ensures that the charges injected from one electrode are not able to reach

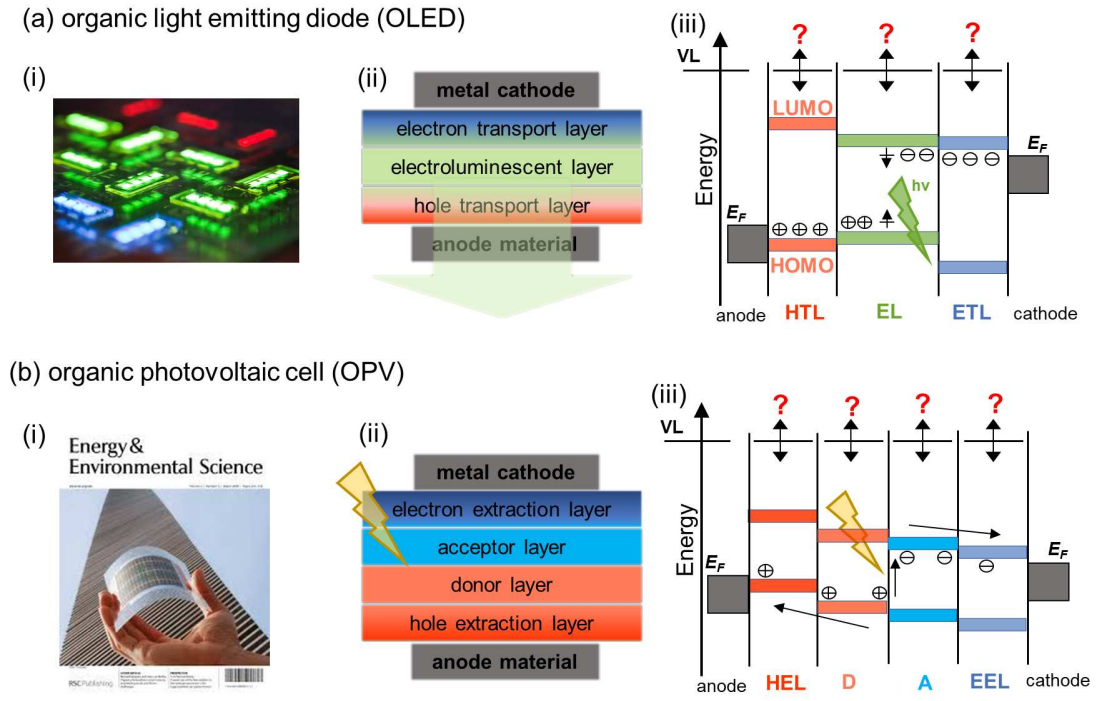

Figure 1.1: (a) Organic light emitting diodes (OLEDs) as well as (b) organic photovoltaic cells (OPVs) have reached marketability and are available on the consumer market. The middle column (ii) shows the device architecture consisting of multiple layers each with a specific function. (iii) shows the structure from an energy point of view. Depending on the HOMO and LUMO positions energy barriers between the respective layers arise which define the functionality and efficiency of the device. The energy-level alignment, that is the vacuum level shift indicated as red question marks, is ultimately responsible for the exact height of said energy barriers. In this thesis the energy-level alignment is explained within the gap state picture, where a small density of electronic states within the electronic gap (between the HOMO and LUMO level) arises due to structural imperfections in the organic thin film. This offers the intriguing possibility to investigate the connection between structural parameters and electronic properties. Figures adopted from [9, 23, 24]

the opposing electrode and excitons (bound electron-hole pairs), which are formed in the EL are hindered to diffuse to either side and recombine non-radiatively.
Also in the case of a typical OPV, as shown in Fig. 1.1 (b), the energies of the HOMO/LUMO states are of fundamental importance [31]. While the two outer materials in this case serve as hole- and electron extraction layers (HEL/EEL), the frontier orbitals in the acceptor have to at a lower energy than these in the donor material to split the excitons into free charge carriers at this interface. To impose a driving force and effectively collect the free charges, the HOMO in the HEL should lie energetically above the ones in the donor material and the LUMO of the EHL should lie below those in an acceptor.

The two examples highlight the importance of the relative position of energy levels at the inorganic/organic as well as at the organic/organic interface. In device optimisation, the choice of material frequently follows the assumption that, after the deposition of an OSC layer on top of another, the vacuum level (VL), that is, the potential energy of an electron far away from the surface, stays constant [32]. With the knowledge of the individual frontier orbital energies of each material, this would imply that the entire energy-level setting in a multicomponent stack can be obtained by simple alignment of the HOMO/LUMO levels of all components to this constant VL [33]. However, a lot of experimental data - often from ultraviolet photoelectron spectroscopy (UPS) - and theoretical calculations point towards the fact that the assumption of VL alignment can generally not be hold and VL shifts of up to $\pm 1.0\,\mathrm{eV}$ are observed across a given interface (indicated by the red question mark in Fig. 1.1) [34–36].
Inconveniently, these deviations translate into relative shifts of the same magnitude between the frontier orbital energies of the OSCs and thereby compromising the interface functionalities introduced above. To achieve a genuine knowledge-based device and materials design, it is clear that a thorough understanding of the fundamental causes for the occurrence or absence of those shifts is needed. However, a comprehensive framework able to predict the sign and magnitude of this energy-level alignment (ELA) for any given set of materials is still elusive. Even despite the evident technological relevance and a large amount of case studies in literature [37–39].
So far, several models based on different approaches have been developed to explain the phenomenon [40, 41]. However, they often differ in the applicable regimes of electronic interaction strength between organic material and/or electrode (from relative weakly interacting passivated electrodes to coupling with atomically clean metal surfaces [42, 43]), their intended range of film properties (from only one OSC layer (monolayer) to thicker films [44, 45]) and also in the presumed distribution of electronic states in the organic material (from discrete states to continuous state distribution [42, 46]).
A reason for the complex electronic properties of organic materials in general and for heterostructures in particular lies in their structural complexity [47]. Organic compounds form mostly polycrystalline films due to the relatively weak van der Waals interaction [48]. Together with their anisotropic molecular shape this leads to a thin film structure and morphology, which is highly anisotropic and depends crucially on the substrate as well as the growth conditions [49].

In recent years, Bussolotti et al. developed a model connecting structural properties - in terms of structural disorder - with the alignment offset between different materials [50–52]. As proposed, a density of additional electronic states within the gap between the HOMO and LUMO levels (and therefore termed *gap states*) arises due to the effect of small deviations in the precise energetic landscape surrounding a specific molecule. Depending on the position of the HOMO or LUMO distribution relative to the substrates

Fermi energy, charges can be transferred from or to the organic layer, resulting in the above described energy level shifts. Since the density of gap states is correlated with structural parameters, in this way, electronic properties can be tailored by controlling structural properties [53].

The specific origin (in terms of different kinds of structural defects) of gap states as well as their impact on the energy-level alignment in single component and the more complex (planar) heterostructures is the main topic of this thesis. In the first part, the fundamental concepts needed for the description of electronic properties and the energy-level alignment will be introduced, with an emphasis on the connection between structural defects and their impact on the HOMO/LUMO state distribution. Additionally, the mechanisms regarding thin film growth and parameters controlling the film quality are discussed. The second and third part are dedicated to the specific materials and the experimental techniques used for the investigation of structural properties (X-ray techniques and atomic force microscopy) and electronic properties (photoelectron spectroscopy). In the fourth chapter the results are presented and discussed.

2 Fundamental Concepts

The following chapter provides the theoretical basis for the involved processes and concepts underlying this work. In the first part, an introduction to the electronic properties of organic compounds in general and organic thin films in particular is given. A main focus lies on the the impact of structural defects on the electronic properties, namely the gap state density. Additionally, the processes and mechanisms responsible for energy-level alignment of organic thin films at different interfaces are introduced. They are mainly based on electrostatic considerations, in which an varied gap state density can be easily included. The last part focuses on the static and dynamic considerations regarding the growth and structure formation of organic thin films and heterostructures and how structural parameters, such as the defect density, can be controlled. For a general introduction to OSCs, the reader is referred to Refs. [54–56].

2.1 Electronic structure and interface energetics

OSCs are materials that show properties typically associated with semiconducting materials. In general, this means absorption and emission of photons in the visible spectral range as well as a degree of conductivity sufficient for their use in conventional semiconductor devices, such as LEDs, solar cells or field effect transistors [8, 57]. However, the origin and nature of the semiconducting behaviour differs between organic and inorganic semiconductors [58].
Since conventional inorganic semiconductors have rather small band gaps (e.g.1.1 eV for silicon and 0.67 eV for germanium [59]), free charges may be created already at room temperature by thermal excitation. For their organic counterparts the electronic gap lies typically in the range of 2-3 eV, which inhibits any significant charge-carrier concentration to be created by thermal excitation (at least at room temperature), making them technically insulators [60]. Only when charge carriers are injected from electrodes, generated by doping or from the dissociation of photo-generated electron-hole pairs they are showing semiconducting behaviour [61]. Additionally, due to a low dielectric constant ($\epsilon_r \sim 3.5$), even for electron-hole pairs created by optical excitation, Coulomb interactions are significant and electrons and holes are bound with a Coulomb energy of 0.5-1.0 eV. This impedes an efficient photo-generation of free charge carriers, which can only take

place at an efficient rate in binary systems as a result of a charge transfer between donor and acceptor molecules at their respective interface [62].

Despite some drawbacks, organic materials offer properties that makes them superior to inorganic semiconductors in certain areas of application. Besides the more complex possibility to chemically tailor the electronic and structural properties, this includes the possibility to apply OSC materials on flexible substrates while inorganic semiconductors are mostly limited to be used on rigid bases [1, 63]. In general three different classes of organic solids can be distinguished:

- **Amorphous films** include solids consisting of small organic molecules that are deposited through evaporation or spin-coating. They show neither short- nor long-range order, with molecules that are randomly distributed on the substrate and are mostly employed for device applications such as LEDs or in xerography (dry photocopying technique) [64].

- **Molecular (poly-)crystalline films** are solids consisting of a lattice and a basis. Similarly to atoms, molecules can form the basis of a crystal that is, in this case, held together by comparably weak van der Waals-interactions. Compared to non-crystalline organic materials, the charge mobilities that can be obtained in molecular crystals are considerably higher [65, 66].

- **Polymer films** may be included for the sake of a complete overview. They consist of small monomers that are covalently coupled and distinguishes them from small molecules. They are often applied from solution, deposition techniques include ink-jet printing or spin-coating [67].

While the constituents of the different classes differ in molecular mass, size and solubility, they are all build up of mostly carbon and hydrogen atoms with the exception of a few heteroatoms such as oxygen, fluorine or nitrogen (among others). This leads to the semiconducting properties having a similar origin, namely a π-conjugated system, which is introduced in the following section.

2.1.1 π-conjugation and molecular orbitals

Characteristic for the organic materials used in organic electronic are alternating single and double bonds between adjacent carbon atoms, i.e. conjugation [68]. Conjugation can be understood as a result of sp^2-hybridized carbon atoms (see Fig. 2.1 (a)). Carbon, in its ground state, has four valence electrons, two of which are occupying the $2s$-orbital and two are in the three energetically higher lying $2p$-orbitals. As soon as a binding partner approaches, i.e. carbon not being in its elementary form, the energy difference between the $2s$- and the $2p$-orbitals is compensated rendering them degenerate [55]. Depending on the number of participating atomic orbitals, up to four *hybrid orbitals* are formed from a linear combination of $2s$- and $2p$-orbitals [69].

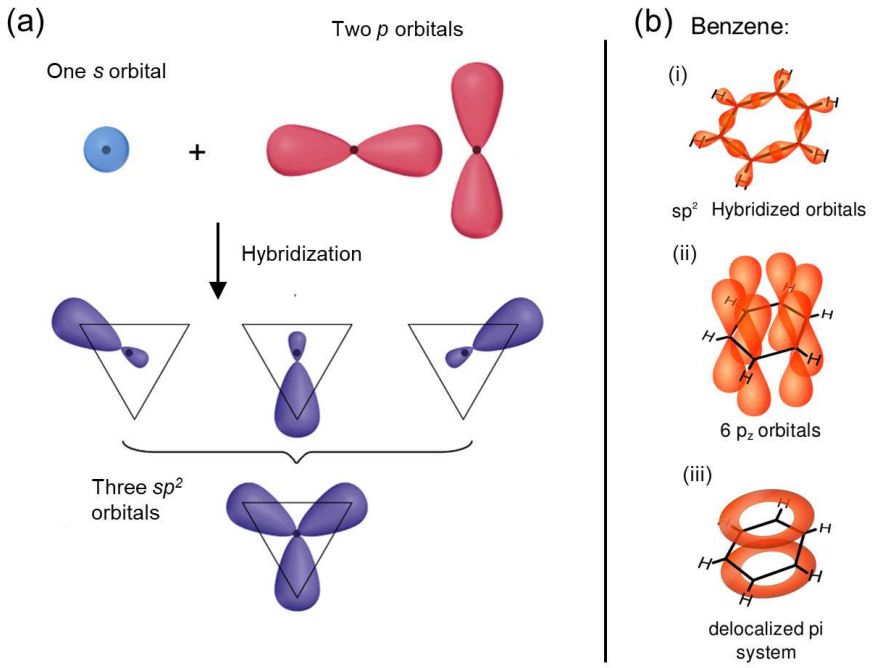

Figure 2.1: Origin of the π-conjugated system in OSCs. (a) sp^2-hybridzation arises from a combination of one $2s$ and two $2p$ orbitals. As a result, three in-plane sp^2 orbitals, oriented with an angle 120 ° between one another are obtained. The p_z orbital oriented in the out-of-plane direction remains unaltered. (b) π-bond formation, exemplarily shown in benzene. The sp^2 orbitals engage in σ-bonds between adjacent carbon atoms and the hydrogen atoms (i), leaving the p_z-orbital free (ii) to contribute to a π-bond connecting to the surrounding atoms. Consequently, the π-electrons are delocalized over the entire molecule (iii). If the molecule is in its ground state, all bonding orbitals are filled, setting a highest occupied molecular orbital (HOMO) and a lowest unocuppied orbital (LUMO). Most of the optical and electronic properties of OSCs are determined by the energy distance between HOMO and LUMO. Figure adopted from [70]

As shown in Fig. 2.1 (b), sp^2-hybridization (from the combination of the $2s$- and two

2p-orbitals) yields three covalent σ-bonds oriented within a plane, leaving the remaining p_z-orbital free to overlap with the p_z-orbital of an adjacent carbon atom, resulting in the formation of a π-bond. From linear combination of atomic orbitals (LCAO) the *molecular orbitals* of a given molecule are derived, which describe the electron distribution over the complete molecular entity.

Since they are the defining parameter for many optical and electronic protperties, two of the molecular orbitals are of special interest: the highest occupied molecular orbital (HOMO) and lowest unoccupied molecular orbital (LUMO). Generally, they are given by π-bonding orbitals and π^*-antibonding orbitals, respectively. HOMO and LUMO are often called the *frontier orbitals* since their energy difference defines the molecular gap. On an energy scale, HOMO and LUMO can be characterized by the ionization energy (IE), that is, the energy required to bring an electron from the HOMO to the vacuum level (VL) and, conversely, the electron affinity (EA), that is the energy gained when bringing an electron from the VL into the LUMO. The VL is thereby defined as a universal energetic reference level, i.e. the energy of an electron located infinitely far away from the system. [1] For π-bonded molecules in the gas phase, the IE is generally in the order of 8$\pm$2 eV [71] and depends mainly on the size of the π-electron distribution. For example, in the series benzene (one ring of six carbon atoms) to pentacene (five linearly fused rings), it decreases from 9.2 to 6.7 eV.

Electrons can be promoted from the HOMO to the LUMO if they are given the energy of the gap (E_{gap}). Since bonds formed by the σ-orbitals are considerably stronger than the π-bonds, molecules are not breaking apart when the antibonding π^*-orbitals become populated.

The molecular π-systems are also actively involved in intermolecular interactions, which are mainly dominated by comparably weak van der Waals-forces. This has important implications for the stability of molecular solids and makes them particularly prone to structural defects since displacements and dislocations only require a small energy expenditure. Furthermore, an electron-hole pair, created by optical excitation of a conjugated system, is usually localized within the same molecule. This limits the charge mobility significantly, which, in most cases, happens through hopping processes from one molecule to another and only weakly through a band-like transport known from inorganic semiconductors [72]. The hopping mechanism in OSCs depends mainly on the degree of $\pi - \pi$ overlap between adjacent molecules and will be significantly more efficient if molecules are facing each other [60]. In the following, the electronic structure of a molecular solid consisting of small OSCs is derived, in which structural properties play a key role.

[1] One has to keep in mind that molecular orbitals derived from LCAO are based on one-electron orbitals. Any electron correlation is neglected and experimentally obtained energies for HOMO and LUMO deviate from the ones calculated on this (one-electron) basis.

2.1.2 Electronic structure of organic thin films

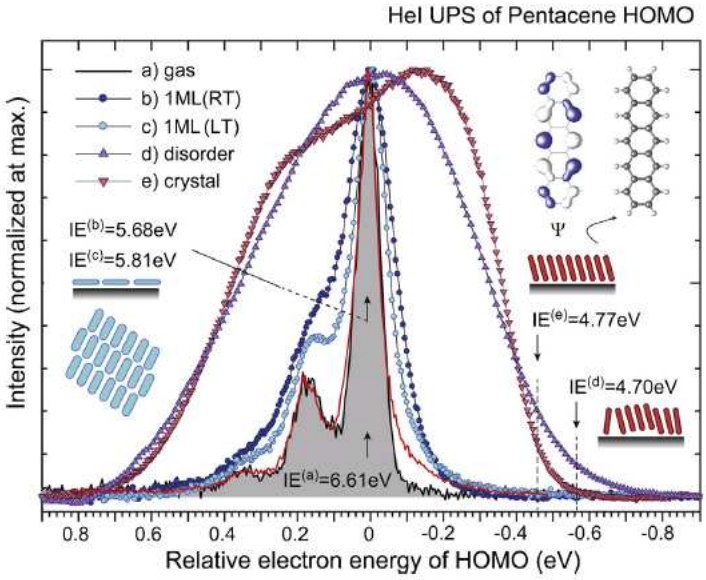

Figure 2.2: Ultraviolet photoelectron spectroscopy (UPS) data for various phases of pentacene. In the monolayer regime ((b) and (c)), the gas phase features are relatively well preserved and the HOMO width is only slightly increased. However, for a film thickness relevant for applications ($\sim 20\,\mathrm{nm}$), the HOMO width is significantly broadened. While, at least for a perfect crystal (e), this can be partly ascribed to an band-like electronic structure formation, newer models highlight the interplay between structural disorder (d) and the broadening of the HOMO distribution. Picture taken from [73].

In the first descriptions of electronic properties in organic thin films, the characteristics of the contained molecules were expected to be preserved due to the only small interactions between them [74–76]. However, as the development of investigation techniques progressed, as shown in Fig. 2.2, this assumption can not be held, particularly for the transition to a film thickness above the monolayer regime. While the HOMO energy distribution is well-defined in the gas phase (a) and in the monolayer samples ((b) and (c)), where even some distinct low energy features are preserved, the distribution is significantly different and broadened for a film thickness of 20 nm ((d) and (e)). Several effects contribute to the increased HOMO width. Probably the most trivial and obvious being the band structure of crystalline parts which also results in the two features in spectrum (e), from bands formed by the two molecules in the unit cell [77]. More recent models, however, based on a combination of quantum and classical dynamic concepts, as well as experimental evidence, point towards the fact that the broadening of the distribution of states is strongly intertwined with structural deviations from an ideal crystal structure [78–80].

A very important feature in the framework of this work, is the difference in the density of states reaching into the bandgap (i.e. the density of states at negative energies in Fig. 2.2 (d) and (e)). While the width of HOMO distribution is comparable in terms of the

full width at half maximum (FWHM) for the perfectly ordered crystal (e) and the highly anistropic, disordered film (d), the density of states between -0.4 eV and -0.7 eV differs significantly. Since these states reach into the formerly forbidden gap, they are termed *gap states* and their density, as implied in the figure, can be controlled by changing the amount of structural defects. In the following section the effect of structural disorder on the (gap) state distribution is introduced in greater detail.

2.1.2.1 Effect of disorder on the state distribution

Since individual molecules represent the building blocks of an organic thin film, the weak intermolecular interaction between them as well as the orientational degrees of freedom makes them generally highly susceptible to the formation of local disorder, defects and polymorphic structures [81]. Realizing that the energy of π-electrons in molecular orbitals of a specific molecule largely depends on the transfer integral (that is, the orbital overlap) between neighbouring molecules, it is easily comprehensible that the energy is strongly affected by any structural variation [82, 83]. As a result, the precise energetic landscape of molecules in the vicinity of a deviation is altered and results in the formation of additional electronic states leading to a broadening of the distribution as a whole and states reaching into the electronic gap [84, 85].

Any disorder in the structural domain will necessarily affect the energetic disorder in the energy domain [86], which is commonly modelled with a Gaussian distribution of energy. Within this model, the standard deviation is quantifying the extent of disorder [87, 88]. In a real experiment, the Gaussian shape can be observed as the limiting case for amorphous thin films with completely random distribution of molecules (Fig. 2.2 (d)). In a polycrystalline sample, such as the ones investigated in this work, the situation lies between a fully crystalline and a fully amorphous sample. In this case, the density of states reaching into the gap can be effectively controlled by altering the density of structural defect [45]. In general, the defect density strongly depends on the growth technique, with vapour-grown films typically having a lower defect density compared to samples grown from solution [89].

Possible sources of additional electronic states are summarised in Fig. 2.3. Generally, one distinguishes between extrinsic and intrinsic effects on the state density [78]. Extrinsically induced states may intentionally be introduced by exposure to electromagnetic radiation, treatment with gases, stress induced through temperature gradients, or dopants [90–93]. They can be excluded relatively easily by constant experimental conditions and careful sample preparation. Intrinsic effects, on the other hand, are always apparent [78]. Intrinsic disorder can be further divided into *dynamic* and *static* disorder. Localization of charge carriers may be observed because of dynamic disorder destroying the already narrow electronic energy bands. However, since dynamic disorder lasts only up to the

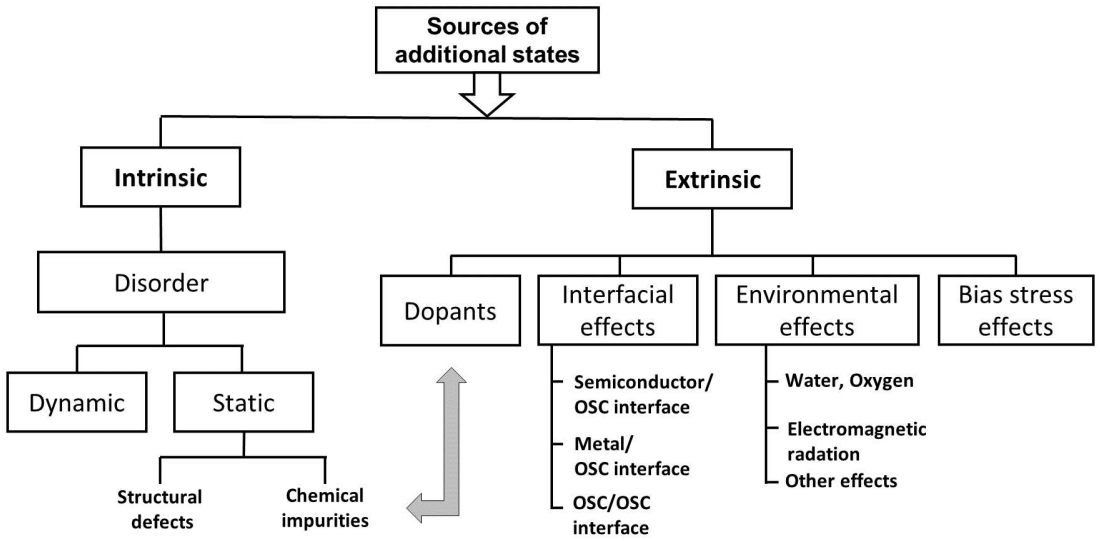

Figure 2.3: Possible origin and sources of additional states leading to the broadening of the HOMO or LUMO density of states. Generally, they can be divided into extrinsic and intrinsic sources. For a systematic study, one has to be careful to only change a minimum of parameters, while keeping the others constant. Extrinsic effects can be relatively easily excluded by keeping the experimental conditions the same and careful sample preparation. In the studies conducted here, a focus lies on the effect of static structural defects on the HOMO and LUMO state distribution, for which, by careful selection of growth parameters, structural defects can be induced or reduced. Modified from [78]

time-scale of the thermal motions the impact on the gap state density can be in large part circumvented by a constant measurement temperature [94]. Static disorder, caused by structural defects and chemical impurities, in contrast, is time-independent and its effect is only apparent at the specific locations where the defects are present [95]. Defects form during or after the crystal formation and their density, as will be shown in a subsequent section, can be effectively controlled by varying growth parameters. Structural imperfections exist in any real crystal and can be categorized depending on the their length scale and orientation [96]. They range from point defects, residing at a specific lattice site (e.g. a vacancy) over extended defects with a range over several lattice site (e.g. dislocation/stacking faults) to the rather large boundaries between individual crystallites or domains [81, 97] and are described in greater detail in the following list:

- **Vacancies and chemical impurities/dopants** can lead to the lattice being expanded or compressed. Generally, states with higher energy arise in regions of the lattice that are compressed. In expanded regions, states with a lower energy can be created around the HOMO or LUMO distribution [78]. Additional states with a broad range of energies can be introduced through the presence of guest molecules (chemical impurities or intentionally added dopants) due to a local distortion of

the lattice or due to energy difference between guest and host molecule. In the case of acene crystals, oxidation can lead to the formation of quinones that act as an chemically inert impurities, but their presence changes polarization energies by locally distorting the lattice [65]. Also, environmental contaminants, e.g. H_2O or O_2 may create discrete states, which necessitates careful sample handling and vacuum conditions [98].

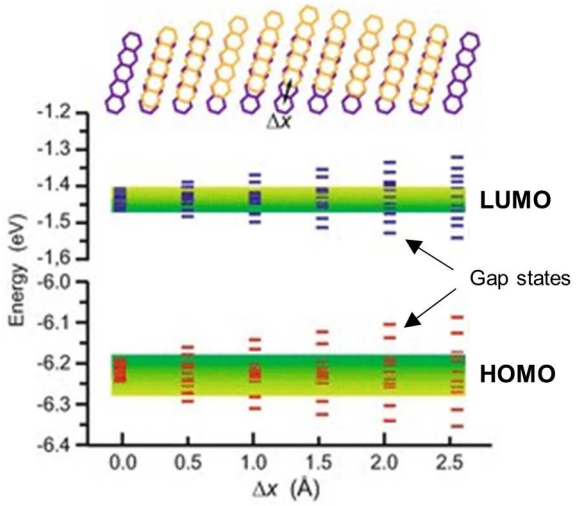

Figure 2.4: The effect of a molecular displacement was studied theoretically by Kang et al.: Molecules are initially positioned at their locations in the single crystal structure with zero displacement (purple color). To model the structure found in defects, they are then displaced (Δx) along their long molecular axis. For zero displacement, the dispersion of the HOMOs and LUMOs can be used to define the defect-free conduction and valence bands (green). It is found that the defect induces the appearance of both, hole and electron levels within the gap. Figure modified from [99].

- **Dislocations** impact the density of states by altering the orbital overlap and thus creating additional states [89, 100]. Shown in Fig.2.4 is the relative shift of an individual pentacene molecule in an ensemble of alike molecules. When a pentacene thin film is grown on a substrate for which the interaction is weak, the molecules nucleate to form "standing up", crystalline layers. Kang et al. performed quantum-chemical calculations to answer the question, whether a sliding defect induces additional states [99]. The molecules were initially placed at their locations in the single crystal structure with zero displacement (purple). By incremental shifting along the long molecular axis with Δx (yellow), the HOMO and LUMO wave function overlaps between adjacent molecules is changed. As a result, additional states appear within the gap, above and below the respective HOMO or LUMO distribution. For a maximum displacement Δx of 2.5 Åthe additional HOMO and LUMO levels in the defect deviate as much as $\sim$100 meV from the corresponding levels in the absence of defects.

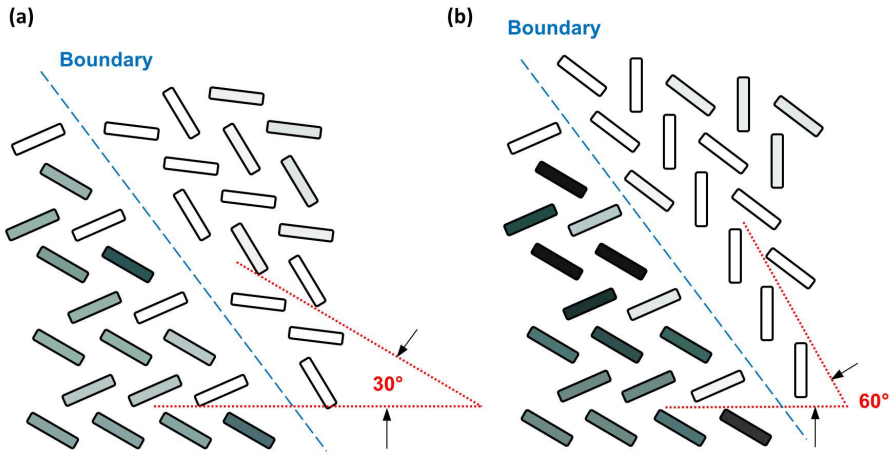

Figure 2.5: Effect of boundaries between crystallites in a pentacene crystal, misaligned by (a) 30° and (b) 60°. The molecules are viewed along their long axis which makes their plane perpendicular to the image plane. The shading marks the energy difference to an undisturbed molecule: states with relative energies below -0.25 eV are marked by dark shading, states with relative energies above 0.25 eV are shaded bright. After Verlaak and Heremans [101].

- **Crystallite boundaries and mosaicity** are common features in OSC thin films. The samples studied in this work mainly grow as a 2-dimensional powder with a random distribution of crystallite orientation *in-plane*, but highly ordered in the *out-of-plane* direction [102]. The in-plane orientation of a crystallite is thereby already determined by the nucleation event and maintained upon the growth of the nucleus [103]. A crystallite continues growing until it meets a neighbouring crystallite, with which it forms a boundary, separating two crystallites with different orientations. A view of two possible situations is depicted in Fig. 2.5. There, the misalignment between crystal directions is set to (a) 30 ° and (b) 60 °. The shading corresponds to the energy difference to an undisturbed molecule. States with, compared to the undisturbed molecules, relative energies below -250 meV are marked by dark shading, states with relative energies above 250 meV are marked bright. The impact of boundaries on electronic properties is based on the weaker electronic coupling between molecules located in the vicinity of a boundary compared to those located inside crystallites [101, 104, 105]. A closely related phenomenon is the so-called *mosaicity* [106]. In a real uniaxial polycrystalline film, the crystallites are slightly skewed and generally show an average tilt with respect to the surface normal. If two adjacent crystallites are, e.g., tilted in different directions, this leads to stronger coupling in the bottom layers but a rather weak coupling in the top layers due to a larger distance between crystallites.

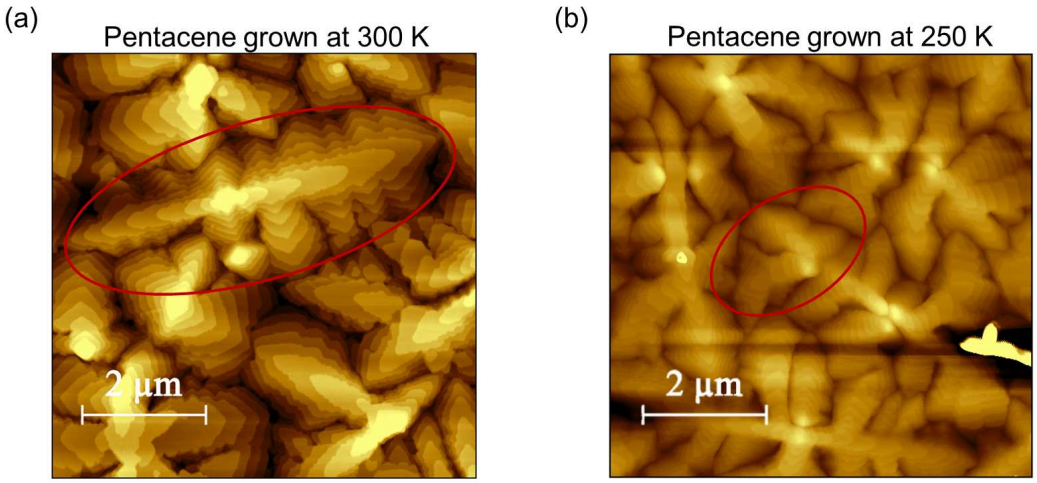

Figure 2.6: Domain boundaries arising between adjacent domains in pentacene thin films, grown at different substrate temperatures. For elevated temperatures, the domains are significantly larger and the boundary length between them is reduced.

- **Domain boundaries** are formed between large scale domains as observed in AFM images and shown in Fig. 2.6. Depending on the substrate temperature during growth, the domains differ in size and become larger at elevated temperatures, for which, correspondingly, the cumulative boundary length becomes smaller [107]. The coupling arguments given above are also valid for boundaries between individual domains, for which additional states result from the altered electronic coupling at the interface compared to the coupling within a domain.

In the vast majority of organic thin films, all described kinds of defects are present. However, their respective density may differ between different films.

2.1.3 Interface energetics and energy-level alignment

The functionality and efficiency of organic devices depends strongly on how charge carriers are able to move and to recombine at different interfaces [28]. The energy barriers emerging at substrate/organic or organic/organic interfaces are therefore a defining parameter for device behaviour and are central to the development of molecular electronics [29, 32]. Understanding and predicting the mechanisms involved in the energy-level alignment (ELA), that is, the shift of energy-levels in order to find a common frame, is hence highly relevant for designing new devices and engineering new functionalities [25, 38]. For example, in OLEDs, efficient charge injection through the electrode is desired; for OPV devices an efficient charge extraction is pursued. In both cases, electrons and holes have to overcome specific energy barriers, which, upon contact, have a common reference at the interface. One of the main obstacles hindering the ability to accurately model and predict the electronic properties of interfaces involving OSCs, is the quantity of different phenomena that may take place at such an interface simultaneously or as a subset and which are summarized in Fig. 2.7.

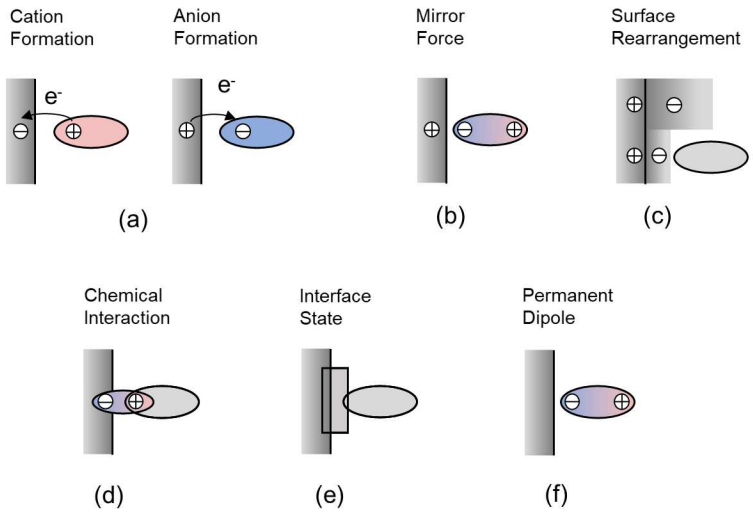

Figure 2.7: Different possible effects leading to an interfacial dipole layer between substrate and OSC. (a) Integer charge transfer across the interface, depending on the transfer direction a cation or anion is formed. (b) shift of charges within the molecule leading to a positive charging of the vacuum side. (c) "Push-back effect" where a rearrangement of the electron cloud at the metal surface is accompanied with a reduction of tailing into the vacuum. (d) formation of a chemical bond due to strong chemical interaction between the surface and the molecules. (e) hybridized interface states serving as a buffer of charge carriers and (f) interface dipole defined by the orientation of polar molecules or functional groups. Figure adapted from [32].

The first effect resulting in an energy-level shift is an electron transfer between the substrate and the organic layer (a), with positive and negative charges separated across the interface. This may be expected for combinations of strong organic acceptor/low work function and strong organic donor/high work function materials as well as at the organic/organic interface leading to the formation of positively or negatively charged molecules. A second factor may be an image effect (b) due to polarization of the electron cloud initiated by an image charge formed in the metal substrate and resulting in the decrease of electrons density at the vacuum side. In (c) a closely related phenomenon is shown, where deposition of organic material leads to the electron cloud of the substrate spilling out into the vacuum being pushed back by Pauli repulsion. For highly reactive substrates, also chemical interaction (d) and specific interface states (e) are possible [108]. Finally, for organic molecules exhibiting a permanent dipole (f), the orientation dipole moment can strongly influence interfacial properties.

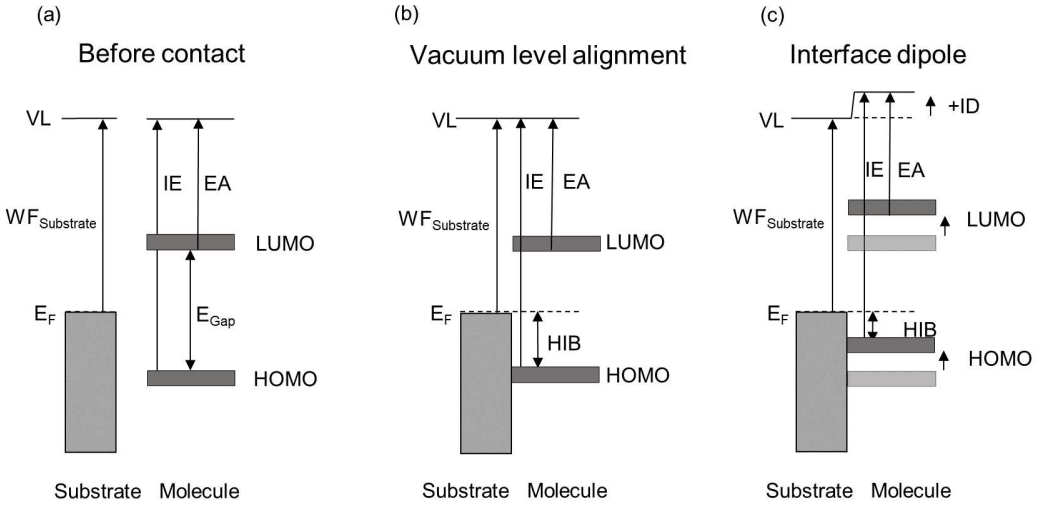

Figure 2.8: Vacuum level alignment or interface dipole after contact. The isolated systems in (a) are characterized by the substrate work function WF_{Sub}, i.e. the energy distance from the Fermi energy E_F to the vacuum level (VL), the ionization energy (IE), that is, the energy distance from the HOMO energy level to VL and the electron affinity (EA, distance from LUMO energy to VL). When brought into contact, two possibilities arise: without any interaction, an alignment according to VL could be expected (also called Schottky-Mott limit). This would imply that by simply knowing the materials parameters, energy barriers (such as the hole injection barrier (HIB) could easily be calculated beforehand. However, in a real experiment, the energy levels often shift as a result of the processes described in Fig. 2.7 and an interface dipole (ID) is observed (c). Since IE and EA stay constant, the energy levels shift accordingly and alter the energy barriers.

To visualize the effect of the different processes on the position of energy levels, the isolated systems without any contact are shown in Fig. 2.8 (a). The substrate is characterized by the energy distance from its Fermi energy (E_F) to the VL, which gives the characteristic substrate work function (WF_{Sub}). For an isolated molecule, the electronic parameters are given by the IE for the HOMO and the EA for the LUMO, respectively. When brought into contact, two possibilities arise: without any interaction, one expects alignment according to the VL (Schottky-Mott limit, (b)). This would conveniently imply that just by knowledge of WF_{Sub}, IE and EA of both materials one could predict how the levels align and energy barriers (e.g. the hole injection barrier (HIB)) arise [109]. However, as a result of the factors described above, a vacuum-level shift, also termed *interface dipole* (ID) is commonly observed. The HOMO and LUMO energy levels shift according to the ID, while IE and EA stay constant which, as a result, alters the height of the HIB [110].

Much to the impairment of device development and improvement, so far, a unifying model taking into account the different interface effects is still elusive [29, 44]. Reduction to a subset of different interface types, sorted by their interaction strength, however, simplifies the situation significantly and models exist that can be applied [37, 111, 112] for specific combinations of materials. In the following, a model particularly suited for the description of the ELA at rather inert interfaces is introduced in more detail.

2.1.4 Electrostatic model of the ELA

A successful model describing the ELA was developed by Oehzelt et al. taking into account electrostatic considerations [46]. It allows various scenarios to be treated on equal footing and, most importantly for the premise of this work, easily incorporates the broadening effect caused by structural defects and an altered gap state density.

As a starting point, a continuous density of states (DOS), both for HOMO and LUMO levels in the OSCs are assumed and modelled with Gaussian peaks. For an unambiguous definition of the Gaussians, the energy position of the maxima, E_H and E_L and the respective standard deviations, σ_H and σ_L, are specified. IE and EA then follow from the energy difference between VL and the respective low-energy or high-energy onsets (see Fig. 2.9 (b)). The substrate is characterised by the work function. The substrate is assumed to be an infinite reservoir of electrons and capable of collecting an infinite amount of electrons without significant changes of $\mathrm{WF_{Sub}}$.

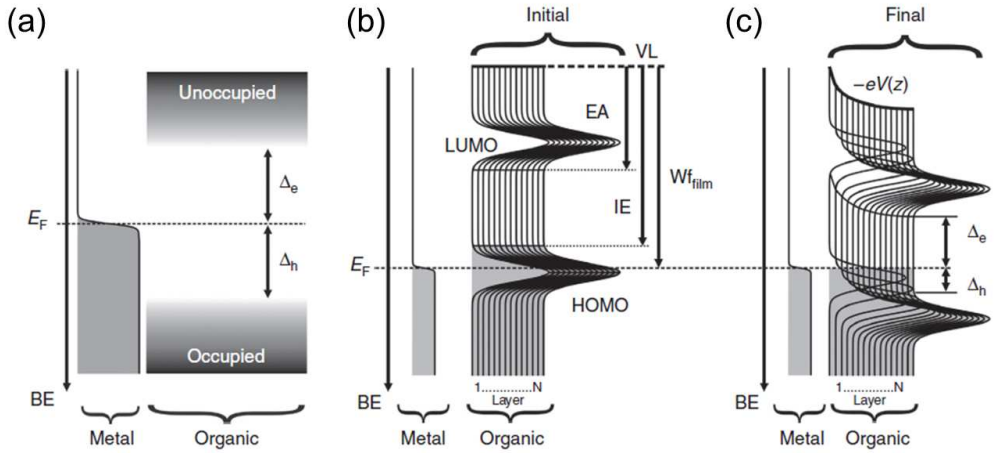

Figure 2.9: (a) Schematic representation of the electron occupation on the inorganic and organic side of the interface. The energy barriers, Δ_h for holes and Δ_e for electrons, are given by the energy distance between E_F and the onsets of the occupied and unoccupied density of states on the OSC side. (b) Initial situation before contact. Ionization energy (IE) and electron affinity (EA) are defined as the difference in energy between the HOMO/LUMO onsets and the vacuum level (VL). (c) Situation after substrate and OSCs are brought into contact. The HOMO states are shifted towards a higher $\mathrm{E_{Bind}}$ by the local electron potential energy ($-eV(z)$) for increasing the distance z from the electrode and changing Δ_h and Δ_e with respect to the initial situation. Figure taken from [46].

The defining parameter for the ELA is the position of the substrate Fermi energy relative to the HOMO and LUMO distributions, for which three different situations can be distinguished:

- The LUMO onset is lower than the substrate Fermi energy. In this case, to establish a thermodynamic equilibrium, electrons are moving across the interface from the

substrate into the "empty" LUMO states of the organic thin film leading to a positive ID.

- The HOMO onset may be higher than the substrate Fermi energy. In this case, the situation is reversed and charges will flow from the filled HOMO states of the organic layers to the substrate to establish an equilibrium. This situation is exemplarily shown in Fig. 2.9 (c) and a negative ID is observed.

- If the substrate Fermi energy lies in between the two distributions in the gap, there is no overlap and no charges are transferred. In this case, vacuum level alignment, without any ID, is observed.

To quantify the number of transferred charges, the organic film is discretized into layers of thickness Δz, which may be simply the lattice spacing between the out-of-plane planes in a thin film. The charge density $\rho(z)$ can then be calculated in each of these layers by:

$$\begin{aligned}\rho(z) = e \cdot n \cdot \Big(&\int_{-\infty}^{+\infty} dE \cdot f_H(E) \cdot D_H[E + eV(z)] \\ &- \int_{-\infty}^{+\infty} d(E) \cdot f_L(E) \cdot D_L[E + eV(z)] \Big)\end{aligned} \tag{2.1}$$

with e the elementary charge, n the number of molecules per unit area, $f_{H/L}$ the Fermi function and $D_{H/L}$ the energy distributions of the HOMO- and LUMO-derived levels. A particular advantage of the model is that it is not limited to the choice of a Gaussian peak but any other peak shape can be used instead. Additionally, every discretization interval (layer) can be modelled with a different DOS to account for, e.g. image-charge screening (see Fig. 2.7 (b)) within the first layers.

To calculate the electrostatic potential $V(z)$ across the OSC film, the $\rho(z)$ of the first layer serves to find the next $V(z)$, which is obtained by solving the 1D-Poisson equation:

$$\Delta \left[\epsilon(z) \Delta V(z)\right] = -\frac{\rho(z)}{\epsilon_0}$$

As a result of $-eV(z)$, the DOS is shifted in energy as shown in Fig. 2.9 (c), and, the next $\rho(z)$ can be calculated by occupying all states in the OSC layer up to E_F. If the difference in charge density is below a certain threshold, the iteration process is stopped. The flow of charges and the resulting electrostatic potential, shifts HOMO, LUMO and VL by the same amount (since IE and EA stay constant) and, ultimately, the energy barriers are obtained as $\Delta_e = \mathrm{E}_F - \mathrm{EA}$ and $\Delta_h = \mathrm{IE} - \mathrm{E}_F$.

With this model at hand, different situations can be analysed in greater detail:

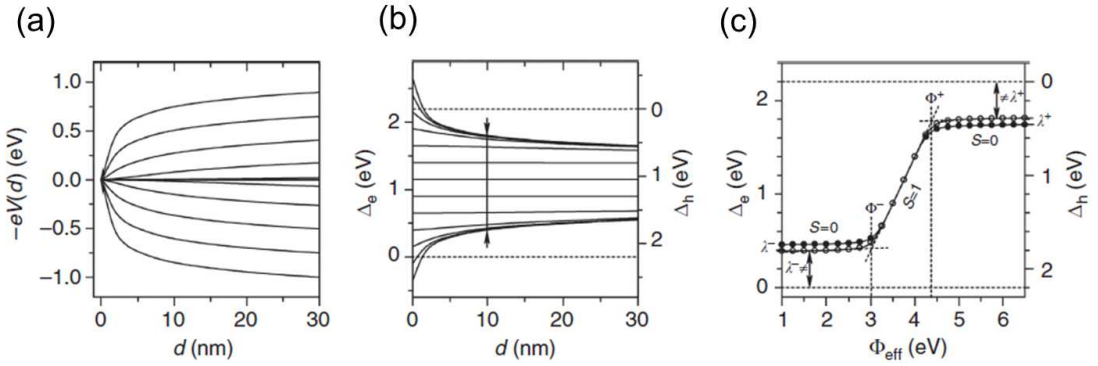

Figure 2.10: (a) shows the electron potential energy change for increasing thickness and as a function of the substrate work function. Depending on the relative position of the Fermi energy to the HOMO/LUMO Gaussians, a positive or negative potential is observed. (b) Corresponding height of energy barriers for the films presented in (a). (c) Injection barriers for electrons Δ_e and holes Δ_h for a fixed thickness but varying substrate work functions. The horizontal parts mark the Fermi level pinning regime, whereas the the region with a Slope parameter S equal to zero, describes the region of vacuum level alignment. Figure taken from [46].

Impact of substrate work function variation Figure 2.10 (a) shows the total potential energy change, $-eV(d)$, for films with increasing thickness d and for a series of different substrate work functions (Φ_{eff}). If E_F comes to lie around the middle of the OSC's gap, only very few electrons are moving from or to the substrate and, as a result, the potential energy profile stays close to flat. However, when E_F approaches either the HOMO or the LUMO DOS, distinct charge transfer and increasingly higher (and steeper) potential energy changes are obtained. Experimentally, shifting the Fermi energy is done by choosing electrodes of different work function. Fig. 2.9 (b) shows the evolution of the absolute values of the energy barriers Δ_h and Δ_e thickness-dependent and for different substrate work functions. Fig. 2.10 (c) shows the energy barriers as a function of the WF for given thickness (here d=10 nm). The resulting functional dependence can be divided by a slope of zero (S=0, characteristic for the so-called Fermi-level pinning) for low Φ_{eff}, a region with S=1 (where vacuum level alignment occurs) and again S=0 for high Φ_{eff}. The transitions between the different regions are marked by the so-called pinning work-functions.

Impact of gap states can be incorporated in the model by variation of the HOMO- and LUMO-related DOS width while keeping it Gaussian-shaped. Leaving, at the same time, the energies of the peak maxima, E_H and E_L, unchanged, one is able to mimic the effect of an increased or decreased density of additional gap states. Trivially, an increase leads to the HOMO and LUMO onsets moving further into the gap. Fig. 2.11 (a) and (b) highlight this circumstance where the width of the Gaussian is varied between $\sigma_{H/L}$=0.1 eV and 0.4 eV while keeping a constant IE and EA.

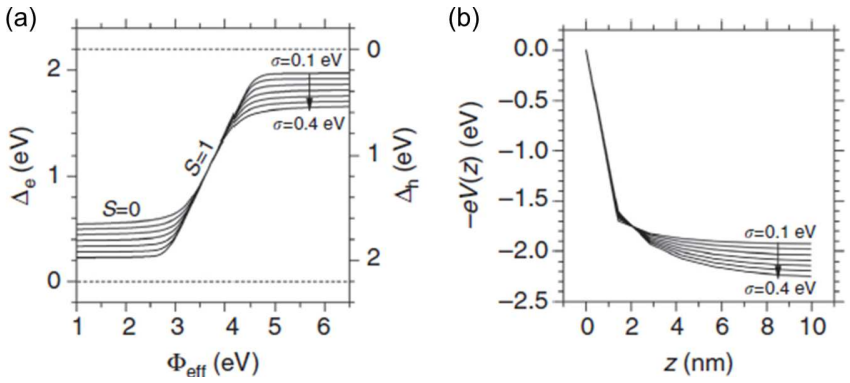

Figure 2.11: (a) Injection barriers Δ_e (left axis) and Δ_e (right axis) as a function of the substrate WF (Φ_{eff}) and with the standard deviations of the Gaussian HOMO and LUMO DOS varied between $\sigma_{H/L}$=0.1 eV and 0.4 eV while retaining a constant IE and EA. This can be applied to mimic a change in gap state density, i.e. more or less states reaching into the band gap. It can be clearly seen that the magnitude of the resulting energy barriers show a dependence on the DOS width and E_F getting pinned even farther in the gap. (b) Electron potential energy profiles thickness-dependent for a constant substrate WF. By altering the Gaussian DOS width, the potential energy changes and the observed interface dipole can be controlled. Figure taken from [46].

The electrostatic model is not only applicable for single-component systems and interfaces between an inorganic substrate and organic layers, but can also be used to model the ELA at organic-organic interfaces between different materials, which will be introduced in the following.

2.1.4.1 ELA at the organic-organic heterointerface

Going beyond the electronic properties of single component thin films to systems consisting of two differing organic layers (heterostructures), one has to acknowledge that the thermodynamic equilibrium is reached across the entire heterostructure (including the substrate). Denying the possibility of the formation of a common E_F (Fig. 2.9), would be to deny the possibility for charge carriers to be transferred through the organic heterostructure. This possibility, however, lies clearly at the very core of all organic (opto-)electronic devices [29]. Taking this consideration into account, the mechanisms introduced in the preceding section also hold for heterostructures of two different materials:

If E_F comes to lie somewhere in the gap of both the organic layers, only a negligible amount of charges will be moved. As a result, the electrostatic potential remains unchanged and VL alignment occurs (Fig. 2.12, middle column). However, if the Fermi energy lies in the fundamental gap of the first OSC but within the LUMO distribution of the second, electrons accumulate in the top organic layer (top right panel). If, on the other hand, the HOMO distribution and E_F overlap, the bottom OSC layer would stay again charge-neutral but holes are now accumulating in the HOMO levels. These examples highlight the important role of the substrate E_F. In the bottom right panel, E_F already touches the LUMO onset of the bottom OSC. Now, no electron accumulation in the top organic is observed, but charges accumulate at the interface to the substrate, pointing towards the dependence of the ELA on the stacking sequence in organic-organic heterostructures.

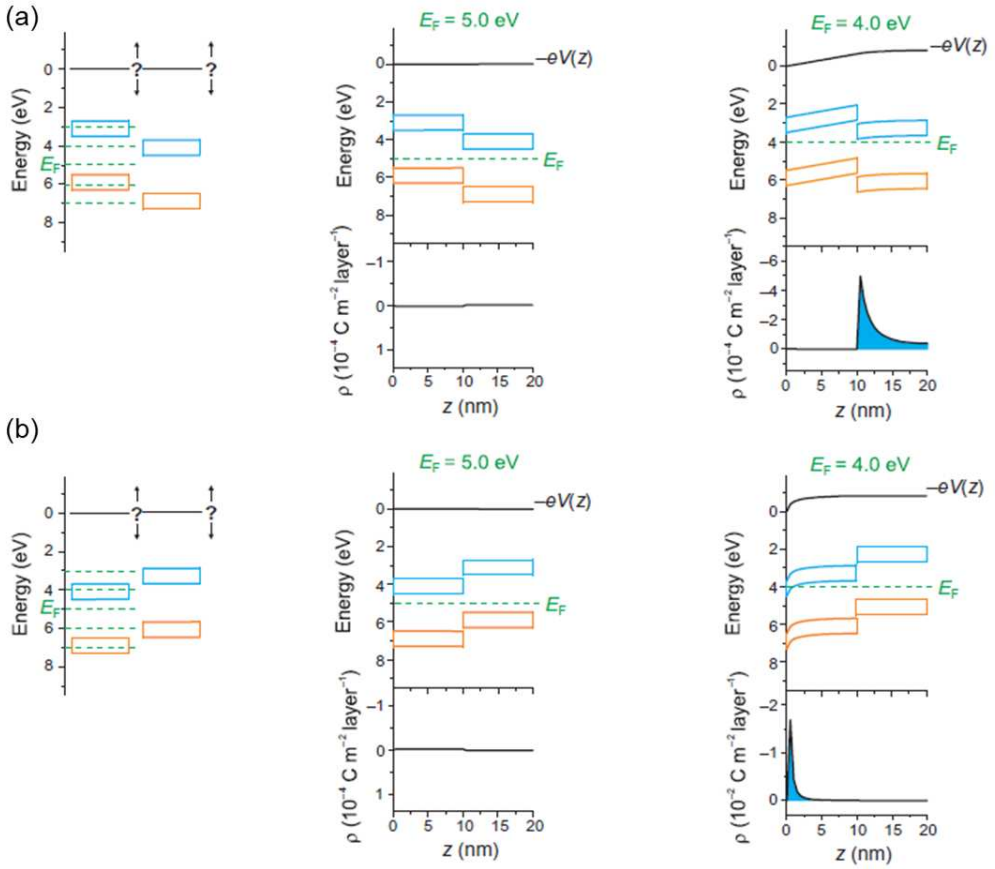

Figure 2.12: (a) Schematic representation of the situation before charge equilibration across the heterostructure and different Fermi level (E_F) positions for which results are shown in the following panels for two different Fermi energies. The top parts show the spatial evolution of the local potential energy as well as of the HOMO (orange) and LUMO (blue) distributions. The according charge-density (ρ) profiles are shown in the bottom panels. For E_F=5.0 eV (middle), the onsets of HOMO and LUMO of both materials have a significant distance to E_F, no charges are transferred and no change in potential is observed. With E_F=4.0 eV, the situation is different: Now, the top layers LUMO distribution overlaps with E_F and electrons are transferred through the bottom organic layer from the substrate into the top layer. Consistently with the single-component situation, the charge distribution shows a thickness-dependence. (b) shows the reversed deposition sequence where the bottom layers LUMO distribution is in sufficiently close proximity for E_F=4.0 eV and charges are transferred. They accumulate now in the bottom layer and leave the top layer undisturbed. Figure adapted from [29].

2.2 Electronic investigation: photoelectron spectroscopy

The experimental data on the electronic properties discussed in this work, are mainly derived from photoelectron spectroscopy (PES), for which the basic concepts as well as some details relevant for the topic of the ELA at inorganic-organic and organic-organic interfaces are briefly presented. For a more detailed introduction in PES, the reader is referred to various existing reviews and books [113, 114]. PES is a highly surface sensitive tool, widely used for the investigation of the chemical and electronic structure of condensed matter. Advantages include the extensive amount of information within a single technique and that it is essentially non-destructive [115].

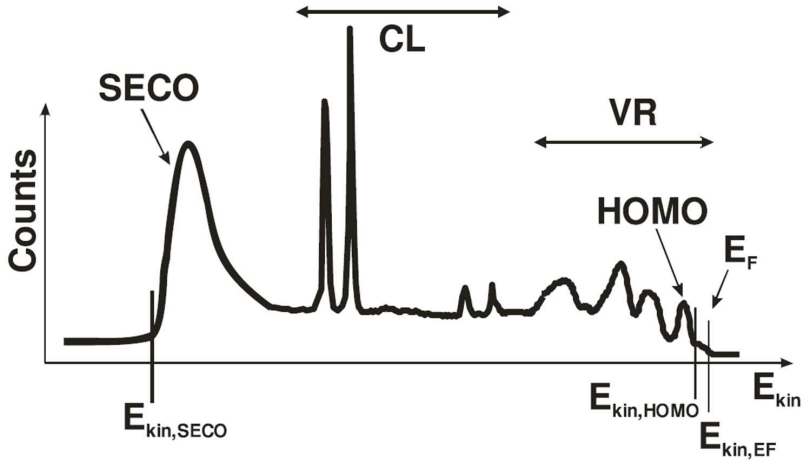

Figure 2.13: Example of the various features accessible with photoelectron spectroscopy. The energy distribution curve can be divided into the valence region (VR) and the core levels (CR). By measuring the energy distribution of electrons ejected from the sample through excitation from photons, the respective binding energies can be obtained. The secondary electron cut-off (SECO) gives information about the material's work function from, within the sample, inelastically scattered electrons. Figure adapted from [28].

In general, occupied electronic states in a sample are divided in the core level (CL) region and the valence region (VR). For OSC systems, the latter corresponds to the $\sigma-$ and $\pi-$orbitals of the contained molecules. CLs correspond to the localized atomic states that are shielded by valence electrons. In an experiment, the sample is irradiated with electromagnetic radiation of energy $h\nu$ which leads to photoelectrons being emitted due to the *photoelectric effect* [116]. Commonly, X-rays are used to emit electrons from the strongly bound CLs (X-ray photoelectron spectroscopy (XPS)) and ultraviolet radiation (ultraviolet photoelectron spectroscopy (UPS)) is used to gain information from the VR. UPS has some advantages over XPS in experiments relevant for the discussion of gap states and ELA since the photoionization cross-section for electrons is orders of magnitude higher in the valence region for UPS and the common photon sources, i.e.

noble gas-discharge lamps, have a high energy resolution (typically $\sim 30\,\mathrm{meV}$ for He lines).

Keeping the photon energy fixed and measuring the kinetic energy distribution of the emitted electrons, a typical curve (in its full range schematically depicted in Fig. 2.13) is obtained. Recording how many electrons have a certain kinetic energy, the density of states (DOS) of the particular system is probed, i.e. the number of electrons that populate a specific energy level.

For the interpretation of photoelectron spectra, the basic equation:

$$E_{kin} = h\nu - E_{\mathrm{Bind}} - \mathrm{WF}_{\mathrm{sample}} \tag{2.2}$$

is used. The electron binding energy, E_{Bind}, for a specific energy level is defined relative to E_F. In fact, thermodynamic equilibrium aligns the Fermi level of the sample and the spectrometer. The work function of the spectrometer $\mathrm{WF}_{\mathrm{spec}}$ is generally different from $\mathrm{WF}_{\mathrm{sample}}$, and VL will show a variation along the electron trajectory. However, the *measured* kinetic energy of the electron E'_{kin} is not influenced by the variation of VL, as only the potential difference between the sample surface and the spectrometer is relevant. Consequently, the relation $E'_{kin} = h\nu - E_B - \mathrm{WF}_{\mathrm{sample}} = E_{kin} - (\mathrm{WF}_{\mathrm{spec}} - \mathrm{WF}_{\mathrm{sample}})$ applies. Using the same experimental set-up, $\mathrm{WF}_{\mathrm{spec}}$ remains constant, and E_{Bind} of electronic states of any given sample can be measured, without further consideration of $\mathrm{WF}_{\mathrm{sample}}$.

Additionaly, the VL shifts (Sec. 2.1.3) that can occur upon deposition of material on the substrate surface can be studied. In an experiment, the work function is obtained from the measured energy of the secondary electron cutoff (SECO) via:

$$\mathrm{WF} = h\nu - E_{\mathrm{cutoff}} \tag{2.3}$$

The electrons are inelastically scattered within the sample, which leaves them barely able to exit the sample in the limit of E_{kin}=0 eV.[2] The VL shift can then simply be obtained by remeasuring E_{cutoff} after the deposition has been carried out. From the measurement, the parameters relevant in the context of inorganic-organic and organic-organic interfaces can be determined: the sample's work function, the organic material's IE as well as the resulting energy barriers. Unoccupied (LUMO) levels, on the other hand, cannot be measured since, without any excitation, they are not populated by electrons. Inverse photoemission spectroscopy (IPES) may be used to obtain the DOS of the LUMO distribution. However, this approach has some limitations regarding the rather poor energy resolution and a vulnerability to sample damage [117].

[2] In order to enable the measurement of the SECO, a negative potential (typically of a few volts) is applied to the sample. This shifts all energy levels upwards relative to the spectrometer and the entire energy distribution can be accessed.

2.3 Growth and structure formation of organic thin films

The following sections introduce and summarise considerations regarding the growth of organic thin films. Detailed knowledge about the mechanisms and processes involved are crucial to understand how organic thin films form and especially how structural parameters can be effectively controlled.

2.3.1 Intermolecular interactions

The arrangement of molecules within a molecular crystal or thin film depends mainly on interactions summarised as van der Waals-forces [118, 119]. They are generally subdivided into three parts, with the London dispersion force acting between electrically neutral, nonpolar molecules, Keesom-interaction between two dipoles and the Debye force between a dipole and a polarisable molecule. The focus here lies on London forces, for which the origin lies in fluctuating electrical multipole moments existing even in molecules with an average multipole moment of zero. Depending on the position of the electron cloud in the molecules, instantaneous electric fields are created acting on the electron distribution in neighbouring molecules which adjust the spatial distribution of their own electrons accordingly [120]. The averaged fluctuations between the first molecule and the induced electrical moments of the neighbouring molecules become correlated giving rise to attractive forces [121].

In general, for a pair of molecules, the induced interaction energy can be written as:

$$V_{\mathrm{London}}(r) = -\frac{A}{r^6} \tag{2.4}$$

With A, the Hamaker constant, including compound specific properties [122]. A simple approximation of molecular interactions may be obtained by summarizing the interactions of individual atoms.

2.3.2 Equilibrium considerations

Despite the fact that growth itself is by definition a kinetic process, the most suited starting point for its description is the classical wetting theory, a theory based on equilibrium consideration [123]. In this simplified picture, film growth can be considered as simple deposition of a uniform material on a substrate not taking into account its granular nature. The behaviour of the material can then be related to the surface or interface tension γ, i.e. the characteristic free energy per unit area needed to create an additional surface or interface. From equilibrium considerations one can conclude the surface tension γ_s, as:

$$\gamma_s = \gamma_F + \gamma_{S/F} \cos(\phi), \tag{2.5}$$

where γ_s is the surface tension of the interface between substrate and vacuum interface, γ_F that of the film and vacuum and $\gamma_{S/F}$ that of the substrate/film interface. Using this simple equation one can find two limiting growth modes that can be distinguished by the wetting angle ϕ. The resulting wetting or spreading behaviour of the material is depicted in Fig. 2.14.

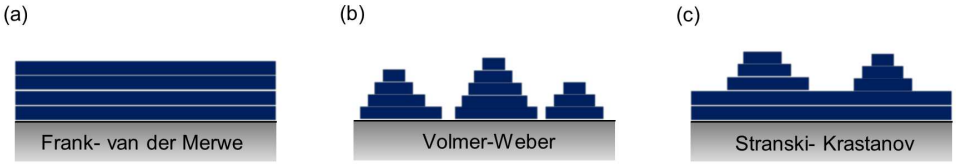

Figure 2.14: Different growth modes observed for organic thin films as a result of the surface tension situation. (a) Frank-van der Merwe or layer-by-layer growth, with a complete wetting of the substrate. (b) Vollmer-Weber growth with the formation of characteristic "wedding-cake"-structures. (c) Stranski-Krastanow growth, the most common growth mode and a combination of the two aforementioned. At first wetting layers are formed, subsequent layers then form islands on top.[124]

A wetting angle of $\phi = 0$ corresponds to Frank-Van der Merwe growth (a) with a layer-by-layer composition and complete wetting of the substrate. The Volmer-Weber growth mode (b) corresponds to a wetting angle of $\phi > 0$ and shows characteristic island formation and dewetting of the substrate. Most commonly observed, is the Stranski-Krastanow growth (c), which is a mix of the two former and may be explained by assuming a lattice mismatch between deposited film and substrate. In this case the lattice of the film tries to adjust to the substrate at the expense of elastic deformation energy. As a result complete wetting layers are formed and islands grow on top [125].

This model is suited especially for energetic considerations regarding film growth, but has one major drawback: it treats the deposited material as a continuous medium (like a liquid) and neglects effects that arise when describing the material as a collection of individual molecules. Because of that, the surface energies and wetting scenarios can only serve as a limiting case, but are not sufficient to properly describe the dynamical nature of growth.

2.3.3 Dynamical description of growth

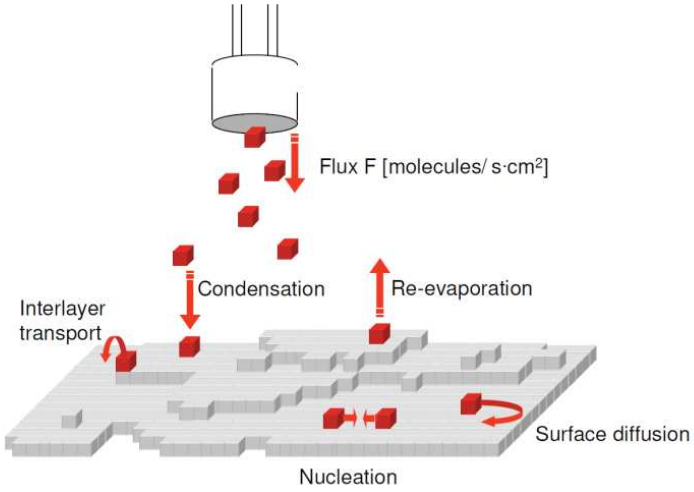

Figure 2.15: Different processes take place during the deposition of material on a substrate which necessitate a dynamical description of growth. Changing the flux of molecules from the crucible to the substrate or altering the substrate temperature one is able to control the processes and effectively change structural properties of the forming thin film. Picture taken from [126].

The multiple processes and mechanisms taking place during the growth of organic thin films (Fig. 2.15) make it a non-equilibrium phenomenon [127] and the dynamical nature of different kinetic mechanisms has to be considered [128, 129]. They include the flux of molecules from the crucible onto the substrate, the attachment or detachment of molecules to or from the surface, inter- and intra-layer diffusion as well as nucleation. In the following, the different processes are briefly introduced:

- **Flux and kinetic energy** can be controlled externally by the temperature selected for heating the molecule container. Changing the amount of molecules arriving at the surface (flux) has an impact on the diffusion length and the nucleation rate.

- **Condensation or re-evaporation** takes place when molecules impinge on the surface. If the kinetic energy of the arriving molecules is low enough, the attractive potential of the surface is sufficient for fixating the molecules on the substrate. The probability for this event to occur defines the *sticking coefficient*. Re-evaporation takes place when the attractive force of the substrate is not strong enough to hold the molecule and it leaves the surface again.

- **Surface diffusion** on the substrate surface or terrace, is a relatively easy to control process in film growth. Generally, the surface potential landscape can be described with a periodic function and an energy barrier E_D between sites is hindering molecular movement [130]. This allows to effectively control the diffusion

by choosing different substrate temperatures. For low temperatures for example, the average thermal energy k_BT of a molecule is expected to be much lower than E_D and its mobility is restricted. The temperature dependence can be studied in more detail when considering the relation between hopping rate and the height of the surface energy barrier:

$$\nu = \nu_0 \exp\left(\frac{-E_D}{k_BT}\right)$$

where a is the effective hopping distance between sites. The hopping rate is related to the surface diffusion coefficient D, which determines the migration length of a molecule on the surface within a certain time t by:

$$D = 1/4a^2\nu.$$

The factor 1/4 is a convention reflecting the two-dimensional nature of surface diffusion.

- **Nucleation** takes place as soon as a molecular cluster contains a critical number of i^* molecules [131]. Clusters containing less than i^* molecules are not stable and the probability for a decay increases. Especially in the beginning of growth, the number N of stable nuclei per unit area grows considerably fast and N is given as:

$$N \propto \Theta^{i^*+2}$$

where Θ is the total coverage of material on the substrate.

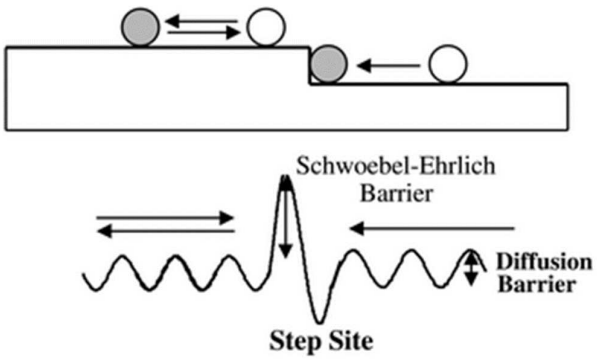

Figure 2.16: Sketch of an Ehrlich-Schwöbel barrier and the resulting energy landscape. The transport from one layer to the other is hindered due to high energy barrier at the step site. Picture taken from [132]

- **Interlayer transport:** The movement of molecules is not limited to the substrate surface or a terrace (intra-layer diffusion), but is also possible from one layer to another (inter-layer diffusion) [133]. The energy barrier, which molecules have to overcome at a step edge to change from one terrace to the other is called Ehrlich-Schwöbel-barrier (see Fig. 2.16) [134]. It results from a reduced interface and, thus, reduced attractive interactions at the step edge. For a very high Ehrlich-Schwöbel-barrier, no molecules can jump from one layer to the other and arriving molecules are reflected. The resulting coverage of island terraces then follows a perfect Poisson distribution.

3 Materials

All materials studied in this thesis belong to the class of small molecule OSCs and were selected due to the possibility to control the structural properties of the resulting thin film and, on the other hand, they cover a wide range of electronic properties in terms of IE and EA. By combination of different materials in a heterostructure, one can study the interplay between structure and electronic characteristics for various discriminative cases. The following section contains a short presentation of the compounds used for in this work with a focus on structure and electronic nature.

3.1 Pentacene (PEN)

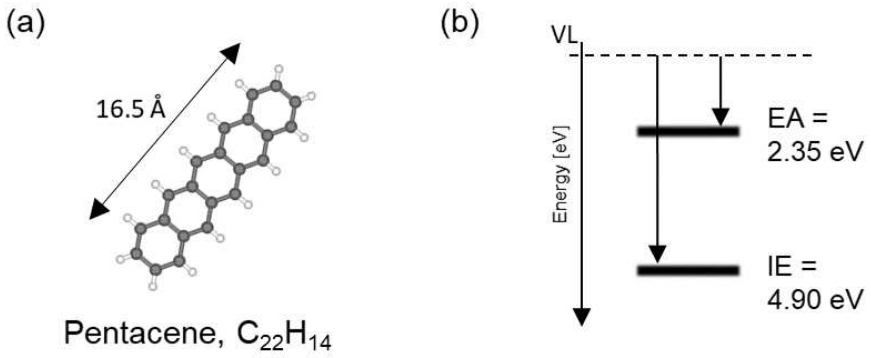

Figure 3.1: (a) Molecular structure of Pentacene (PEN). (b) Ionization energy and electron affinity for pentacene thin films on a silicon substrate [135].

Table 3.1: Lattice parameters of the 'thin film' and 'bulk' phase for PEN grown on SiO_2

	a [Å]	b [Å]	c [Å]	α [°]	β [°]	γ [°]	V [Å^3]
film	5.96	7.60	15.61	81.25	86.56	89.80	697
bulk	6.49	7.41	14.75	77.25	85.72	80.92	680

Pentacene (PEN, $C_{22}H_{14}$) belongs to the group of acenes, consisting of five benzene rings fused together linearly. It is one of the most widely studied organic semiconductors and has found its way in different applications of organic electronics [136].

When grown on native silicon, PEN exhibits a herringbone structure with a triclinic unit cell and two molecules per unit cell. Two different polymorphs for PEN are known: the thin film phase and the bulk phase. Depending on film thickness and growth conditions the one or the other can be predominant. They can be distinguished due to their differing out-of-place lattice spacing (15.4 Å for the thin film compared to 14.4 Å for the bulk phase). However, for the thicknesses deployed in this work (up to 20 nm) mainly the thin film phase is expected. On SiO_2 PEN exhibits a Stranski-Krastanow growth mode with a wetting layer and individual islands forming on top. The reported IE and EA for PEN are in gas phase 6.59 and 1.39 eV and 4.90 and 2.35 eV [135] for thin films on silicon.

3.2 Perfluoropentacene (PFP)

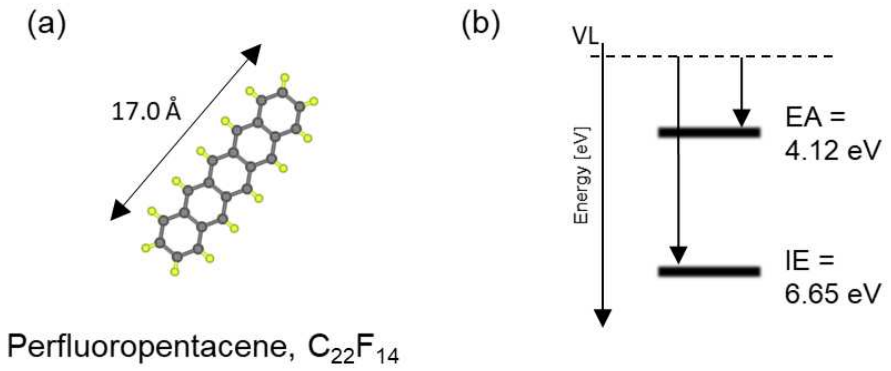

Figure 3.2: (a) Molecular structure of Pentacene (PFP). (b) Reported IE and EA of PFP growing in a standing-up configuration, as observed for the growth on silicon [135].

Perfluoropentacene (PFP, $C_{22}F_{14}$) is the perfluorinated counterpart of PEN, in which the hydrogen atoms are substituted by flourine atoms. By perfluorination, a organic hydrocarbon can be turned from a p-type semiconductor into a n-type semiconductor [137]. Also, the chemical stability often increases. PFP was extensively studied as a promising n-type material, with a high electron mobility of 0.22 cm^2/Vs, resulting from the crystalline growth on, e.g. silicon substrates [138]. The structural compatibility with PEN creates the possibility to prepare high performance bipolar transistors.
Structurally, when grown at room temperature, PFP exhibits a herringbone structure with a monoclinic unit cell and two molecules per unit cell. In thin films deposited on SiO_2 the structure of a slightly distorted 'thin film' structure was determined. IE and EA are 7.50 and 2.66 eV in gas phase and 6.65 and 4.12 eV in thin films grown on silicon [135].

Table 3.2: Lattice parameters of the 'thin film phase' and the 'bulk phase' for PFP grown on SiO_2.

	a [Å]	b [Å]	c [Å]	α [°]	β [°]	γ [°]	V [Å^3]
film	15.76	4.51	11.48	90	90.4	90	816
bulk	15.51	4.49	11.45	90	91.6	90	797

3.3 Buckminsterfullerene (C60)

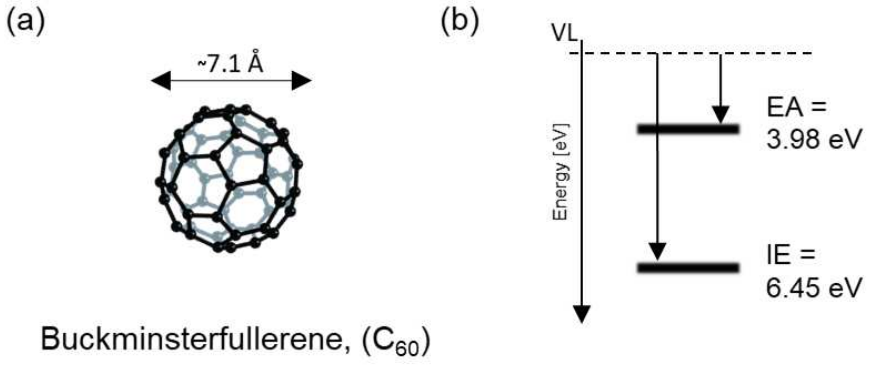

Figure 3.3: (a) Molecular structure of C_{60}. It consists of carbon atoms for which each atom has three bonds. (b) Reported IE and EA for C_{60}

Buckminsterfullerene C_{60} (C_{60}, Fig. 3.3) consists of carbon atoms which are connected by single and double bonds to form a closed structure. It is made up of fused rings of twelve pentagons and twenty hexagons [139]. The hollow spheres have been the subject of extensive research with respect to their chemistry as well as their application in nanotechnology, organic electronics and materials science [140]. In its solid form, the C_{60} molecules adopt the form of a close packed crystal with either *fcc*- or *hcp*-stacking. Due to the only weak van-der-Waals interactions between them, C_{60} molecules start rotating freely around their crystal sites at temperatures exceeding -20 °C. As a result the lattice constant shows a small, yet abrupt increase [141].

Table 3.3: Lattice parameters for different C_{60} structures measured at room temperature.

	a [Å]	b [Å]	c [Å]	α [°]	β [°]	γ [°]	V [Å^3]
fcc	14.42	14.42	14.42	90	90	90	2837
hcp	10.01	10.01	16.34	120	90	90	1417

IE and EA are 7.58 and 2.67 eV [142] in gas phase and 6.45 and 3.98 eV [52, 143] in thin films grown on silicon.

3.4 [5]- and [6]Phenacene

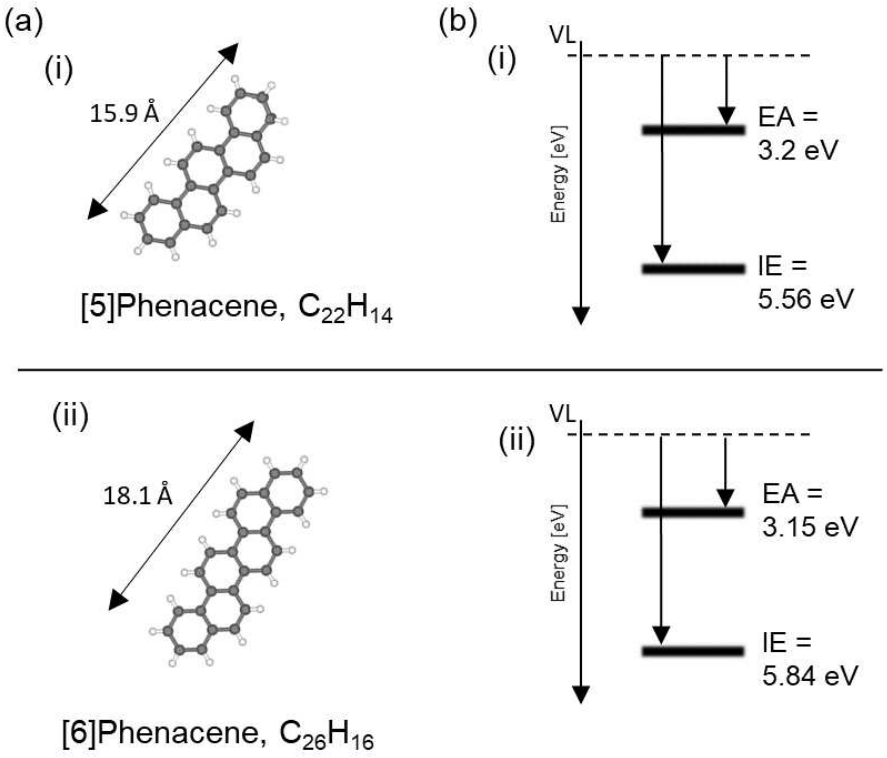

Figure 3.4: (a) Molecular structure of (i) [5]Phenacene and (ii) [6]Phenacene. (b) shows the EA and IE of the two compounds.

The two molecules depicted in Figure 3.4 belong to the class of phenacenes. They are related to acenes (e.g. PEN), but differ in the arrangement of the fused rings. Compared to the linear arrangement of PEN, the benzene rings are fused together in a zig-zag-shape. As a result, an increased stability against degradation upon exposure to light and air compared to PEN can be observed [144]. Phenacenes are a promising material for future applications of stable and high performance electronic devices such as OFETs [145].

	a [Å]	b [Å]	c [Å]	β [°]	V [Å^3]
[5]Phenacene[a]	8.47	6.15	13.52	90.5	704.3
[6]Phenacene[b]	8.4	6.2	32.0	98	1666.6

The reported IE and EA for [5]- and [6]Phenacene are in gas phase 5.5 eV and 2.2 eV, respectively 2.4 eV [146] and 5.56/5.84 and 3.2/3.15 eV [96, 147] for [5]/[6]Phenacene thin films on silicon.

3.5 α-Sexithiophene (6T)

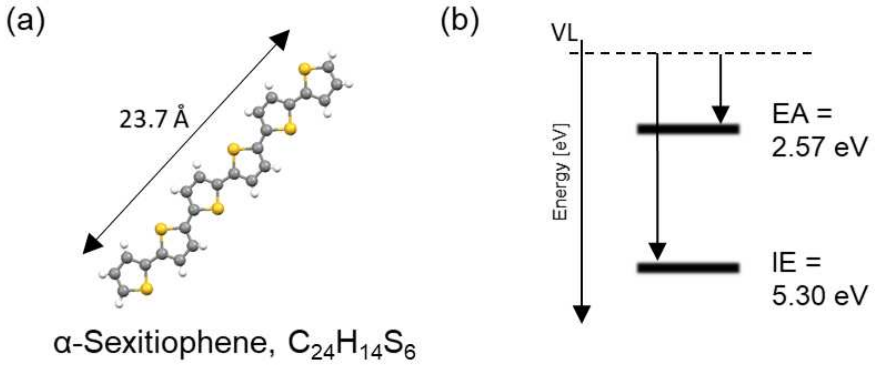

Figure 3.5: (a) Molecular structure of 6T and (b) the reported EA and IE [148].

Two single crystal structures were identified for α-sexithiophene (6T, Fig. 3.5): the so-called low-temperature (low-T) polymorph and the high-temperature (high-T) polymorph. The use of 6T in OFET architectures and the characterization of device transfer characteristics have been reported and show high charge carrier mobility of this OSC [149, 150].
The possibility to use 6T-based OFETs for chemical sensing has also been demonstrated as well as its use as donor in combination with C_{60} in organic solar cells or as templating layer for diindenoperylene (DIP) [151]. Furthermore, the recent world-record efficiency for small-molecular OSC-based organic solar cells of 13.2 % established by Heliatek has been achieved using a functionalized five-membered thiophene ring derivative in the functional organic layers [152]. The reported EA and IE are 2.57 and 5.30 eV [148] for thin films grown on SiO_2.

Table 3.4: Lattice parameters of the low-T phase for 6T grown on SiO_2

	a [Å]	b [Å]	c [Å]	α [°]	β [°]	γ [°]	V [Å^3]
low-T	44.71	7.85	6.03	90	90.76	90	2116

3.6 Substrate

For most of the thin films prepared in the course of this work, amorphous silicon (Si) with a native oxide layer (SiO_2) was used as a substrate. The choice relies on several factors: SiO_2 is commonly used as gate dielectric in OFETs and it is often passivated with an organic compound in order to reduce the density of surface traps [153]. It is established that the vast majority of OSCs interact more weakly with this kind of surface than with metal surfaces or single-crystalline surfaces of other oxides. In the context of quasi-epitaxy, for OSCs employed in this thesis, growth and self-assembly processes are not expected to be 'templated' by the amorphous substrate surfaces during growth. Another factor concerns the suitability of Si substrates for the thin film characterization methods employed in this work, for instance X-ray scattering or photoelectron spectroscopy. The native oxide layer forms naturally due to exposure of a clean Si surface to standard atmosphere with consequent diffusion of O_2 into the surface. The thickness of this native oxide layer is $\sim 2\,\mathrm{nm}$ and its exact composition varies with the distance from the Si surface, from stoichiometric SiO_2 in the topmost layers to a stoichiometry with lower O_2 content near the Si substrate. The surface roughness is in the order of few Å. In the course of this work, p-doped Si(001) wafers with a native oxide layer were used as substrate material, from which smaller slides were cut.

4 Experimental methods and techniques

In the following, the experimental methods and techniques used throughout this thesis will be introduced and explained. In the beginning, a closer look at the general sample preparation is taken. Next, the experimental details of the main techniques: organic molecular beam deposition (OMBD), X-ray scattering, atomic force microscopy (AFM) and ultra-violet photoelectron spectroscopy (UPS) are described in more detail. Note that the intention is not to give an elaborate description of each technique, but rather an overview of the basic working principles and, where needed, the reader is referred to continuative literature.

4.1 Sample preparation

4.1.1 Procedure for substrate cleaning and preparation

Since already a small amount of residues on the substrate surface can influence the structural defect density in the organic thin films, particular attention was given to the preparation and cleaning of the substrates. All substrates were cleaned in an ultrasonic bath successively using deionized water, acetone and isopropanol for five to ten minutes each. After drying under a nitrogen flow the substrates were heated outside the vacuum system to roughly 120 °C for up to 30 minutes on a heating plate to remove any excess residues. After that, the substrates were fixed on the sample holder using silver paste (home vacuum systems) or screws (UPS system) and then heated to above 350 °C and kept there, generally, over night.

4.1.2 Organic molecular beam deposition

The samples studied in this work were prepared using organic molecular beam deposition (OMBD) [154, 155]. The method is based on the use of Knudsen-cells consisting of thermally insulated glass or ceramic crucibles that are heated resistively using a tantalum wire wrapped around the crucible [156]. By heating, the molecules sublimate and enter the main vacuum chamber (see Fig. 4.1), in which they absorb onto the substrate and form an organic thin film. Thermocouples, which are placed adjacent to the crucibles,

are used to measure the temperature and a shutter, placed in front of the aperture, is used to precisely control the beginning and end of the film growth. The crucibles are held in position by a stainless-steel structure and, in order to avoid short cuts, ceramic pieces are used to insulate conducting parts. The cells can easily be mounted to any vacuum chamber and - if used in an overhead configuration - the compounds are held in place by inserting glass wool into the crucible.

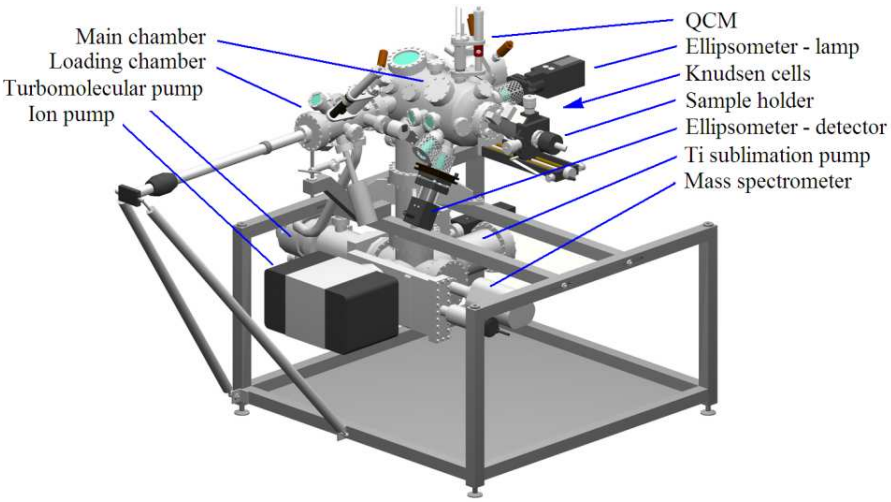

Figure 4.1: Schematic representation of the used OMBD chamber. The main chamber is connected to a loading chamber to avoid breaking the vacuum when inserting a new sample. The vacuum conditions are secured through a combination of different pumps: turbomolecular pump, ion pump and Ti sublimation pump. The chamber is equipped with a quartz-crystal microbalance (QCM) to monitor and control the deposition rate. The molecules are stored as a powder in crucibles in Knudsen cells attached to the main chamber. By resistive heating the molecules start to evaporate, enter the main chamber and are absorbed on the substrate. The substrate itself can be cooled using liquid nitrogen or heated resistively via the sample holder. Figure taken from [157].

To control the rate of deposition and the nominal thickness of the thin films a quartz-crystal microbalance (QCM) was used in the vacuum chambers [158]. Positioning the QCM in close proximity to the molecular beam allows molecules to land on the QCM sensor surface and change the oscillation frequency of the sensor from which growth parameters such as rate and film thickness can be calculated. For the UPS system used in Japan, due to technical restrictions, a permanent display of QCM values was not possible. In this case, the deposition rate was checked directly before the beginning of the growth and again right after - if the values were consistent, a constant growth rate during deposition was assumed.

4.1.3 Ultra-high vacuum

Working under ultra-high vacuum conditions is of fundamental importance for sensitive studies carried out on a surface [159, 160]. For practical reasons, such as keeping contamination on the substrate surface at a minimum or for experimental reasons, e.g. vacuum conditions with a pressure $p < 10^{-9}$ mbar are required to achieve a reasonable sensitivity in photoelectron spectroscopy measurements.
To achieve ultra-high vacuum conditions, generally, a combination of different vacuum pumps, as exemplified in Fig. 4.1 for the in-house system, is used [161]. The basic pumping unit is the pre-vacuum pump (either an oil- or membrame pump), for which an initial vacuum down to 10^{-3} mbar is achieved. Operating the pre-vacuum pump in series with a turbomolecular pump (TMP) allows to reach vacuum conditions in the high vacuum range. The TMP working mechanism is based on the transfer of kinetic energy from a series of rotating turbines to the unwanted gas molecules. The curvature of the rotors causes the affected molecules to diffuse away from the chamber downstream to the pre-vacuum pump.
In addition, the system is combined with an ion pump, where the undesired gasses get ionized and trapped in a solid electrode with a strong electrical potential (typically 3-7 kV). Under ideal conditions, this set-up is capable of reaching pressure as low as 10^{-13} mbar. In general, a lower pressure can be reached by a longer pumping time. However, the lowest accessible pressure is ultimately defined by construction parameters of the set-up and by the characteristics of the material employed. In order to further reduce the density and impact of contaminants, “outgassing” of potentially contaminated surfaces was carried out. Typically, this is done not only for the substrate (as described above) but also for the chamber walls, the crucible containing the compound and the compound itself, after a sufficiently low pressure in the vacuum set-up is reached.

4.2 X-ray scattering and organic thin films

While there are more "direct" methods to study the structure of organic thin films (e.g. scanning tunnel microscopy or transmission electron microscopy), there are also some intrinsic advantages in favour of X-ray scattering. For example, it offers the possibility to study buried layers (fundamental for planar heterostructures) and has a large information length scale, giving rise to averaged structural parameters obtained from a large area of the film. In the following, the theory of X-ray scattering is introduced and described. The focus lies on different experimental geometries and their respective use for defect density investigations. For details on the derivations, see Refs. [162–164].

4.2.1 X-ray diffraction

X-ray diffraction is based on the occurrence and direction-dependence of constructive interference. Given that the investigated sample has crystalline domains, X-rays that are hitting the sample are scattered by the electrons in specific directions (see Sec. 2.1). For the derivation, a reciprocal lattice is defined via:

$$\mathbf{b_1} = 2\pi \frac{\mathbf{a_2} \times \mathbf{a_3}}{\mathbf{a_1} \cdot \mathbf{a_2} \times \mathbf{a_3}}, \qquad \mathbf{b_2} = 2\pi \frac{\mathbf{a_3} \times \mathbf{a_1}}{\mathbf{a_1} \cdot \mathbf{a_2} \times \mathbf{a_3}}, \qquad \mathbf{b_3} = 2\pi \frac{\mathbf{a_1} \times \mathbf{a_2}}{\mathbf{a_1} \cdot \mathbf{a_2} \times \mathbf{a_3}}, \tag{4.1}$$

$\mathbf{a}_1$, $\mathbf{a}_2$ and $\mathbf{a}_3$ correspond to the primitive real-space lattice vectors. Using integer numbers h,l and k, any position in the lattice can be specified by the sum of the reciprocal lattice vectors:

$$\mathbf{b}_{\mathrm{hkl}} = h \cdot \mathbf{b}_1 + k \cdot \mathbf{b}_2 + l \cdot \mathbf{b}_3 \tag{4.2}$$

Through Eq. 4.1, each reciprocal lattice vector $\mathbf{b}_{\mathrm{hkl}}$ corresponds to a set of real-space lattice planes that is orthogonal and describes their orientation. In addition, the length of $\mathbf{b}_{\mathrm{hkl}}$ is connected to the inter-plane distance d by

$$|\mathbf{b}_{\mathrm{hkl}}| = \frac{2\pi}{d} \tag{4.3}$$

The condition for constructive interference is given by Bragg's equation and occurs at an angle Θ:

$$2d \sin\Theta = n \cdot \lambda \tag{4.4}$$

with n being an integer number and λ corresponding to the X-ray wavelength. Bragg's law is equivalent to the so-called Laue condition, which connects the scattering vector $\mathbf{q}$ of the X-ray beam and the reciprocal lattice vectors by:

$$\mathbf{q} = \mathbf{k}_{\mathrm{out}} - \mathbf{k}_{\mathrm{out}} = \mathbf{b}_{\mathrm{hkl}} \tag{4.5}$$

with the incoming and exiting wave vectors $\mathbf{k}$ having an absolute value of $2\pi/\lambda$. In polycrystalline samples with a random distribution of crystal directions, a crystallite can be found in any direction for which the Laue condition is fulfilled. For uniaxially anistropic polycrystalline samples, crystallites exhibit a fixed orientation with respect to a preferred direction (e.g. the out-of-plane direction) but are unoriented around this axis. In this case, the diffraction pattern shows no dependence on the direction of the component of $\mathbf{q}$ perpendicular to this direction and depends solely on the two components q_z and q_{xy} of the scattering vector $\mathbf{q}$. To achieve access to all combinations of q_z and q_{xy}, two different diffraction geometries, namely, X-ray reflectivity and grazing incidence X-ray diffraction have been applied.

4.2.2 X-ray reflectivity

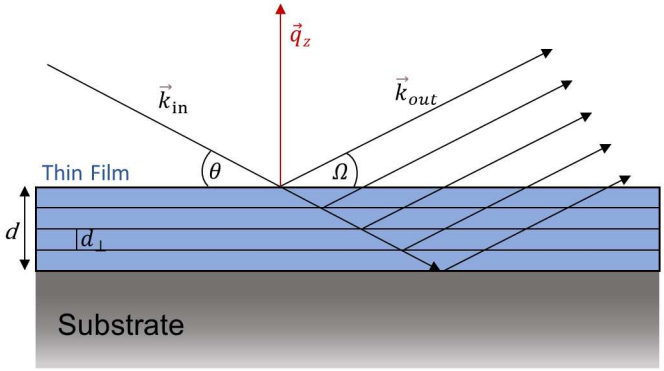

Figure 4.2: Schematic of the scattering geometry for x-ray reflectivity (XRR). The angle between incoming and outgoing beam is kept constant, so that the momentum transfer q_z is perpendicular to the substrate. From a XRR scan, different film parameters are obtained, e.g. information about the out-of-plane lattice spacing $d_\perp$ or the film thickness d.

X-ray reflectivity (XRR) allows the investigation of the electron density profile of a sample in the direction perpendicular to the substrate (along the surface normal) as well as the morphology of the sample. A specular geometry (Fig. 4.2) is used to probe the out-of-plane momentum transfer q_z by keeping the angle of the incoming beam, Θ, and the angle Ω (detector angle) equal. In this geometry, the only relevant component of the momentum transfer q is perpendicular to the substrate and can be written as:

$$q_z = \frac{4\pi}{\lambda} \sin\Theta$$

From a typical XRR dataset (Fig. 4.3), the following features can be obtained and converted into physical properties of the thin film:

- **Total reflection edge** depends on the average electron density ρ_e of a sample. For organic systems, the electron density is often in a similar range (see section 4.2.1)

- **Bragg peaks** are a result of the coherent superposition of waves scattered from families of molecular layers stacked in the out-of-plane direction for the case when the Bragg condition is fulfilled. The position of Bragg peaks allows to calculate the lattice spacing $\mathrm{d}_\perp$.

- **Kiessig fringes** (or oscillations) arise from interference between the reflected wave at the film/air and the film/substrate interface. The occurrence of such fringes does not depend on the thin film having a crystalline texture and can be observed also for

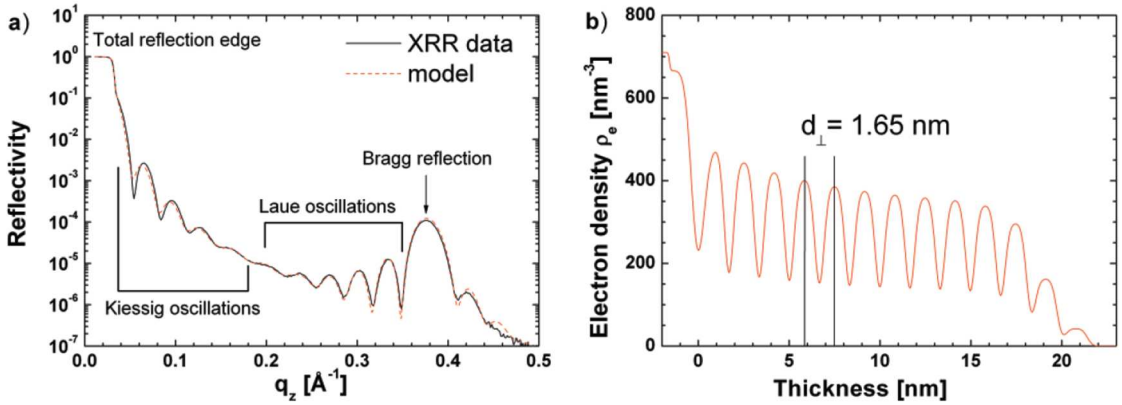

Figure 4.3: Example of a typical XRR scan (a) and the probed electron density profile (b) obtained from a model fitted to the data. From the position of the total reflection edge, the spacing and damping of Kiessig oscillations, the existence of Laue oscillations and the position of Bragg reflections, different thin film parameters can be obtained.

amorphous film. The spacing Δq_z between the Kiessig fringes allows an approximate calculation of the film thickness via the equation $d = 2\pi/\Delta q_z$. Additionally, the damping provides a qualitative estimation of the thin film roughness.

- **Laue fringes** (or oscillations) are interference fringes originating from crystals scattering coherently along the z-direction. Their spacing provides information on the length scale of coherence in the out-of-plane direction. For organic semiconducting molecules exhibiting high structural order, the thin film often scatters coherently for its entire thickness d, and Kiessig and Laue fringes provide the same information.

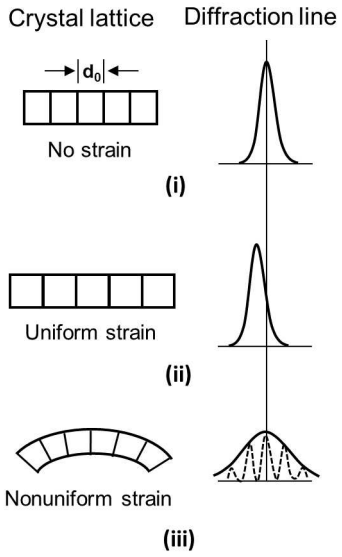

Figure 4.4: Effect of uniform and nonuniform strain on the diffraction line. Uniform strain (ii) leads to the lattice being tugged or compressed and the observed Bragg reflection shifted towards higher or lower values compared to the diffraction line observed without any strain (i). If the strain is nonuniform the the reflection is broadened due to a superposition of reflections.

Williamson-Hall analysis Additionally, information about structural defects can be obtained via the so-called *Williamson-Hall analysis*[1] [165]. Due to dislocation formation and other kinds of defects, an organic solid usually contains regions where the lattice is bent or twisted. This leads to planes in a particular grain being strained and their lattice spacing deviating from an ideal $d_\perp$. If this deviation is uniformly distributed, the corresponding diffraction peak is simply shifting to higher or lower angles (Fig. 4.4 (ii)). However, if the deviation is non-uniform (e.g. tension on the top and compression on the bottom) the grain can be imagined to be composed of regions with an essentially constant lattice plane spacing but slightly different from the spacing of adjacent regions, each of which contribute a sharp diffraction peak indicated on the right side by the dotted curves in Fig. 4.4 (iii). Since only an ensemble of crystalline domains is measured in a XRR experiment, a broadened peak is observed. Experimentally, a direct analysis of defects from the peak broadening is hindered by the fact that not only defects but also grain size is influencing the peak width. To separate the two effects, the full width at half maximum (FWHM) of reflections in a given crystal direction is plotted as a function of $\sin\Theta$ from which the reciprocal of the intercept with the y-axis gives an estimate of grain size and the slope can be assumed as a measure of defect density. This method

[1] In fact, the theory developed by Williamson and Hall deals with (micro-)strain in a given system. However, since strain and dislocations are two sides of the same coin (where dislocations can be seen as the source of strain and vice versa) they are used here synonymously.

is known as the *Williamson-Hall plot* and is, naturally, also applicable in the crystal in-plane direction.

4.2.3 Rocking scans

By definition, in a rocking scan the sample is moved around a tilt angle ω. Practically, this is done by keeping the sample fixed, while scanning the X-ray source and detector concurrently toward the same direction, such that the incident angle is varied but 2Θ (and consequently the absolute momentum transfer $|q_z|$ remains unchanged) [166]. The plot of the scattered X-ray intensity as a function of ω is called a *rocking curve*. Rocking scans can be conducted in the in-plane and out-of-plane direction, in this work solely rocking curves in the out-of-plane direction were recorded. Two defect parameters can be obtained from a rocking curve:

- **Mosaicity**, i.e. the average tilt of crystallites relative to the surface normal is probed by rotating the sample around the ω-axis and selecting different tilt angles for which equation 4.2.2 is fulfilled [106]. Analysing the width of the resulting reflection, the FWHM can be used as a degree of mosaicity of the thin film. The smaller FWHM, the better the individual crystallites are aligned.

- **Out-of-plane defect density** can be extracted from an analysis of the diffuse scattering signal surrounding the sharp (Bragg-)component of a rocking curve as introduced by Nickel et al. [167]. There, a misorientation vector τ is defined and the diffuse intensity around each reciprocal lattice-point assumed to be a function of it. A linear increase of the FWHM of the diffuse scattering intensity κ_{II}^{D} is characteristic of defects and strain fields found in organic films. From a linear plot of κ_{II}^{D} versus the ascending higher order reflections, a defect density in the out-of-plane direction can be estimated.

4.2.4 Grazing incidence X-ray diffraction

To study lateral structures, grazing incidence X-ray diffraction (GIXD) was performed. In GIXD, the angle of incidence, Θ, is chosen to be close to the total reflection edge. This leads to a evanescent field and only a small penetration depth of the X-ray beam into the sample (see section 4.2.1). Θ is kept equal to the out-of-plane detector angle Ω. The structure is then investigated by variation of the in-plane angle 2Φ (Fig. 4.5).
Most of the samples studied in this work are polycrystalline and correspond to an in-plane powder without a preferred orientation. Therefore, probing the in-plane structure by

GIXD can be understood in terms of powder diffraction. The momentum transfer can then be calculated from:

$$q_{xy} = \frac{2\pi}{\lambda}\sqrt{(\sin\Phi\cos\Theta)^2 + (\cos\Omega\cos\Phi - \cos\Theta)^2} \tag{4.6}$$

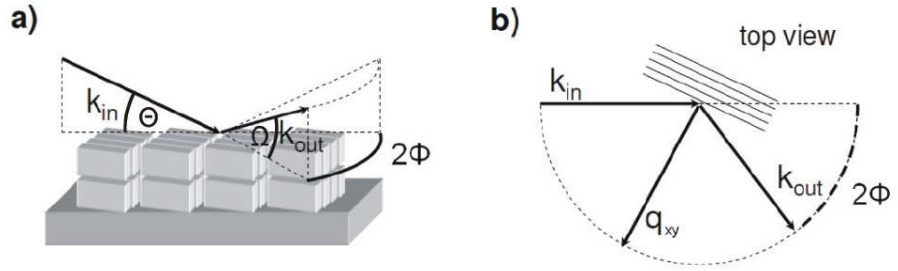

Figure 4.5: (a) Schematic representation of the GIXD geometry. The angle of incidence of the incoming beam is kept constant, while the detector angle is changed parallel to the substrate (2Φ). Diffraction takes place at the crystalline in-plane lattice and information about the in-plane arrangement of molecules can be obtained. Picture taken and modified from Ref. [168].

Scherrer's formula To probe the size of the in-plane coherently scattering domains D_{coh} the width (in terms of the full width at half maximum) of Bragg reflections obtained from a GIXD scan is analysed. Since D_{coh} is a function of structural parameters altering the crystalline order (e.g. grain boundaries, dislocations, point defects), an in-plane areal defect density can be obtained.
The theory behind peak broadening due to D_{coh} size was developed by Scherrer [163, 169]. As a starting point, a crystal with thickness D consisting of m planes is assumed, corresponding to an undisturbed region in the thin film. The angle Θ is regarded as a variable and Θ_B defined as the angle which exactly satisfies Bragg's law. By considering incident rays that lead to Bragg angles only slightly different from Θ_B and careful analysis of the constructive and destructive interference situation in such a system, two limiting angles Θ_1 and Θ_2 are found at which the diffracted intensity must drop to zero. The angular range, $2\Theta_1$-$2\Theta_2$, increases as the number of coherently scattering planes m decreases leading to a broader diffraction curve. Considering the path difference for these two angles for the entire thickness, the well-known Scherrer formula

$$D_{\text{coh}} = \frac{2\pi}{\text{FWHM}} \cdot 0.9394 \cdot K_s \tag{4.7}$$

is obtained. Here, K_s is the Scherrer constant for spherical grains. The instrumental broadening of the diffractometer was not included in the calculations, therefore only lower limits of D_{coh} are given.

4.2.5 X-ray sources and experimental setup

The X-ray measurements were either performed at the home laboratory source or at a synchrotron facility. In the home laboratory, a GE XRD 3003TT diffractometer is used (Fig. 4.6). A copper anode in combination with a multilayer mirror and a germanium mononchromator ($CuK_\alpha 1$ radiation, $\lambda = 0.151\,nm$) is applied for the generation of X-rays. Synchrotron measurements were either performed at beamline I07 of the Diamond Light Source (DLS) in Didcot (UK) [170], the SiXS beamline at the Soleil synchrotron in Gif-sur-Yvette, France [171] or at ID03/ID10 of the European Synchrotron Radiation Source (ESRF) in Grenoble, France [172, 173].

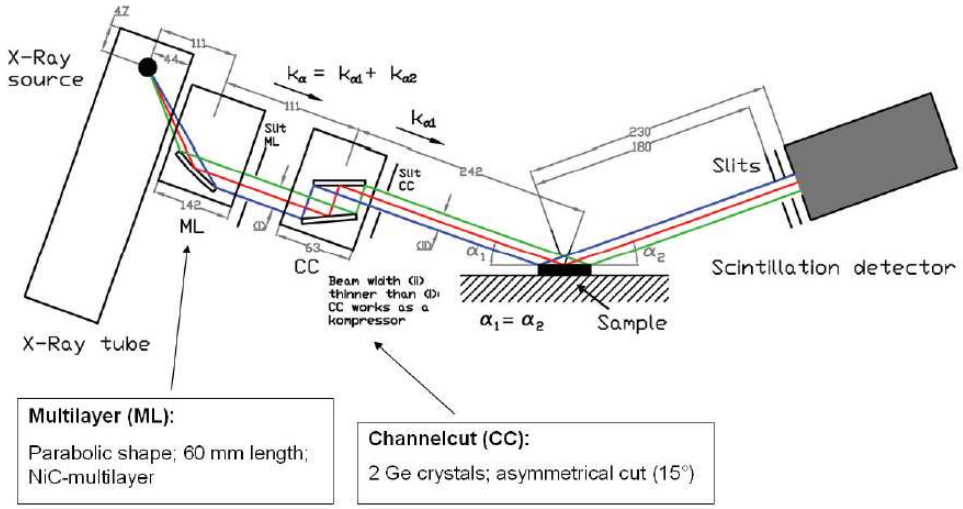

Figure 4.6: The experimental setup of the home diffractometer (XRD 3003). The X-rays are generated using a copper anode and multilayer mirrors and beam cuts are used to focus a monochromised beam onto the sample. Figure taken from [157]

4.2.6 X-ray scattering experiments in situ and in real-time

To study growth behaviour and structure formation of organic heterostructures in situ, X-ray real-time experiments were conducted at beamline I07 of the DLS. A home-build portable UHV system, as depicted in Fig. 4.7 was used [155, 174]. The chamber is equipped with a beryllium-window, a pumping system and a resistive heating or cooling (using liquid nitrogen or helium) option connected to the sample holder. The system can be mounted on a diffractometer at a synchrotron. The pumping systems consists of a roughing pump, turbo pump and ion pump with which a base pressure of 10^{-9} mbar is reached.

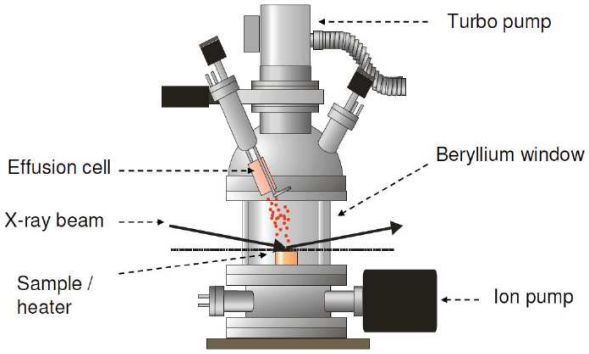

Figure 4.7: Schematic of the portable UHV chamber used for real-time and in-situ measurements. The chamber can be mounted on any standard diffractometer. It is equipped with the possibility for resistive sample heating and cooling using liquid nitrogen or helium. The X-ray beam can enter and exit through the Beryllium window which is vacuum tight, allowing for the creation of UHV conditions. Picture taken from Ref.[168]

4.3 Atomic force microscopy

Besides the possibility for the manipulation of matter on the nano-scale, atomic force microscope (AFM) can be used for the characterization and imaging of surfaces in the atomic range. The working principle is based on the interaction between a microscopically fine tip with the sample surface. The resulting adhesion forces range in the order of only 10^{-9} to 10^{-10} N. To measure such small changes in the interaction forces, highly sensitive devices have been developed, which combine a variety of laser-optical techniques.

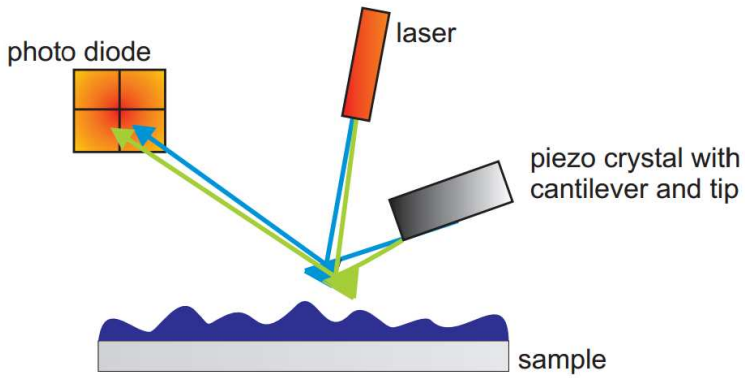

Figure 4.8: Schematic representation of the working principle of an AFM setup. A laser beam is directed onto the reflective cantilever surface and any movement from the tip measured with a four-quadrant photodiode.

The principle of an AFM measurement is illustrated in Fig. 4.8. The cantilever moves

over the sample surface in a systematic fashion [175]. For the positioning as well as for the initial approach of the tip to the surface piezoelectric components are used. The height information is collected via a laser beam, directed onto the back side of the cantilever, from where it is reflected into a four-quadrant photo-detector diode.

The AFM can be operated in two different modes: contact and intermittent mode [176]. In contact mode, the tip and sample remain in close contact as the scan proceeds. When imaging soft materials, such as OSCs, intermittent mode is often the better choice, since the tip is not in contact with the surface but oscillating close to it. In a scan, the frequency and amplitude of oscillation is modified by the tip-sample interaction forces. By moving the cantilever either upwards or downwards, a constant force between the sample surface and the tip is maintained, as a result the surface morphology is obtained. In contrast to the averaging nature of the above described X-ray scattering techniques with information length scales extending to several hundreds of microns in the regime of grazing angles, AFM yields direct local information over scales of one up to some tens of microns. Thus, AFM is complementary to the above-mentioned reciprocal x-ray techniques.
The AFM images in this thesis were recorded using a Nanowizard-II AFM system from (JPK/Bruker) [177].

Data visualisation and analysis: For visualisation and analysis of the obtained AFM images, the freely available software Gwyddion was used [178]. Major benefits of the program are the many built-in data processing and statistical quantities tools e.g. background correction and data levelling.

4.4 Ultraviolet photoelectron spectroscopy

4.4.1 Experimental setup at the Institute for Molecular Science, Okazaki, Japan

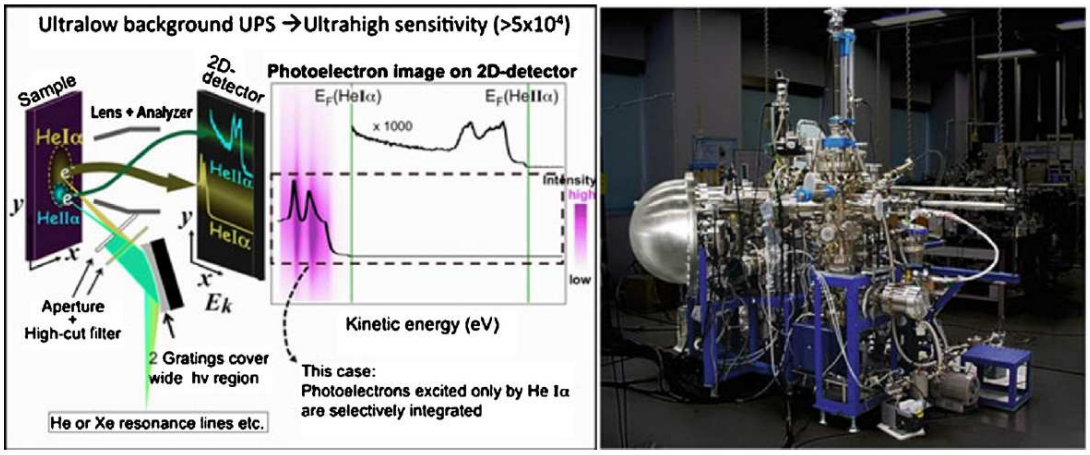

Figure 4.9: Schematic description of the high sensitivity measurement method (left) and a photograph of the UPS setup (right). Image from [179].

Most of the UPS measurements presented in this work were performed using an ultralow-background, high-sensitivity UPS apparatus with a hemispherical electron analyser (MBS A-1) and either a monochromatic HeI (energy: 21.2 eV) or XeI (8.4 eV) radiation source. The gap state density spectra were typically acquired over 90 min. All UPS spectra were measured at normal emission with an acceptance angle of ±18°. The He or Xe light was incident at 45° with respect to the sample surface. A bias of -5 V was applied to the sample in order to detect the secondary cutoff.

The UPS chamber is equipped with the possibility to transfer the sample from the growth chamber into the measurement chamber without breaking the vacuum. Additionally, the sample holder can be heated resistively or cooled down using liquid nitrogen. To achieve the ultra-low background necessary for the direct measurement of gap states a dedicated experimental setup was developed at Chiba University in Japan and is today located at the Institute for Molecular Science in Okazaki, Japan. Fig. 4.9 displays the principle of the high sensitivity measurements as well as a photograph of the apparatus. Two monochromators for the incident beams and, to further reduce the intensity of high/low-energy impurity photons, two filters (Al thin film and LiF single crystal) are installed and are used depending on the desired photon energy. The basis of the ultrahigh sensitivity techniques is the use of a hemispherical electron energy analyzer with a two-dimensional detector (see Fig. 4.9, left). By selecting a particular area of the detector the information from photoelectrons solely excited by the desired photons can

be separated and the secondary electron background produced by inelastic scattering of high kinetic energy photoelectrons produced by the remaining high energy photons can be significantly lowered. A more detailed introduction can be found in [179].

4.4.2 Experimental setup at Soochow University, China

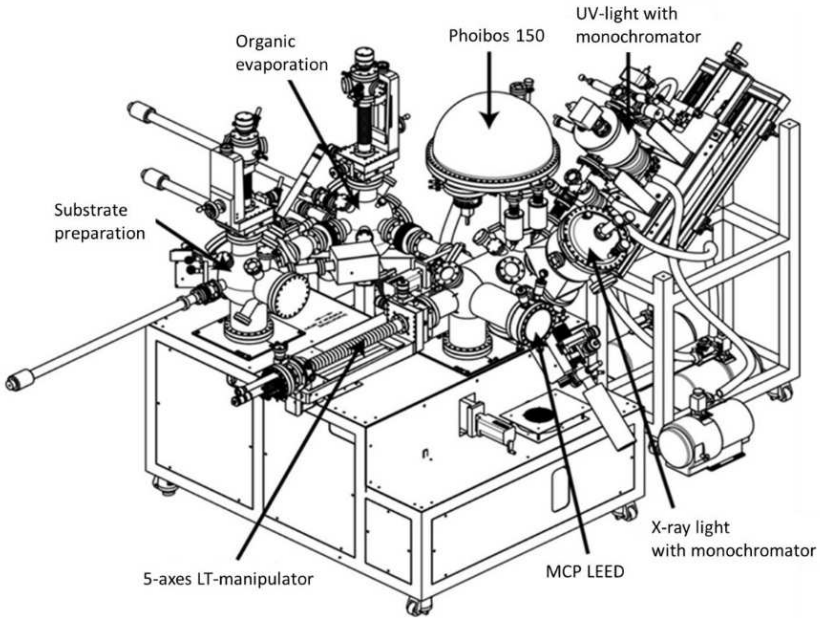

Figure 4.10: Schematic representation of the UPS chamber used in parts of this work. The setup is located at the Institute of Functional Nano and Soft Materials (FUNSOM) at Soochow University, China and belongs to the group of Prof. Steffen Duhm. The picture is courtesy of SPECS GmbH.

Parts of the UPS measurements presented in Sec. 5.2 of this work were carried out in Prof. Steffen Duhm's group, at the Institute of Functional Nano and Soft Materials (FUNSOM) at Soochow University, China. The used setup is depicted in Fig. 4.10. Three interconnected chambers with different functions are deployed: a evaporation chamber (base pressure in the order of $3{\cdot}10^{-10}$ mbar), an annealing and sputtering chamber (base pressure: $3{\cdot}10^{-10}$ mbar) and an analysis chamber (base pressure: $2{\cdot}10^{-10}$ mbar). The measurements were performed using monochromatized HeI radiation ($h\nu = 21.2$ eV) and a Specs PHOIBOS 150 analyzer. The angle between the incident beam and the sample was fixed to 40°.

5 Results and Discussion

In this chapter the obtained results are presented and discussed. With the general investigation strategy depicted in Fig. 5.1, the order of results follows a certain logic: first, possible sources of gap states - in terms of structural defects - are studied in greater detail. The goal is to isolate the kind of defect, ultimately responsible for the creation of gap states. In the second and third part, the structural and electronic properties of device-relevant planar organic-organic heterostructures are investigated. Of main interest are the parameters influencing the ELA.

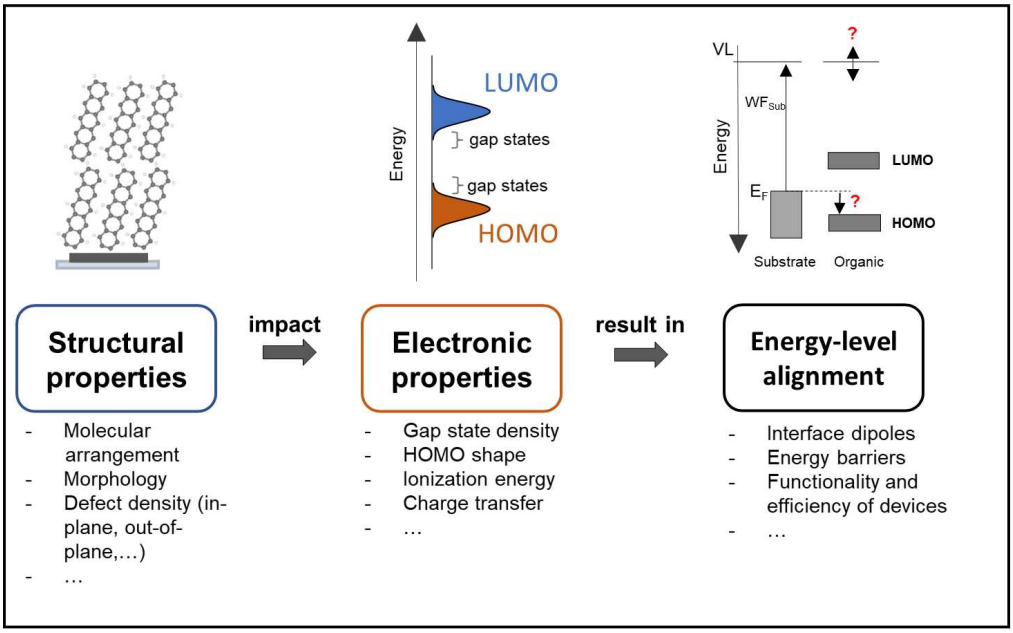

Figure 5.1: Schematic representation of the general investigation strategy of either single component thin films or donor/acceptor heterostructures (post-growth as well as in-situ). In general, the structural properties are studied regarding their crystal structure, the morphology and, of particular interest, the densities of different kinds of structural defects. In a next step, the interplay of structural properties and electronic properties are studied and, for that matter, a main focus lies on the dependence of the gap state density on structural defects. Ultimately, the energy-level alignment at the interface of OSCs with inorganic substrates or at the organic-organic interface is investigated. While the emphasis might differ in the following sections, generally, all three topics are studied, respectively.

5.1 On the origin of gap states in molecular semiconductors

A phenomenon observed at the interface between inorganic-organic and organic-organic materials is the energy-level alignment, in which the relative positions of the molecular frontier orbitals can be shifted, and energy barriers can be smaller or larger than what is theoretically expected [32, 180–182]. Different mechanisms have been proposed to explain this behaviour, but, until now, a unifying model is still elusive and depending on the reactivity of the substrate, different cases must be distinguished [37, 182–184]. For the case of weakly interacting, inert surfaces it was proposed that the ELA is in fact governed by a small density of electronic states within the energy gap of the organic compounds [45, 185–187]. They are thought to result from structural or chemical defects acting as dopants, and also, theoretical studies modelling the presence of gap states underline the importance and impact on the ELA mechanism [29, 46, 62, 110]. It was demonstrated that their appearance is a common feature in molecular thin films and their density can be controlled by changing preparation parameters [45, 53, 73, 188].

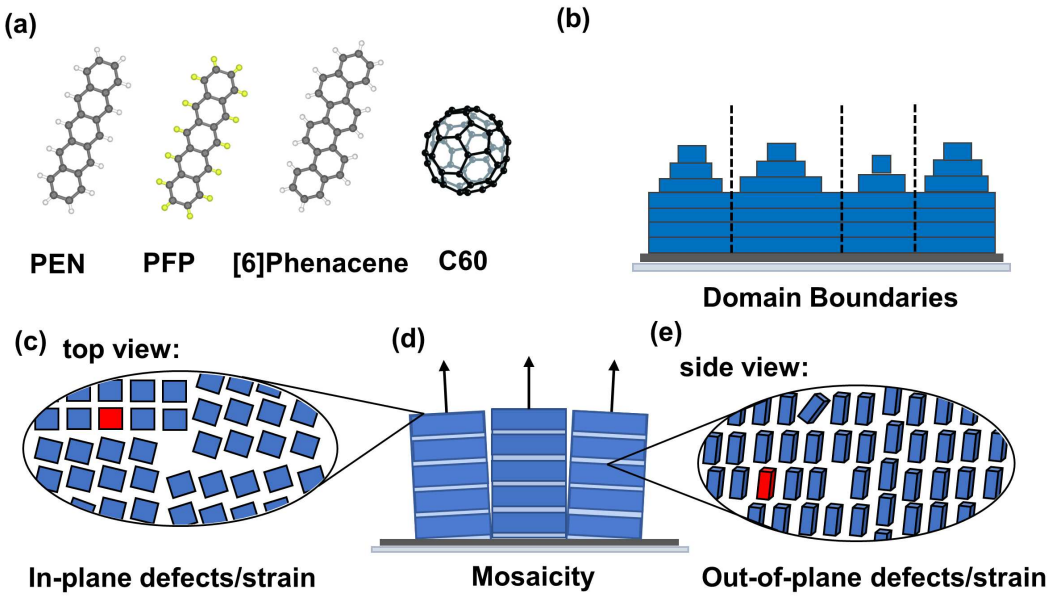

Figure 5.2: (a) The four prototypical OSCs chosen for the first part of this investigation. They differ in their composition, structure and their electronic properties. (b)-(e) Schematic representation of the different structural defects as possible sources for gap states. Each represents a different length scale or orientation. They range from rather large scale boundaries between adjacent domains (b), to microscopic defects and dislocations in-plane (c) and out-of-plane (e).

In this section, two approaches are deployed to vary the structural defect density. In the first part, based on Ref. [96] and concerned with single-component thin films of PEN, PFP, [6]Phenacene and C60 (Fig. 5.2 (a)), the substrate temperature during growth is varied within one sample set. Since the dynamical processes and mechanisms described in Sec. 2.3 are affected by the higher thermal energy of the molecules on the surface, more or less structural defects are induced. [101, 155, 174].
The second approach, introduced in the subsequent part, is the mixing of two structurally and electronically closely related compounds, namely [5]- and [6]Phenacene. They are co-evaporated in varying mixing ratios and, due to their structural compatibility, mix on the molecular level. By replacing one or the other compound statistically in the respective unit cell, point defects are introduced in the blend.

In both parts, different X-ray techniques and AFM measurements are combined to study the molecular arrangement, morphology and, subsequently, to study and organize the different defects depending on their length scale and direction [189–191]. The focus lies on rather large scale domain boundaries [192] (Fig. 5.2 (b)) and microscopic dislocations, point defects or impurities (indicated as red blocks) within the organic crystal [193, 194], which, in turn, can be divided into in-plane and out-of-plane defects (Fig.5.2 (c),(e)). The obtained results are then compared to the variation of the gap state density obtained from UPS. Doing so, conclusions regarding the main source of gap states can be drawn. Since the UPS signal of the gap states is some orders of magnitude smaller than the typical signal of valence states, a direct measurement is generally difficult and is only achievable by acquiring UPS data with an ultra-low background. Such an approach allows for data acquisition and quantitative visualization of the density of gap states even on a logarithmic scale.

5.1.1 Gap states induced by temperature variation

Gap states and their impact on the ELA were first described by Sueyoshi et al. in copper phthalocyanine thin films [91]. By exposure to inert nitrogen gas (N_2) they found a drastic and reversible change in bandwidth and -shape as well as in the energy position for repeated cycles of gas exposure and subsequent annealing. The changes were broadly ascribed to weak intermolecular interaction between the organic material and the gas molecules and their effect on the molecular packing structure by N_2 diffusion into the film.
Since then, the same principle of defect creation has been used successfully on multiple OSCs including C60 and PEN [50, 52]. However, the underlying relationship between structural properties and the gap state density was never studied systematically and is often simply assumed. In order to conduct an extensive and systematic study of the interplay between gap states and structural defects, 20 nm thin films of PEN, PFP, C60

and [6]Phenacene were grown on SiO_2 with a rate of 2 Å/min at substrate temperatures of 250, 300 and 350 K, respectively.

5.1.1.1 Structural characterization

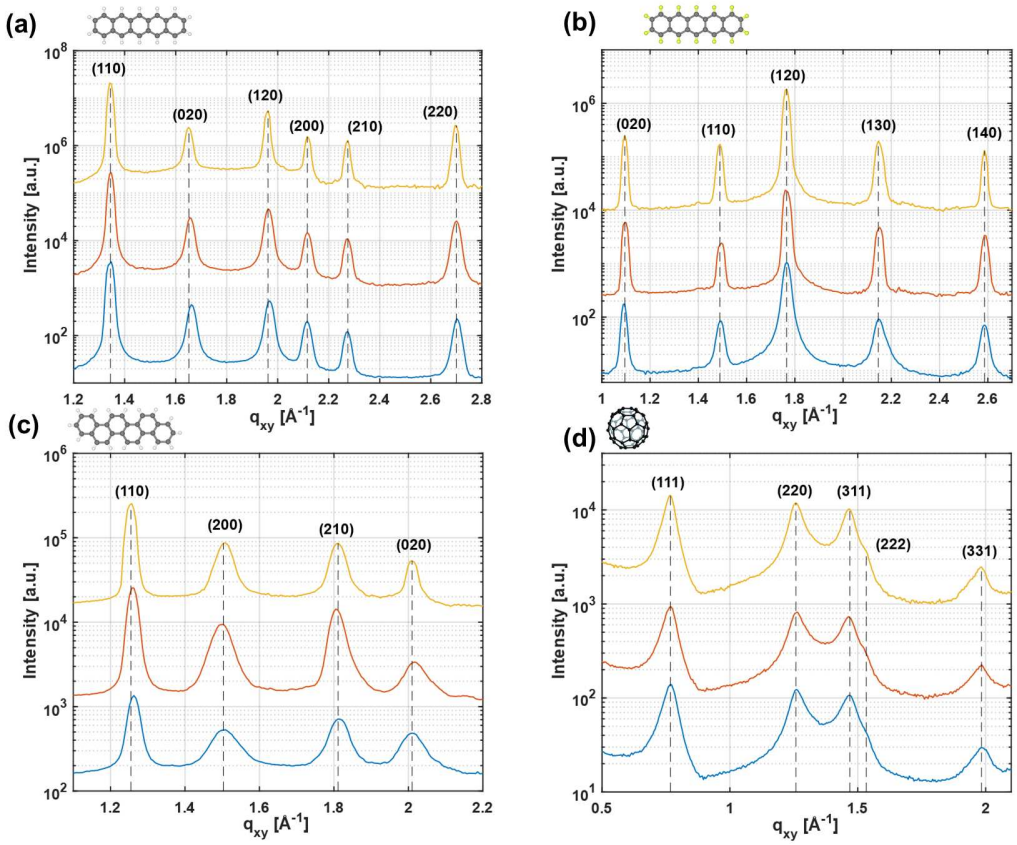

Figure 5.3: GIXD spectra of (a) PEN, (b) PFP, (c) [6]Phenacene and (d) C60 grown at different substrate temperatures. The different colors correspond to the temperatures: 250 K (blue), 300 K (brown) and 350 K (yellow). All compounds show the polycrystalline arrangement expected for growth on SiO_2 and consistent with literature. PEN, PFP and [6]Phenacene exhibit a so-called fibre texture (2D powder) with the two short unit cell axes parallel to the substrate. In contrast, C60 exhibits Bragg reflections consistent with randomly distributed domain orientations (3D powder).

In-plane structure Figure 5.3 shows GIXD spectra of PEN, PFP, [6]Phenacene and C60 grown at different substrate temperatures. The colors correspond to the temperatures: 250 K (blue), 300 K (brown) and 350 K (yellow) and are maintained in the following. Consistent with literature, the compounds show the polycrystalline arrangement expected for growth on SiO_2. PEN (a), PFP (b) and [6]Phenacene (c) exhibit a so-called fibre texture (2D powder) with the two short unit cell axes parallel to the substrate [195–197].

C60, on the other hand, exhibits the Bragg reflections consistent with the randomly distributed domain orientations of a 3D powder [198]. In general, Bragg peak positions for different growth temperatures are rather identical for each compound, indicating that the crystal structure is not affected by a change of growth temperature. Therefore, different polymorphs can be ruled out as sources of gap states.

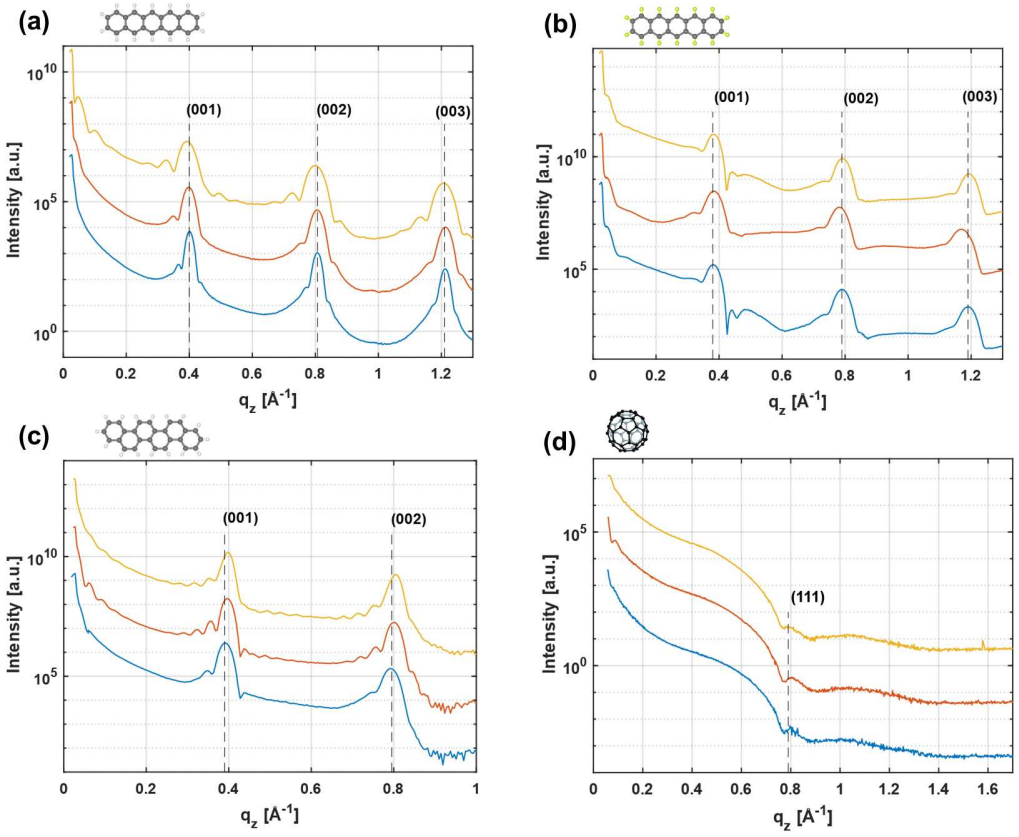

Figure 5.4: XRR spectra of the compounds grown at different substrate temperatures. The rod-like molecules (a) PEN, (b) PFP and (c) [6]Phenacene show a high order in the out-of-plane direction, evident from the observed Bragg peaks and corresponding to molecules standing upright with a small inclination to the surface normal. For C60, only a weak Bragg peak signal is found, consistent with randomly distributed domains and no strong out-of-plane ordering of molecules. Changing the temperature during growth only has a minor impact on the structure for all investigated compounds.

Out-of-plane structure The out-of-plane arrangement was studied using XRR, for which the spectra are shown in Figure 5.4. From the well defined Bragg peaks a significant order for the rod-like molecules is observed. The position of the respective Bragg peaks corresponds to molecules standing upright with a small inclination to the surface normal. As expected, C60 shows also a low ordering in the out-of-plane direction, with only a weak signal from (111) planes and consistent with the observed in-plane arrangement.

Altering the temperature during growth only has a minor impact on the structure, however, for [6]Phenacene a marginal dependence of the lattice spacing can be found, with the Bragg peak for the higher temperatures slightly shifted towards higher q_z values. The damping of Kiessig oscillations shows a general trend towards smoothers films for elevated temperatures, especially evident from the pentacene sample set (a).

Morphology The morphology of the thin films was studied using an AFM. The obtained images are collected and presented in Figure 5.6, where from left to right, the temperature was increased stepwise. A general trend for all films is the increase of domain size with elevated temperatures. This observation can be explained with an increased downhill transport of molecules. Due to a higher thermal energy, the diffusion length is increased and more molecules are able to overcome the step-edge barrier at terrace borders. As a result, the valleys between adjacent domains are filled and smoother films are obtained. Decreasing the temperature, on the other hand, has a converse effect, with smaller domains and rougher films. The behaviour is exemplarily shown in Fig. 5.5 for [6]Phenacene. Increasing the temperature leads to a smoothing, shown in (a), reaching from $\sigma_{250\mathrm{K}}$=4.6±0.3 nm to $\sigma_{300\mathrm{K}}$=3.9±0.3 nm and $\sigma_{350\mathrm{K}}$=4.6±0.3 nm in terms of the root-mean-square (rms) roughness. (b) shows the evolution of the correlation length, a measure for the mean peak-to-peak distance [199]. Moving from low to elevated temperatures, the correlation length increases roughly five-fold.

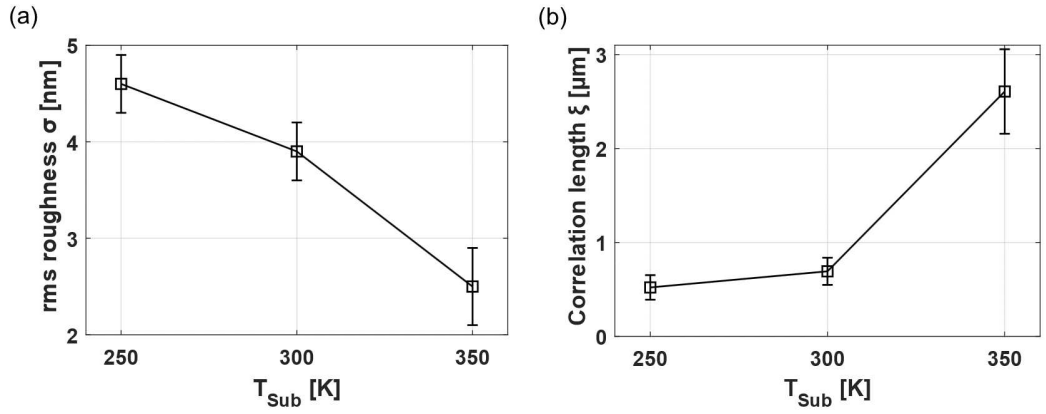

Figure 5.5: The evolution of the root-mean-square roughness σ (a) and the correlation length ξ (b). The decrease and increase respectively may be explained with an increased downhill transport of molecules.

The distinct domain shapes are well preserved for the films of PEN (a) and [6]Phenacene (c) with a complete wetting layer and more or less spherical islands growing on top. The domains for PFP show the characteristic needle-like shapes for all substrate temperatures (b), while the C60 domains are significantly smaller and only observable as a collection of spherical structures without any distinct features.

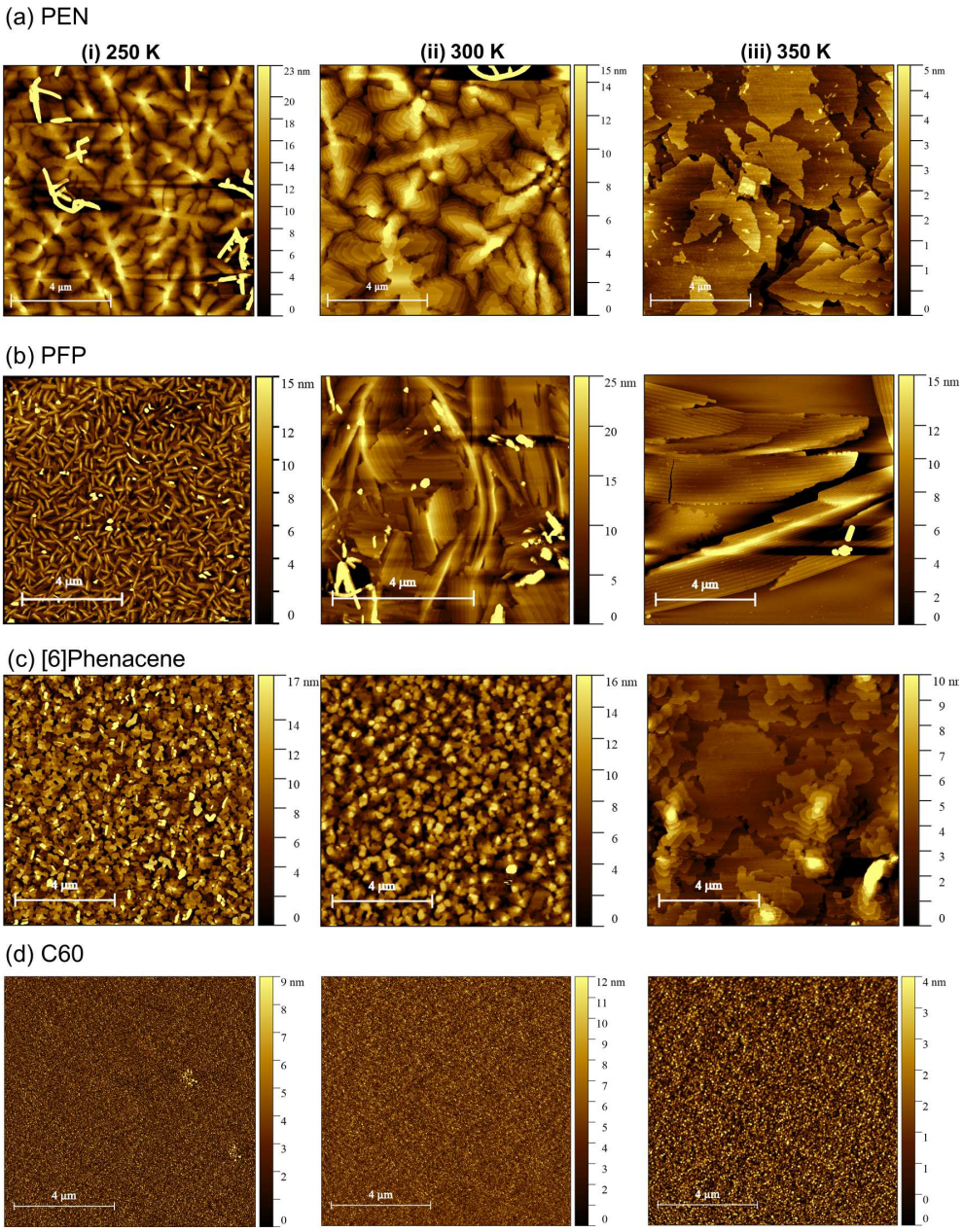

Figure 5.6: AFM images of the different compounds arranged in rows, for which the temperature was increased moving from left to right ((i)-(iii)). For all samples a complete wetting of the substrate is found, with individual domains growing on top. As a general trend, an increase of domain size for elevated temperatures is observed. While for PEN, PFP and [6]Phenacene individual features and terraces can be resolved, the domains for C60 are too small and are only observable as a collection of spherical structures.

5.1.1.2 Structural defects

Now, the different kinds of structural defects are introduced and investigated in detail. For better comparison within one sample set and between the different compounds, the defect density is generally normalized to the room temperature (300 K) sample. As pointed out before, the defects are organized according to their length scale (from large domain boundaries to microscopic defects) and their direction (in-plane or out-of-plane).

Domain boundaries To determine the density of defects from large domain boundaries (Fig.5.2 (b)), the height profiles of each sample measured by AFM (Fig. 5.6) are used. For quantification of the domain size changes, the boundary lengths were extracted using the software Gwyddion [178] and its built-in grain-detection function for at least three different AFM images per sample. Figure 5.7 shows the resulting boundaries (in red) for the images presented above. Already by eye, it is obvious that an increase of temperature leads to decrease of boundary length which corresponds well with the increase of domain size. Comparing the trend by normalizing the length to the respective room temperature film one finds the decrease reaching from a factor of 0.4 for the low temperature PEN sample to 0.6 for the low temperature [6]Phenacene sample, the increase from 1.2 for high temperature [6]Phenacene to approximately a factor of 1.75 for the high temperature PFP sample compared to the respective 300K films (Fig.5.7, right column).

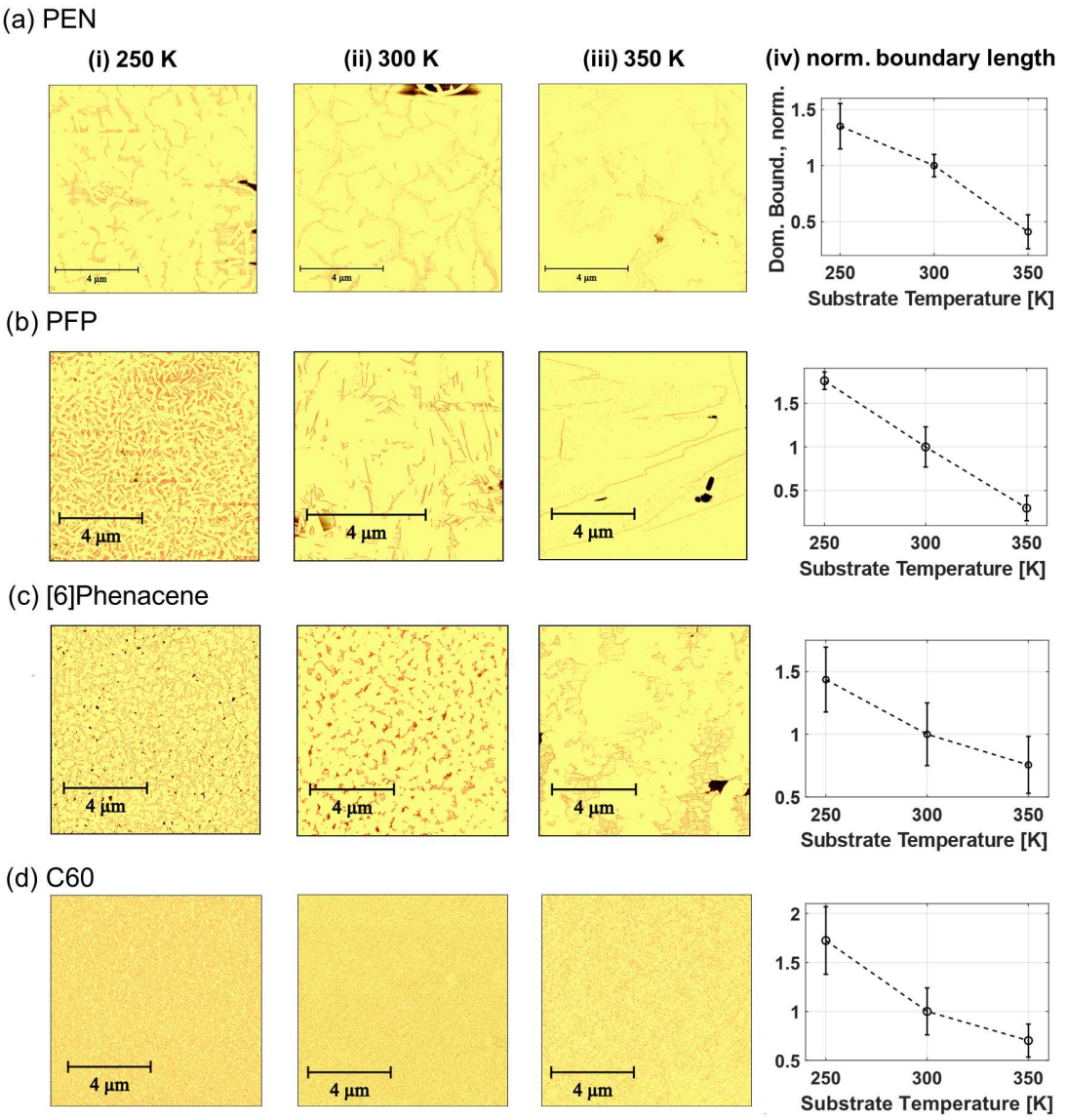

Figure 5.7: Domain boundaries indicated in red from the AFM images presented above. To determine the boundaries, the buit-in detection function of Gwyddion was used [178]. An increase of boundary length between adjacent domains for the lower temperature samples is observed. This corresponds well to the increase of domain size described before. The last column (iv) shows the trend of the domain boundaries with changing substrate temperature, normalized to the respective room temperature sample (300 K).

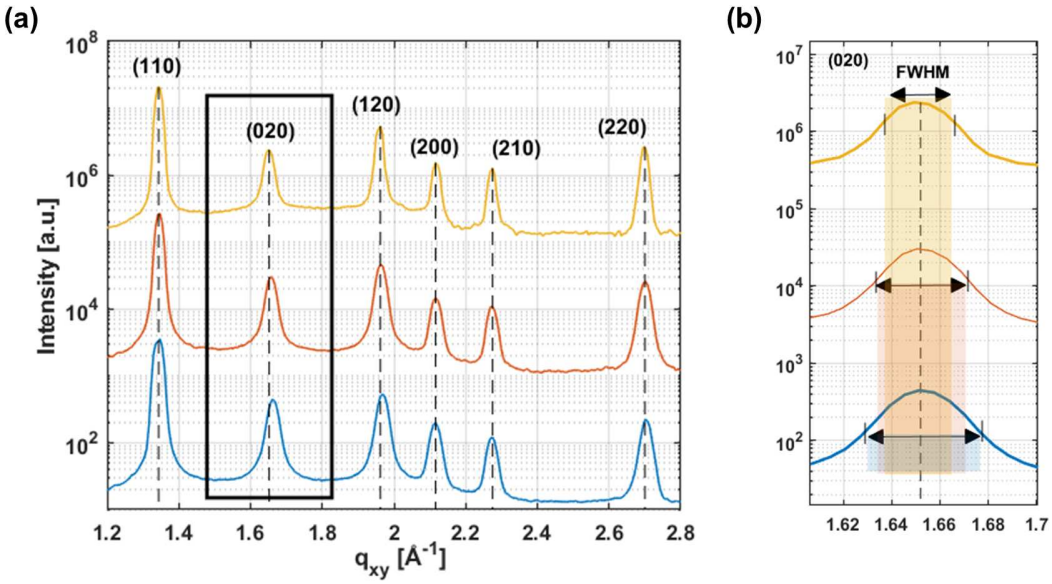

Figure 5.8: Representative example of the behaviour of the width of Bragg reflections in terms of the FWHM. (a) shows the GIXD scans for PEN, with an emphasis on the (020) reflection. (b) Zoom into the (020) Bragg reflection with indicated FWHM. As a general trend, the width of reflections is broadened for low temperatures leading to smaller coherently scattering island sizes (D_{coh}) for lower temperatures.

In-plane defects GIXD allows to study structural in-plane defects related to the crystal structure as introduced in Sec. 4.2.4 and described in Fig. 5.8. Analysing the width of Bragg reflections for all samples in Fig. 5.3, the in-plane coherently scattering island size D_{coh} can be obtained through Scherrer's formula. D_{coh} depends mainly on strain, dislocations and point defects (misfits, vacancies), which reduce the long-range crystalline order in the thin films [200, 201] and can be converted into an areal defect density via $1/D_{coh}$ [202, 203]. Depicted in Fig. 5.9 are the obtained and normalised defect densities. As a general trend, the defect density, which is inversely proportional to D_{coh}, is decreasing with increasing the substrate temperature. A decline to a factor of about 0.6 for the high temperature [6]Phenacene sample and 0.8 for the high temperature PEN sample is observed. The increase of defects lies between 1.2 for the C60 sample grown at low temperature and up to 1.6 for the PFP low temperature sample.

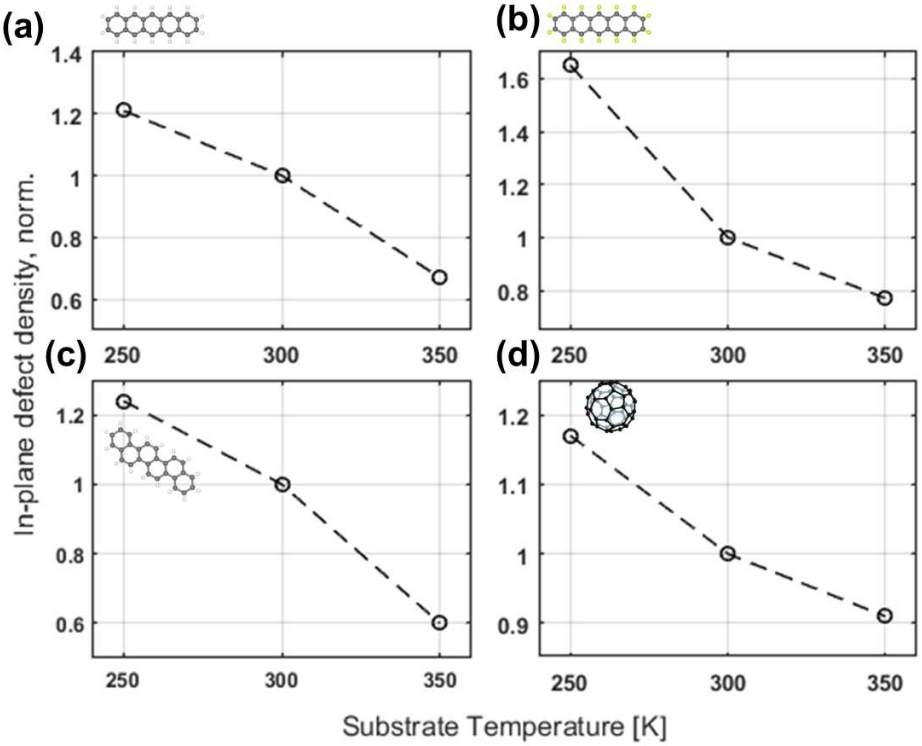

Figure 5.9: The normalized in-plane areal defect density obtained from the FHWM of Bragg reflections in GIXD scans shown in Fig. 5.3. D_{coh} can be converted into a defect density via $1/D_{coh}$ [202, 203]. Increasing the substrate temperature generally leads to a decrease of defects for all studied compounds. The figure shows the data for PEN (a), PFP (b), [6]Phenacene (c) and C60 (d).

Out-of-plane defects The defects acting in the out-of-plane direction are investigated by different approaches. First, the tilt of crystallites relative to the surface normal is studied. The small displacement between neighbouring molecular layers in adjacent crystallites can potentially lead to a change in molecular orbital overlap. Fig. 5.10 shows rocking curves for (a) PEN, (b) PFP, (c) [6]Phenacene and (d) C60. The curves are fitted with Gaussian functions and the respective FWHM is used as the magnitude for the mosaicity (i.e. the tilt in the out-of-plane direction). Especially for the PEN and PFP sample a trend of the impact of substrate temperature is visible, with the mosaicity increasing with decreasing growth temperature. However, the [6]Phenacene data does not show appreciable dependence between the low temperature and the reference sample, with only a 3% alteration. The rocking curves of the C60 thin films in Fig. 5.10 (d) are identical with the resolution limit of the X-ray setup. This is consistent with C60 growing as randomly distributed crystallites on SiO_2. The inset shows the respective trend, normalized to the room temperature sample.

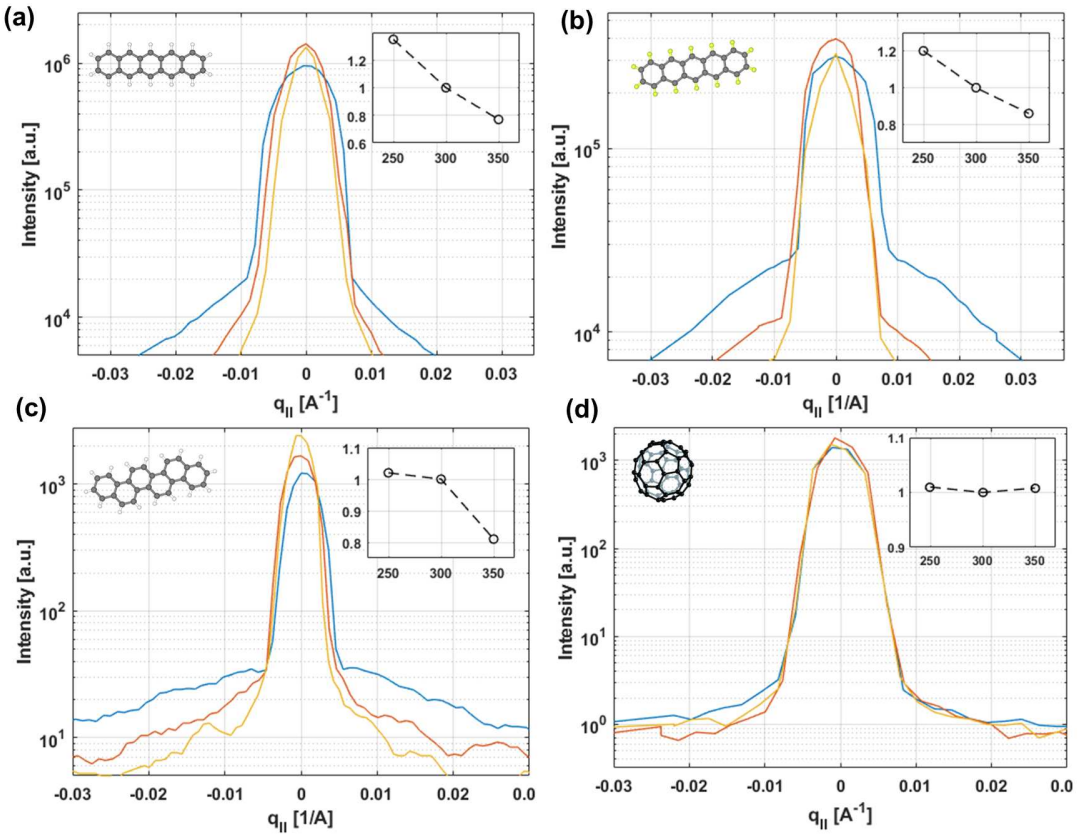

Figure 5.10: Rocking curves around the first out-of-plane reflection of (a) PEN, (b) PFP, (c) [6]Phenacene and (d) C60. By keeping the incident and exit angles constant, the scattering vector is constant and the average tilt of crystallites, i.e. mosaicity can be measures. For PEN and PFP, a trend of the impact of substrate temperature is visible, with the mosaicity increasing with decreasing growth temperature. [6]Phenacene, on the other hand, does not show a appreciable dependence between the low temperature and the reference room temperature sample. For C60, the rocking curves are identical within the resolution limit of the X-ray setup, consistent with C60 growing as randomly distributed crystallites.

A second approach is to analyse the broadening of the Bragg reflections of ascending order in the out-of-plane direction, i.e. the Williamson-Hall analysis (see section 4.2.2). With this method the density of strain, dislocations and misfits along the surface normal is investigated. To separate the effects of (i) diffraction-order independent broadening due to the average finite size of the crystallites, (ii) order-dependent broadening due to strain introduced by structural defects, and (iii) instrumental broadening, the total integral breadth $\beta_2\Theta$ (ratio of peak area to height) is plotted against reduced reciprocal units d*. The resulting slope denotes the maximum strain, which is proportional to the distortion of the crystal lattice. Figure 5.11 shows WHA plots for (a) PEN, (b) PFP and (c) [6]Phenacene. In the case of C60, a WHA is not feasible due to the lack of out-of-plane Bragg reflections (see Fig. 5.4 (d)). As can be seen in (d), a low substrate temperature during growth has a strong impact on the defect density with a greater slope

for all the compounds. However, the growth at higher substrate temperatures only has a minor impact with the strain and defect densities staying close to the reference room temperature sample for PEN and PFP and even increasing again for the [6]Phenacene sample.

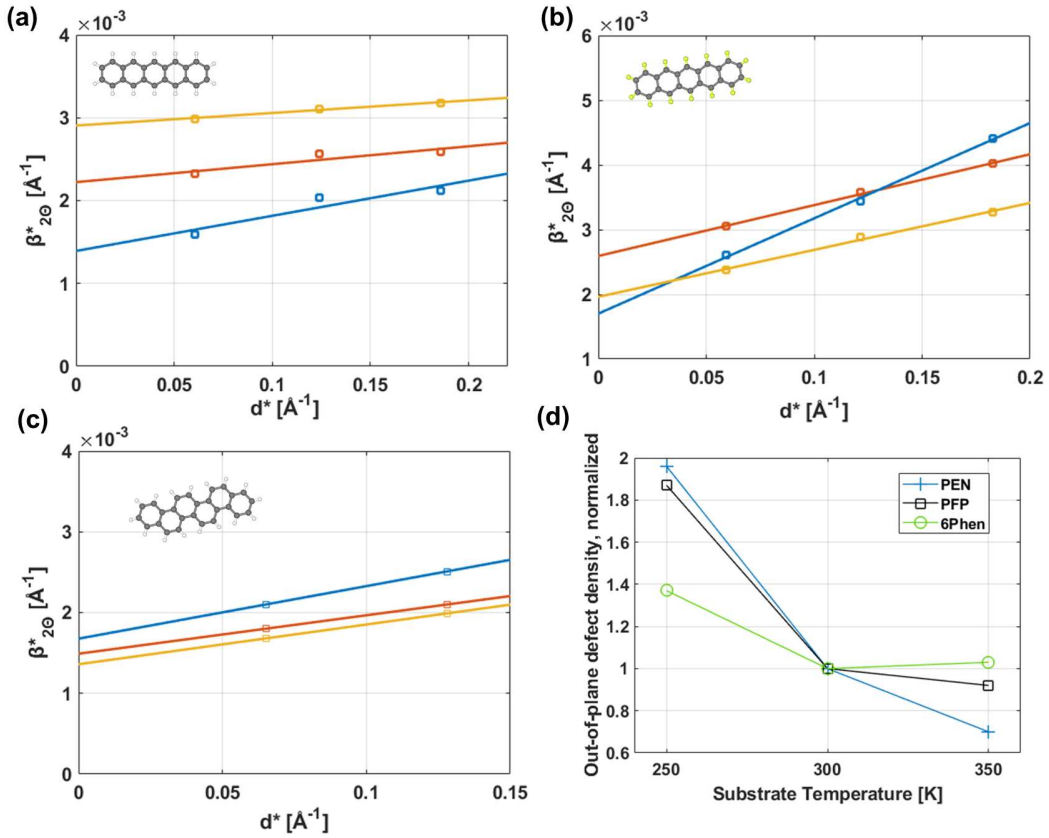

Figure 5.11: The Williamson-Hall analysis allows to separate the effect of strain induced by structural defects and instrumental broadening. The resulting slope denotes the maximum strain, which is proportional to the distortion of the crystal lattice. Shown are WHA plots for (a) PEN, (b) PFP and (c) [6]Phenacene. For C60, a WHA is not feasible due to the lack of out-of-plane Bragg reflections. Generally, a low substrate temperature during growth has a strong impact on the defect density with a greater slope for all the compounds. The growth at higher temperatures, however, only has a minor impact with the defect density staying close to the reference sample and even increasing for the [6]Phenacene sample.

The last approach studying the out-of-plane defect density is based on a method introduced by Nickel et al. [193]. Due to dislocations and distortions, the reciprocal lattice points of a real crystal are misoriented and displaced relative to the ideal lattice resulting in a diffuse scattering signal. The increasing width of the diffuse scattering signal in rocking scans can be converted into a defect density. By analyzing the broadening solely in direction of the surface normal (i.e. along (00L) reflections) one is able to extract the density of defects in the out-of-plane direction. Fig. 5.12 (a)-(d) shows the dependence of the FWHM (as k_{II}^{D}, obtained from Gaussian fits to the diffuse scattering signal) on

the momentum transfer L. The linear slope increase can be directly converted into the defect density, in the case of a constant film thickness. As apparent from the normalized defect density shown in the insets, a strong decrease of the out-of-plane defect density when changing from low to room temperature for all investigated systems is found. On the other hand, a change of growth temperature from room temperature to high temperature has a much weaker impact on defect density (also compared to the other kinds of examined defects). For PFP even a small increase in the number of out-of-plane defects at higher temperature is observed.

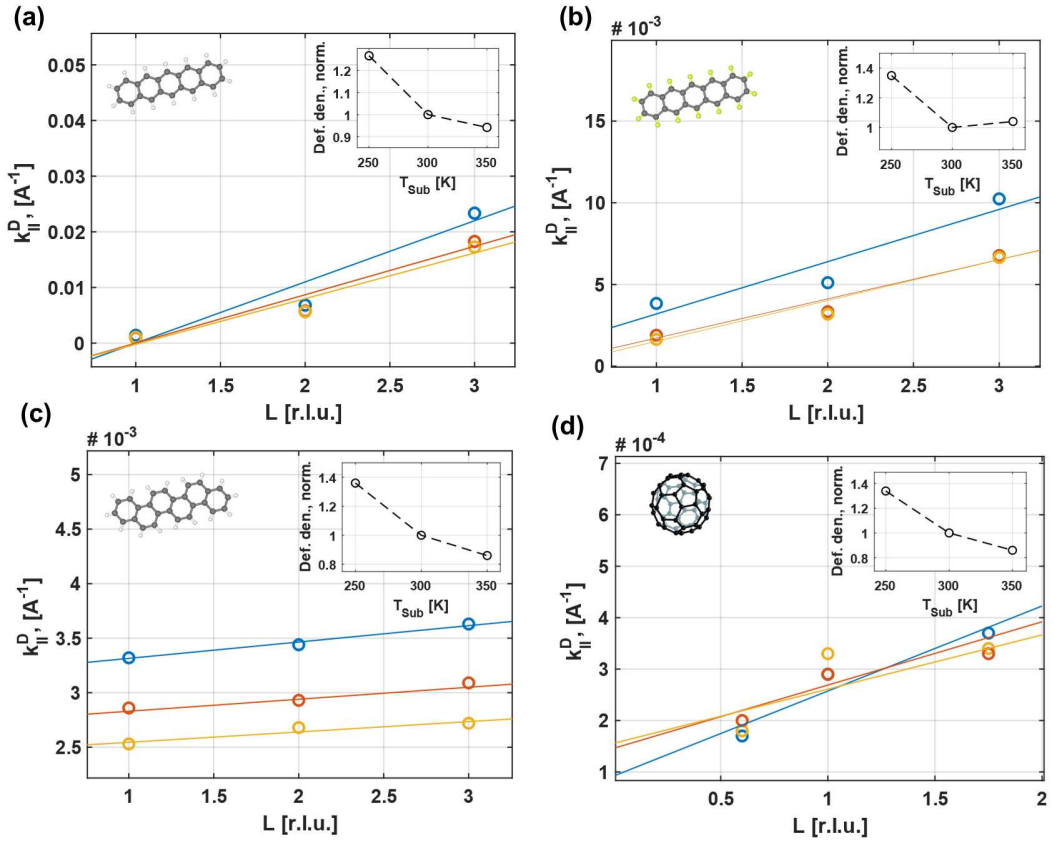

Figure 5.12: Following a method introduced by Nickel et al., the FWHM of the diffuse scattering k_{II}^{D} is given as a function of reduced lattice units for (a) PEN, (b) PFP, (c) [6]Phenacene and (d) C60. From the slope of the respective linear fits, the defect density in the out-of-plane direction can be calculated. The insets show the resulting defect density normalized to the respective room temperature sample. For all compounds an increase of defect density with decreasing substrate temperature is observed.

5.1.1.3 Electronic properties - gap state density and ELA

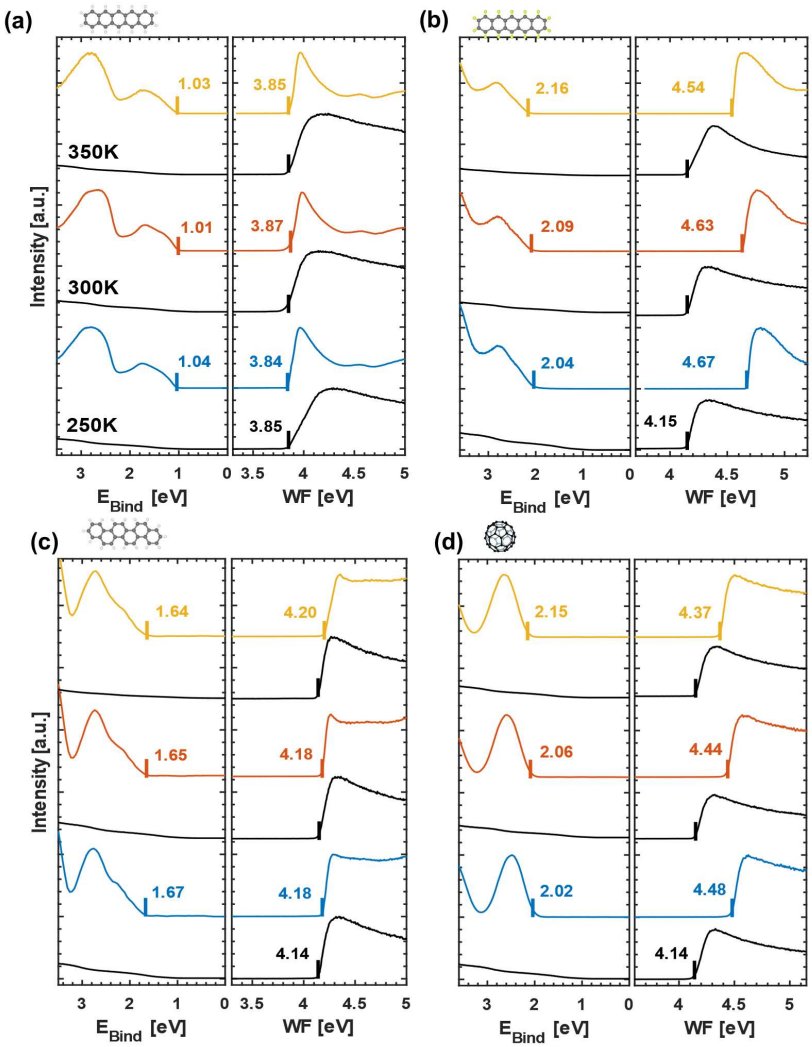

Figure 5.13: HOMO and SECO regions obtained from UPS measurements for (a) PEN, (b) PFP, (c) [6]Phenacene and (d) C60. The vertical lines and the given values correspond to the onset of the respective HOMO DOS and SECO. The observed SECO shift between the substrate and organic SECO gives the interface dipole between them. The overall shape of the HOMO distribution is not affected by a different growth temperature.

UPS Data The electronic properties of the different thin films were investigated using UPS. Figure 5.13 shows the measured spectra for the OSCs as well as for the SiO_2 substrates (black). The vertical lines indicate the exact position of the onset for the HOMO DOS and the SECO region. The shift of the SECO measured for the substrate and the organic film corresponds to the interface dipole. Since UPS is a highly surface sensitive technique, only the top few molecular layers contribute to the UPS signal. It is noted that the overall shape of the respective HOMO distributions is not affected by a different growth temperature and that the substrate work function is constant for one sample set.

Gap state density Figure 5.14 shows the HOMO gap state regions of (a) PEN, (b) PFP, (c) [6]Phenacene and (d) C60. To visualize the change in gap state density the spectra for each compound are shifted to align with their respective HOMO edge (which corresponds to the onset in linear scale (see Fig. 5.13), the energy values are given relative to that. First it has to be noted that for each compound the density of electronic gap states scales with the substrate temperature. As a general feature an increase of gap states going from the high temperature samples to room temperature to the low temperature samples is observed. The shape of the electronic gap states varies for different compounds and temperatures, however, it can generally be approximated by an exponential tail, indicated by straight lines on the logarithmic scale in Fig. 5.14 (the fitting parameters are shown in Tab. 5.1). The slight deviation of the low temperature samples of PEN and [6]Phenacene could point towards the influence of a predominant type of structural defect resulting in a relatively well-defined density of additional states. Also, for the general trend it seems not possible to identify any specific dependency on molecular characteristic such as shape or polarity, suggesting that the phenomenon is widespread and expected to be also found in thin films of other compounds. For better comparison, the density (i.e. the integrated area below the exponential tail and above the background signal (grey rectangle)) is normalized to the area of the respective room temperature sample and displayed in the insets. This can now be used to correlate the density of electronic gap states to the different types of structural defects for the different organic molecules.

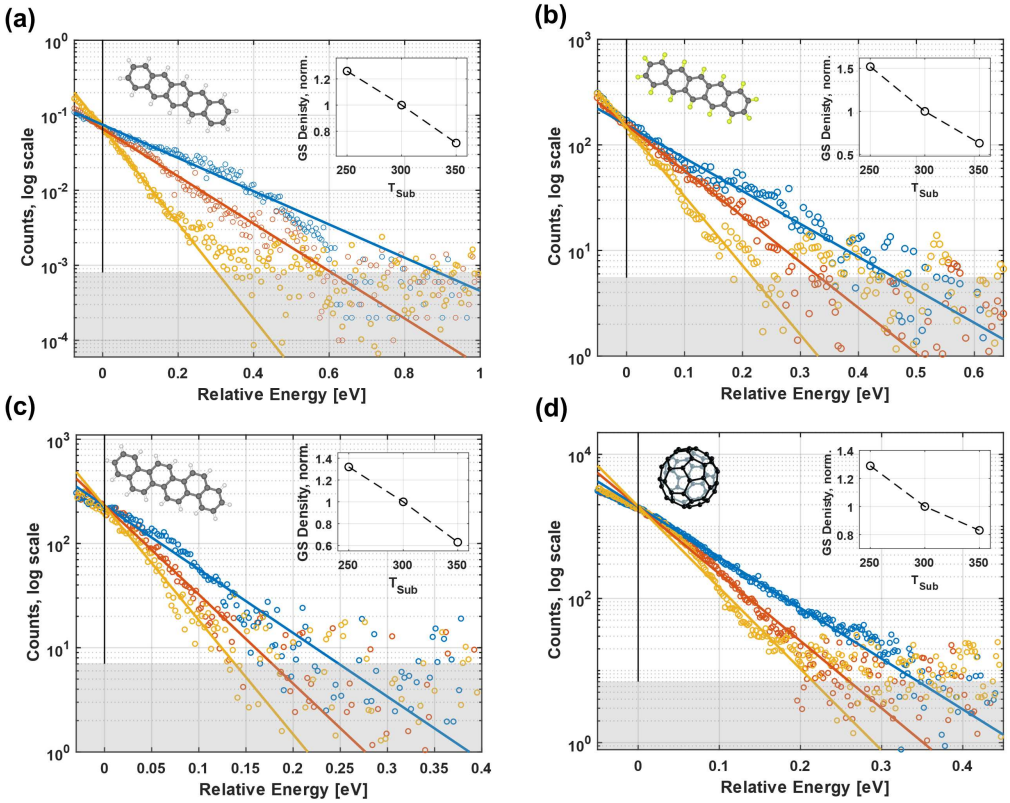

Figure 5.14: Ultra-low background UPS spectra of the gap state region for (a) PEN, (b) PFP, (c) [6]Phenacene and (d) C60. The colors correspond to the substrate temperature during growth. The spectra are shifted horizontally to the respective HOMO edges to allow for a better comparison. The straight lines approximate the observed gap state densities occurring as exponential tails reaching into the band gap. The insets show the relative amount of gap states normalized to the respective room temperature sample.

Table 5.1: Fitting parameters for the exponential fits to the gap state density, indicated as straight lines in Fig. 5.14. Equation: ae^{bx}

PEN	a	b	**PFP**	a	b
250K	0.069	-4.57		154.1	-6.54
300K	0.065	-7.27		154.2	-9.97
350K	0.067	-14.6		147.9	-15.12
[6]Phenacene			**C60**		
250K	230.7	-14.06		1874	-16.18
300K	232.3	-19.69		1888	-21.48
350K	228.4	-25.20		1899	-25.98

Energy-level alignment Lastly, the impact of the gap state density on the interface dipole (ID) between substrate and the organic thin film is studied. Figure 5.15 shows the ELA of (a) PEN, (b) PFP, (c) [6]Phenacene and (d) C60 on the silicon substrate. In general, within the gap state model, the ELA between substrate and organic film is governed by the energy distance between the substrate Fermi energy and the HOMO (LUMO) distribution, as well as, the exact shape of the distribution [46]. As shown in Fig. 5.14, the density distribution of gap states depends strongly on the substrate temperature during growth and differs for the investigated systems. For example, the extension of states may reach an additional 100 meV for low temperature [6]Phenacene and as much as 400 meV for the low temperature PFP into the electronic gap compared to the respective high temperature sample.

It has to be noted that, so far, due to experimental restrictions, only a direct measurement of HOMO gap states is possible. The direct detection of gap states reaching out from the LUMO level, which is principally accessible with inverse photoelectron spectroscopy (IPES), is still elusive. However, the impact of an altered LUMO gap state density on the ELA can be studied using a conventional UPS set-up and is evident from the PFP and C60 data, where a positive ID (indicated in red) can be observed. This can be attributed to a charge transfer through tunnelling from the substrate into the empty LUMO gap states of the organic layer [46, 204]. Since the substrate work function was identical for most of the compounds, a change in magnitude in the ID can be exclusively ascribed to the broadening of the LUMO distribution (i.e. gap state density). With more gap states accessible, more electrons can be transferred, thus leading to a higher observed ID. For PEN and [6]Phenacene, the energy barrier between Fermi energy to both, the HOMO and LUMO states is too large, leading to no transferred charges and no gap state density dependent ID can be observed. The LUMO positions (EA) indicated here are taken from IPES measurements found in literature: EA_{PEN}=2.35 eV [205], EA_{PFP}=4.12 eV [205], EA_{C60}=3.98 eV [206]. For [6]Phenacene, no IPES data can be found. However, the electron affinities of the closely related [5]- and [7]Phenacenes are 3.2 eV [144] for [5]Phenacene and 3.1 eV [144] for [7]Phenacene. Assuming a linear dependence of the energy gap width as for acenes, the EA of [6]Phenacene is estimated to be 3.15 eV.

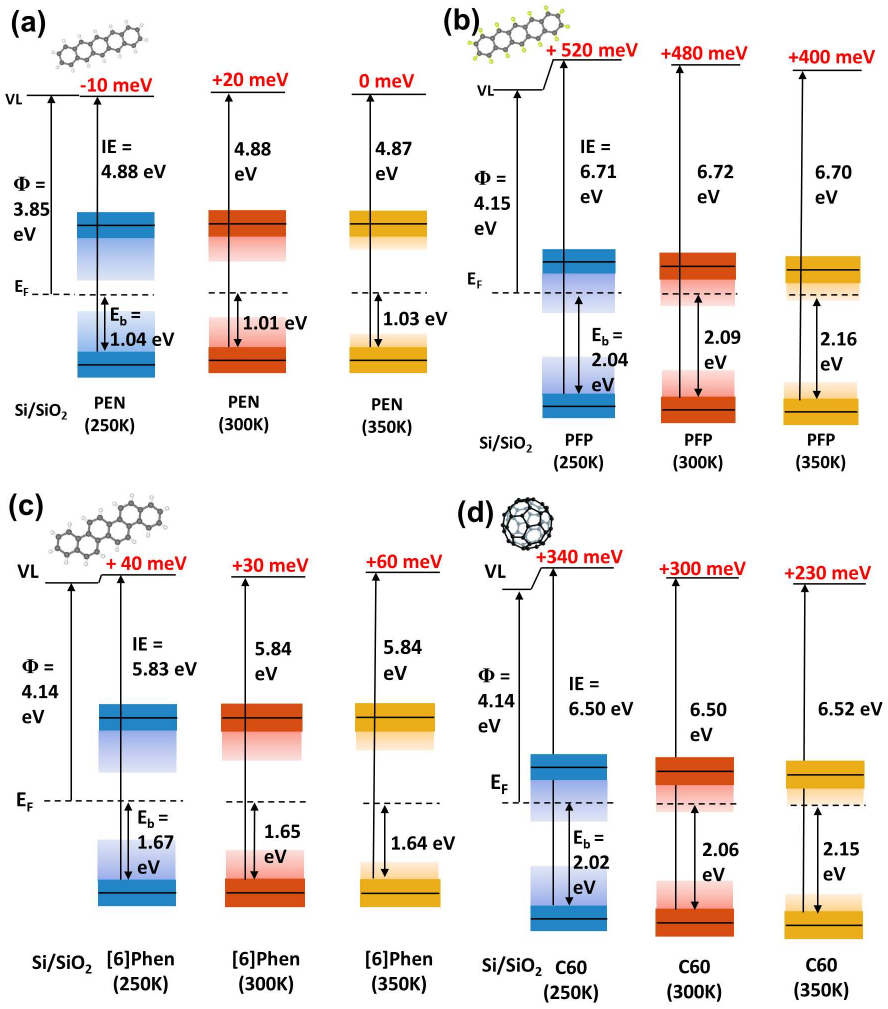

Figure 5.15: Schematic representation of the ELA of (a) PEN, (b) PFP, (c) [6]Phenacene and (d) C60. For PFP and C60 a positive interface dipole (ID, indicated in red), resulting from electrons moving from the substrate into the 'empty' LUMO states, dependent on the gap state density can be observed. For PEN and [6]Phenacene, the energy barrier between substrate Fermi energy to both, the HOMO and LUMO states is too large, leading to no transferred charges and no gap state density dependent interface dipole.

5.1.1.4 Summary and conclusion

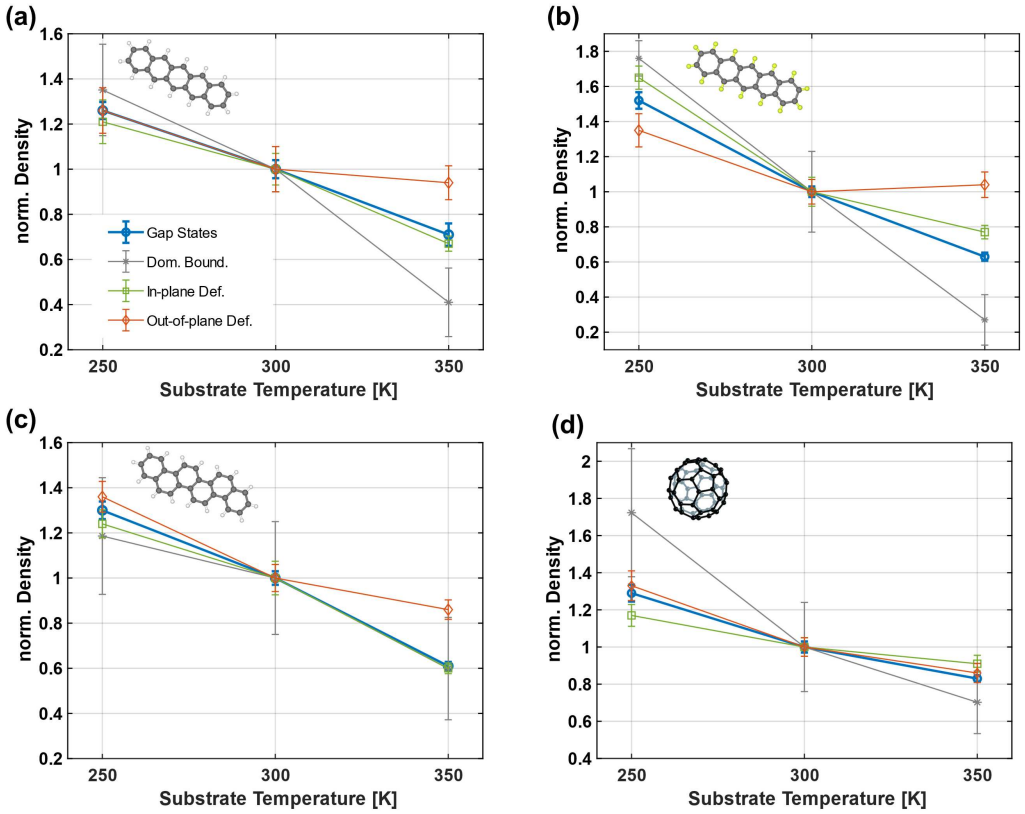

Figure 5.16: Comparison between the normalized gap state density and normalized defect density for different kinds of structural defects (for the out-of-plane defect density, the data obtained from the Nickel-analysis is used). In general, the density of all types of defects decreases with higher substrate temperature. The exact temperature dependence, however, is somewhat different. Notably, the in-plane defect density obtained from the coherently scattering island size D_{coh} is in good agreement with the gap state variation.

The impact of different structural defects on the gap state density of four prototypical OSCs as well as the role of such defects in the ELA by complementary X-ray scattering, AFM and ultra-low background UPS measurements was studied. Varying the growth temperature of the respective thin films allows to control the density of electronic gap states, with a lower temperature leading to a higher density of observable states. Comparing the dependence of gap states and structural defect density on growth temperature the two aspects can be linked and even pinpoint the impact of defects of different spatial distribution and length scale.
In Fig. 5.16, the gap state density and the different defect densities are summarized (for the out-of-plane defect density, the data obtained from the Nickel-analysis is included). In general, the density of all types of defects decreases with higher substrate temperature,

however the exact temperature dependence is somewhat different. Notably, the in-plane defect density obtained from the coherently scattering size D_{coh} is in good agreement with the gap state density variation. Since gap states are thought to result from deviations in the overlap of molecular orbitals and the rod-like compounds grow standing up and in a layered fashion, the overlap is mainly localized inside planes parallel to the substrate. A smaller (in-plane) D_{coh}, i.e. more strain, defects and dislocations has therefore a large impact and a strong influence on the precise electronic landscape of the thin films.

This assumption is further confirmed by the C60 data. Since C60 is a spherical molecule, the molecular orbitals are uniformly distributed in every spatial direction and the impact of defects on the gap state density is expected to be independent of a predominant direction [207]. As can be seen Fig. 5.16 (d), this is the case with an overall decrease of defect density and the gap state density following the trend of both out-of-plane defect density and the in-plane defect density. Additionally, a key factor governing the ELA at the substrate/organic interface are the energy gap between substrate Fermi energy and HOMO/LUMO states and the exact distribution of the density of gap states. If the energy barrier between the substrate Fermi energy and the HOMO/LUMO states is small enough, an interface dipole, due to charge transfer, can be observed. Its magnitude depends strongly on the gap state density with more charges transferred when the substrate temperature is decreased during growth.

In summary, by adjusting the density of structural defects (e.g. by temperature variation) the ELA at inorganic/organic interfaces can be controlled. This opens up new possibilities for tuning the functionality and increasing the efficiency of devices based on organic semiconductors such as organic light emitting diodes (OLEDs) or organic solar cells.

5.1.2 Gap states induced by structural doping

In this section, the defect density is not controlled by a change of substrate temperature during growth but through a mixing of two compounds: [5]Phenacene and [6]Phenacene. Both belong to the family of phenacenes and while [5]Phenacene consists of five benzene rings fused together in a zig-zag manner, [6]Phenacene is built-up of six rings. Therefore, they only differ in their length and the two shorter dimensions are similar. This makes them perfectly suited to be co-evaporated and forming a so-called solid solution (Fig. 5.17), in which a continuous or nearly continuous mixing behaviour, without phase separation, is expected. As a result, the one or the other compound is incorporated into the host unit cell and point defects are created. Generally, within the concept of structural compatability in solid solutions, molecules of similar length are mixing well and molecules with very different length exhibit phase separation due to induced stress. Since the length difference is comparably small, the amount of point defects and, with that, induced stress can be controlled by the mixing ratio. Electronically, the properties of [5]- and [6]Phenacene are expected to be well preserved [144], which allows to study the effect of an altered defect density (by mixing) on the gap state density of the blends. Besides thin films of the pure compounds, blends with mixing ratios of 3:1, 1:1, 1:3 were grown at room temperature on SiO_2 with a rate of 2 Å/min up to a thickness of 20 nm.

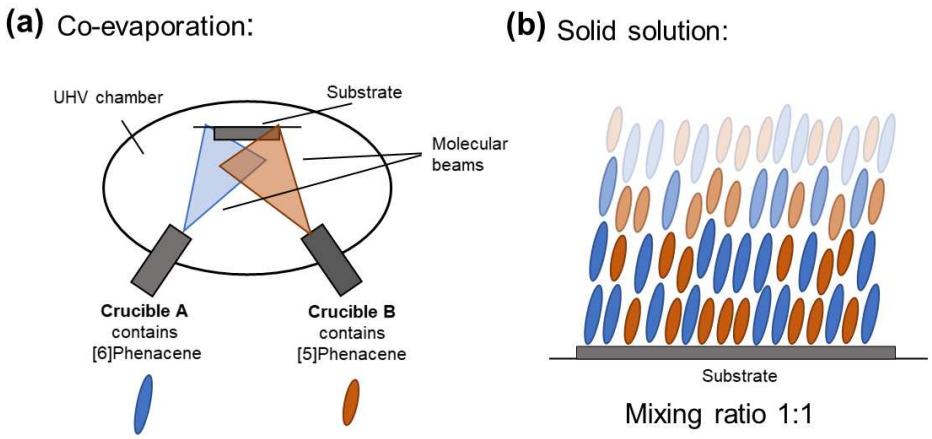

Figure 5.17: (a) Schematic representation showing the principle of co-evaporation. Two different materials are loaded in crucibles and installed in an UHV system. Simultaneously heating both crucibles, the molecules enter the gas phase and are deposited onto the substrate at the same time. Careful selection of molecular flux allows to control the mixing ratio in the resulting thin film. (b) If the two molecules are sterically compatible and have comparable interactions energies they mix on the molecular level and form a solid solution without any phase separation. One molecule is thereby statistically incorporated into the unit cell of the other introducing point defects.

5.1.2.1 Structural properties

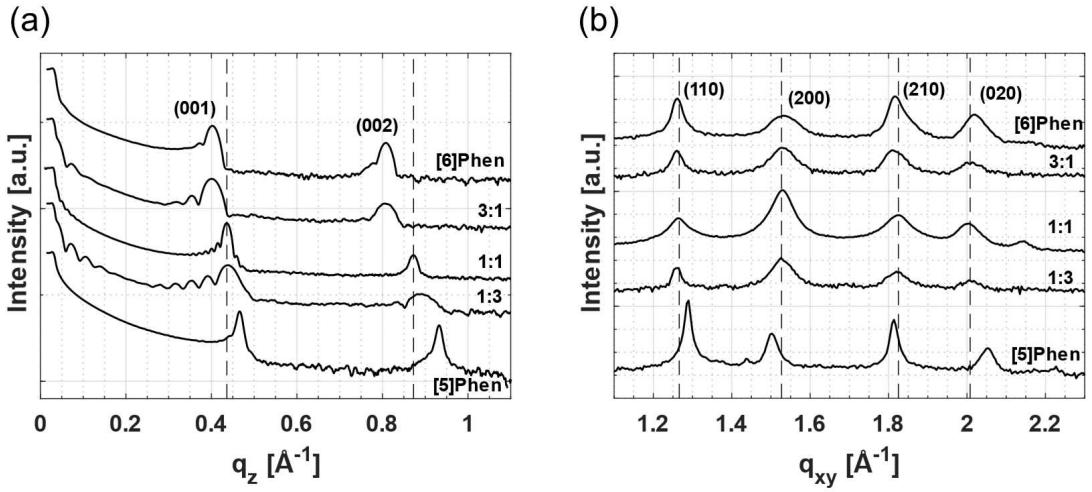

Figure 5.18: Structural data of the mixing series [6]Phenacene:[5]Phenacene. (a) XRR spectra of pure [6]Phenacene (top), [5]Phenacene (bottom) and for the different mixing ratios. Independent of the mixing ratio, the molecules adopt a standing up configuration with the long axis parallel to the substrate normal. The shift of the Bragg reflection is correlated with the mixing ratio. (b) Corresponding GIXD data. Mixing of [5]- and [6]Phenacene has only a small impact on the in-plane arrangement of molecules indicating that the molecules, in fact, are mixing on the molecular level.

In-plane and out-of-plane structure Figure 5.18 (a) shows XRR data for [5]Phenacene and [6]Phenacene films as well as the blends in different mixing ratios. As a reference the Bragg peak position of the 1:1 mixture is indicated. In all cases pronounced (001)- and (002)-Bragg reflections are observed, indicating a high ordering behaviour in the out-of-plane direction. Interestingly, the peak position is shifting corresponding to the mixing ratio. This can be rationalised with the random mixing of molecules in the out-of-plane direction. Since XRR probes the mean electron density along the z-axis, a random composition would lead to a linear change in the electron density with increasing ratio of the longer (or shorter) molecule. This can be visualized by a step-by-step incorporation of [6]Phenacene into the unit cell of [5]Phenacene. For a given mixing ratio, the longer molecule would be at random positions within the [5]Phenacene lattice and increasing the electron density slightly just above the [5]Phenacene molecules (see also Fig. 5.17). The more [6]Phenacene molecules are incorporated, i.e. increasing the mixing ratio, the more the electron density shifts towards the one of the latter.

In all mixtures, Kiessig- and Laue oscillations can be observed, indicating smoother films compared to the pure, single component films. The effect is especially pronounced in the blends with a 3:1 and 1:3 mixing ratio. In (b), the GIXD spectra of the respective films are shown. The positions of Bragg reflections differ only slightly and no new peaks

appear in the mixed systems. The appearance or vanishing of peaks would indicate the formation of a new structure or mixing-phase. Since this is not the case and from the linear shift of the Bragg peak position in XRR, one can conclude a total intermixing as a result of similar intermolecular interactions caused by the same composition and structure of the two molecules. Apparently, the strain induced by some degree of steric incompatibility due to the different length is not enough to lead to phase separation or the formation of a new crystal phase.

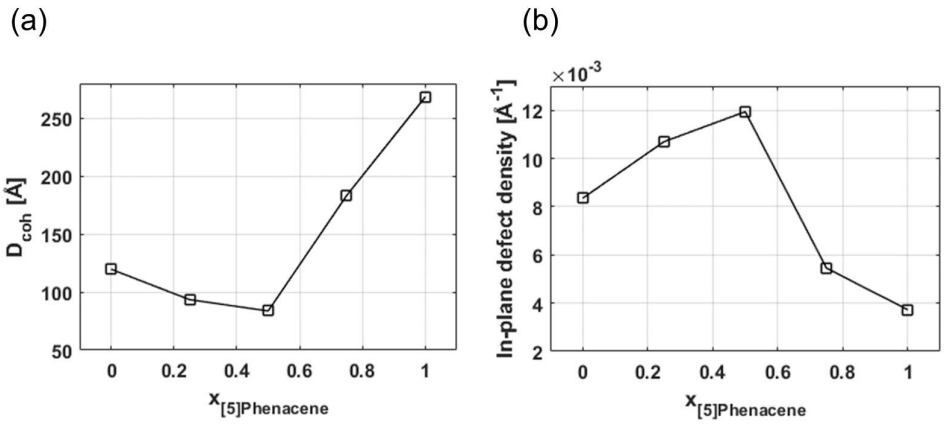

Figure 5.19: Defect analysis of the pure [5]- and [6]Phenacene films as well as the blends in different mixing ratios using the GIXD data presented in 5.18 (b). (a) D_{coh} as a function of [5]Phenacene content. D_{coh} is considerable larger for pure [5]Phenacene and the 1:3 blend, the 1:1 mixture marks the minimum as expected from literature [127]. (b) contains the corresponding in-plane defect density obtained via $1/D_{coh}$. Increasing the [5]Phenacene content leads to an increase of defects for the 3:1 and 1:1 blends but a significant decrease is found for the 1:3 mixture and the pure [5]Phenacene film.

In-plane structural defects Following the results obtained in the preceding section, the discussion of structural defects focuses on areal in-plane defects. Again, the width of Bragg reflections in the GIXD scans (Fig. 5.18 (b)) is analysed in terms of the FWHM and the coherently scattering island size, D_{coh}, is obtained through Scherrer's formula. In Fig. 5.19, the results are summarised. The highest crystal quality is found for pure films of [5]Phancene and the 1:3 mixture with an excess of [5]Phenacene. Generally, mixing has a strong impact on the crystallinity of the thin films leading to an overall u-shape with the 1:1 blend as the minimum. This result was already reported in literature for different, statistically intermixing systems and is generally related to a modified step-edge barrier in the blends [127]. D_{coh} of pure [6]Phenacene is considerably smaller compared to pure [5]Phenacene and as a result, the corresponding defect densities in the former are signficantly larger (shown in (b)). The overall behaviour is mirrored and a maximum defect density is found for the 1:1 blend, while the pure [5]Phencene shows the least defects.

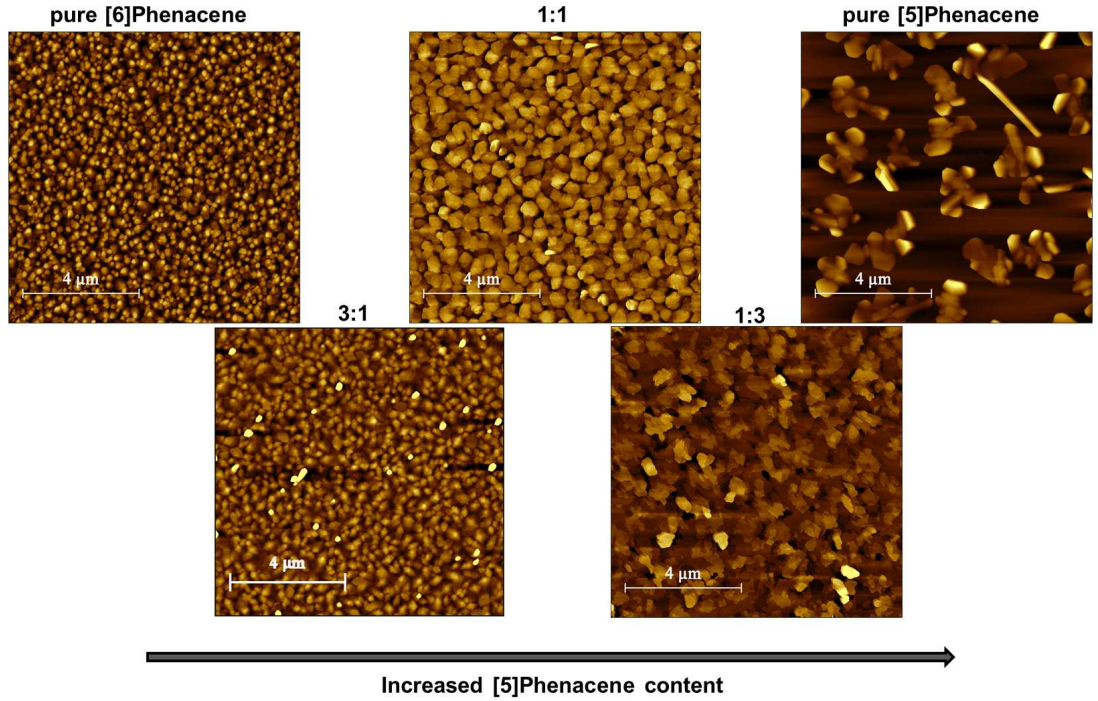

Figure 5.20: Morphology of the different blends measured via AFM. From left to right the [5]Phenacene content is incrementally increased. [6]Phenacene shows the typical wedding-cake island shape already observed in the preceding section. Increasing the mixing ratio leads to a significant change and the islands resemble more and more the islands of pure [5]Phenacene. Also, the wetting behaviour is different. Whereas pure [5]Phenacene shows a dewetting of the substrate surface, already a rather small amount of [6]Phenacene in the blend is enough to achieve the formation of complete wetting.

Morphology and domain boundaries The morphology of the respective thin films was investigated and compared using AFM. The resulting images for the pure films and different mixing ratios are shown in Figure 5.20. From left to right, the [5]Phenacene content is increased. Probably the most prominent, overall difference is in the wetting behaviour, especially apparent for the [5]Phenacene thin film, where areas of the substrate are visible. In contrast, the blends as well as the [6]Phenacene film are completely covering the substrate surface. Apparently, only a small amount of the longer molecule is enough to change the wetting behaviour completely, which might be connected to a modified Ehrlich-Schwöbel barrier and an increased downhill transport of molecules for the mixed systems [127]. Also, the island shapes are changing with mixing ratio. While pure [5]Phenacene shows quite sharp edges and a very characteristic shape, with increasing percentage of the longer molecule, the island shape transforms stepwise to the shape of the pure [6]Phenacene sample. To obtain a measure for the difference in domain boundary length, the progression of the correlation length is depicted in Fig. 5.21. A linear increase is observed, corresponding to an increase in the mean peak-to-peak distance between

adjacent domains, already visible by eye. Keeping the investigated area (i.e. the area of the AFM image) fixed, the correlation length can be used to estimate the density of structural defects resulting from domain boundaries, which are, in turn, inversely proportional to the correlation length. As a conclusion, a linear increase of domain boundary length for the blends with higher [6]Phenacene content is found.

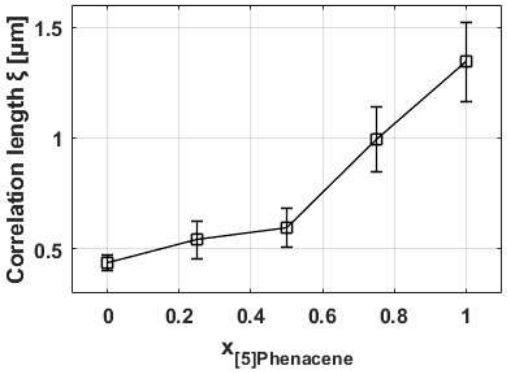

Figure 5.21: The progression of the correlation length extracted from the AFM images shown in Fig. 5.20. Increasing the content of [5]Phenacene leads to a linear increase in correlation length, which describes an increase of the mean peak-to-peak distance. For a fixed area, the mean distance between peaks can be used to estimate the boundary length between adjacent domains, which is, in turn, inversely proportional to the correlation length. In conclusion, an increase of [5]Phenacene in the blends leads to more defects from domain boundaries.

5.1.2.2 Electronic properties

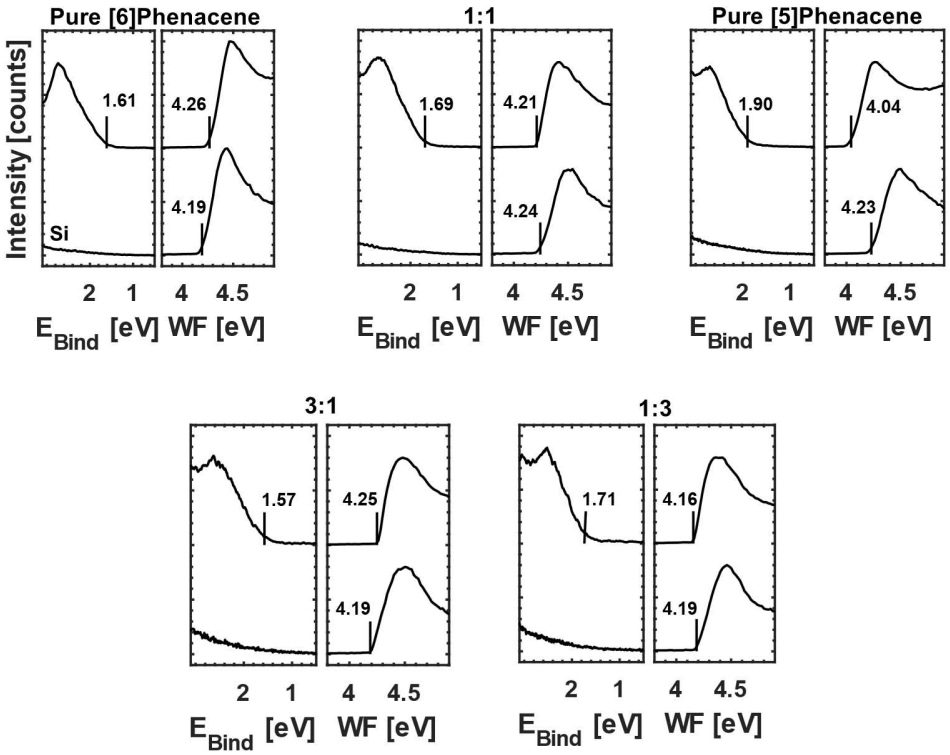

Figure 5.22: UPS spectra of pure [5]- and [6]Phenacene thin films (top left and right) and the blends with the respective mixing ratio given above each panel. Additionally, the measurement from the SiO_2 is shown. Indicated by the vertical lines are the HOMO (left) and SECO onset (right). Due to the similar molecular structure of [5]- and [6]Phenacene, the HOMO shape does not differ significantly and the HOMO shape in the blends is well preserved.

UPS Data In Fig. 5.22, the HOMO and SECO region, measured at the FUNSOM institute in China, is presented. The vertical lines indicate the respective HOMO and SECO onset. The data of the pure compounds is depicted in the top left ([6]Phenacene) and top right ([5]Phenacene) panels, at the bottom, the signal from the silicon substrate is shown. The work function of the substrate shows only a rather small variation of $\pm 50\,\mathrm{meV}$. Moving from left to right, the amount of [5]Phenacene is increased and the mixing ratio is specified above the respective panel. As expected, since [5]- and [6]Phenacene are structurally closely related, the HOMO shape does not differ significantly and is well preserved in the blends. The binding energy is shifted towards larger values with increasing [5]Phenacene content by $\sim 300\,\mathrm{meV}$.

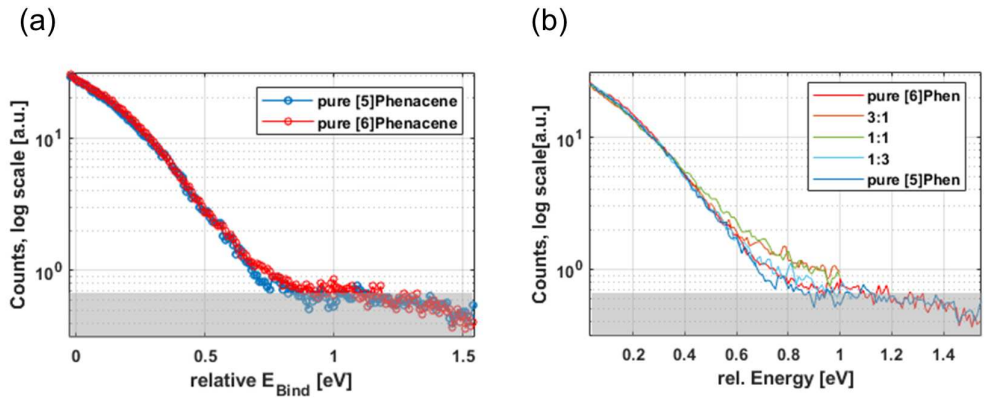

Figure 5.23: UPS spectra of the gap state region for (a) the pure [5]- and [6]Phenacene thin films and (b) with data from the respective blends included. The data is plotted on a logarithmic scale and shifted to be aligned at the same HOMO edge. The gap state densities of the pure compounds only show a small difference with a slight increase in the [6]Phenacene thin film. While the 1:3 mixture exhibits a density comparable to [6]Phenacene, significantly more gap states are observed in the 3:1 and 1:1 mixture. This result corresponds well with the density of structural defects obtained from D_{coh} and further highlights the impact of areal in-plane defects on the gap state density.

Gap state density The gap state region is depicted in Fig. 5.23. The data is plotted on a logarithmic scale and shifted to align at a similar HOMO edge. (a) shows the gap states of the pure compounds [5]Phenacene (blue) and [6]Phenacene (red). As expected, the overall shape is rather similar, however, a slight increase in gap state density for the [6]Phenacene sample is observed. In (b) also the gap state regions of the different blends are included. The blend with a mixing ratio of 1:3 exhibits a density comparable to the one of [6]Phenacene, while for the 1:1 and 3:1 mixtures a significant increase in gap state density is observed. This result, in fact, corresponds well to the progression of structural defects obtained from D_{coh}, where the maximum amount of defects was found in the 1:1 and 3:1 blends and the crystallinity of the other three samples was significantly increased.

Comparing the trends of structural defects obtained from D_{coh} and from domain boundaries with the trend of gap state density allows for further conclusions regarding the source of gap states. While the defects from domain boundaries showed a linear behaviour with increasing one or the other compound (Fig. 5.21), the smaller areal defects showed a behaviour resembling an inverted u-shape (Fig. 5.21). If the domain boundaries were the main source of gap states, one would expect the 1:1 mixture to have a lower gap state density compared to pure [6]Phenacene and the 3:1 blend. However, since the density is significantly larger, respectively rather similar, one can preclude domain boundaries as the main source of gap states. This further highlights the impact and role of small areal in-plane defects on the gap state density and confirms the conclusion made in the previous part.

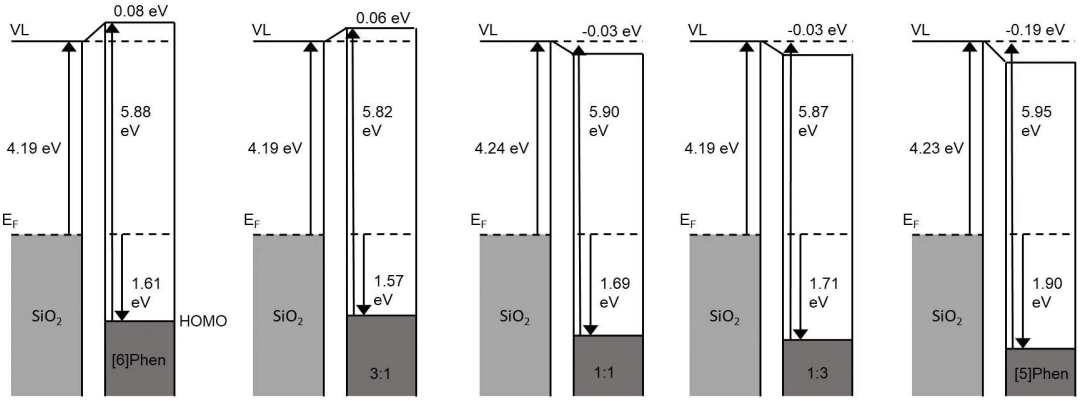

Figure 5.24: Schematic representation of the ELA from pure [6]Phenacene (left) to pure [5]Phenacene (right) with the blends in increasing mixing ratio in between. As expected, the thin films only show a small and gap state independent ID with the exception of pure [5]Phenacene. In this case, further studies are needed to investigate the reason for the rather large and negative ID.

Energy-level alignment For a complete description of the electronic properties, also the ELA of the mixing series is presented. In Fig. 5.24, a schematic representation of the data shown in Fig. 5.22 is depicted. Since the energy distance between substrate Fermi energy and the HOMO/LUMO distributions is anticipated to be too large for any charges to be transferred, no gap state dependent ID is expected. This is clearly the case, with only small IDs observed for all samples except the pure [5]Phenacene film. The rather large ID of -190 meV is too high for the ELA to be considered the result of vacuum level alignment. Two reasons might explain this somewhat unexpected behaviour. For one, the measurement could be faulted by the position of a screw needed to fixate the sample on the sample holder. Since the measurement is very sensitive to the material properties, already only partial illumination with the photon beam could alter the measured SECO. To avoid any disturbance of that kind, generally, three measurements were conducted at different positions. However, in this case, they only differ by ~ 50 meV, respectively, not explaining the observed result. A second reason could be related with the observed slightly increased IE of [5]Phenacene. As shown in [147], [5]Phenacene exhibits a dependence of the IE on orientation of the molecules relative to the substrate normal. Increased values of IE are found for more lying down molecules. In the presented case, the IEs for the blends with an excess of [5]Phenacene and for the pure compound are generally higher than expected from literature. This could hint towards a small amount of [5]Phenacene molecules adopting a lying-down configuration, which could potentially change the ELA mechanisms considerably [208]. Further investigation is needed to ultimately investigate the reason for this behaviour and to decide if the ID changing stepwise from +80 meV for the pure [6]Phenacene to -190 meV for pure [5]Phenacene with increasing [5]Phenacene content is simply appearing by sheer chance or if there is any systematic dependence of the ID on the mixing ratio.

5.1.2.3 Summary and conclusion

Thin films of [5]- and [6]Phenacene, as well as blends in mixing ratios of 3:1, 1:1 and 1:3 were grown and investigated using X-ray scattering, AFM and UPS measurements. It was found that the molecules mix on the molecular level and that the molecular arrangement is only slightly affected by mixing. The length difference between [5]- and [6]Phenacene is small enough to not induce any strain leading to phase separation, however, mixing of the compounds had a strong impact on the thin film morphology and the crystallinity of the samples. For the small areal defects, obtained from the coherently scattering island size, a maximum defect density was found for the 1:1 mixing ratio, while the pure [5]Phenacene thin film did exhibit the least defects. From an analysis of the correlation length from the AFM images, a linear increase in domain size from [6]- to [5]Phenacene was found, which inversely proportional to the domain boundary length.

UPS measurements revealed an increase of gap states in the mixtures compared to films of the pure compounds. Comparing the trend of the gap state increase with the trend of the domain boundary length and the small areal defect density, a correlation between gap states and the latter is found. This result is in good accordance to the results gained in the preceding part of this section, further strengthening the assumption of in-plane defects being the main source of gap states.

In summary, mixing of two sterically compatible and electronically similar compounds is an efficient way to control, for one, structural properties in terms of defects and, on the other hand, control the density of gap states within the film.

5.2 Gap states and energy-level alignment in heterostructures

The following section is based on [209]. Generally, organic electronic devices comprise a stack of different organic layers (Fig. 5.25 (a)), for which every neighbouring and interconnected organic layer can be regarded as an organic-organic heterojunction (OOH) [26, 210, 211].

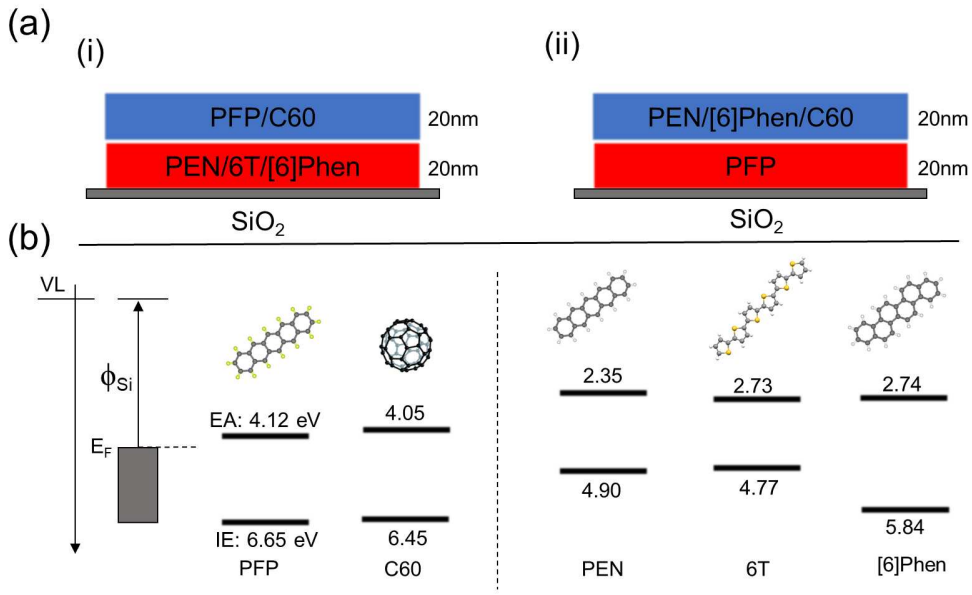

Figure 5.25: Schematic representation of the investigated heterostructures and electronic properties of the compounds. (a) Heterostructures with donor molecules as the bottom layer and acceptor molecules as top layers are investigated in closer detail. (b) Schematic representation of the different compounds, including the ionization energies (IE) and electron affinities (EA) of the acceptor molecules (left) and donor molecules (right). The silicon substrate is characterized by its work function Φ_{Si}, defined as the energy distance of the Fermi energy (E_F) to the vacuum level (VL).

At such interfaces, the ELA of frontier orbitals, plays a crucial role in determining device performance [28, 183]. In the case of OPVs, for example, the splitting of photogenerated electron-hole pairs takes place at an interface between donor- and acceptor-type OSCs and the energy offset between them is a key factor for the photocurrent generation as it defines the open-circuit voltage [212, 213]. In OLEDs, the relative energy positions of HOMO and LUMO determine the respective hole and electron injection efficiency and the offsets serve as effective blocking barriers to confine the charge carriers predominantly to the emission layer and thereby enhancing the probability of radiative recombination [214]. A model particularly suited for the description of the ELA at the OOH is based on

electronic gap states. By control of the density of structural imperfections, it is possible to control the density of gap states and their extension into the gap, which ultimately defines the ELA [45, 96].

A possibility to effectively control the structural properties of both layers in a heterostructure was demonstrated using different substrate temperatures during the growth of the bottom layer [48]. By a templating effect, the structural and morphological properties of both, the bottom layer and the layer grown on top are affected and the orientation and crystalline quality of the top layer can be adjusted [215].
In this section, the effect of the density of structural defects at the OOH on the ELA is investigated by using a combination of X-ray scattering techniques and UPS measurement. As prototypical materials relevant for device application were chosen: two different acceptor molecules (PFP and C60) and three different donor molecules (PEN, 6T and [6]Phenacene). Fig. 5.25 (b) shows their respective ionization energies (IE) and electron affinities (EA).

In the first part, PFP and C60 are deployed as the top layer, since both are expected to show a Fermi-level pinning behaviour with an gap state dependent ID. Doing so, the impact of the bottom layer on the ELA can be studied in detail. In the second part, the orientation is reversed and PFP is deployed as the bottom layer with PEN, [6]Phenacene and C60 grown on top. This allows to further investigate the defining parameters of the ELA at the OOH in terms of crystal quality and gap state density. The bottom and top layers in the heterostructure were grown to a thickness of 20 nm, respectively, with a rate of 2 Å/min. The substrate temperatures during growth of the bottom layer were set to 250, 300 and 350 K, as substrates, SiO_2 was used.

5.2.1 PFP and C60 as top layer

5.2.1.1 Structural characterization and in-plane defects

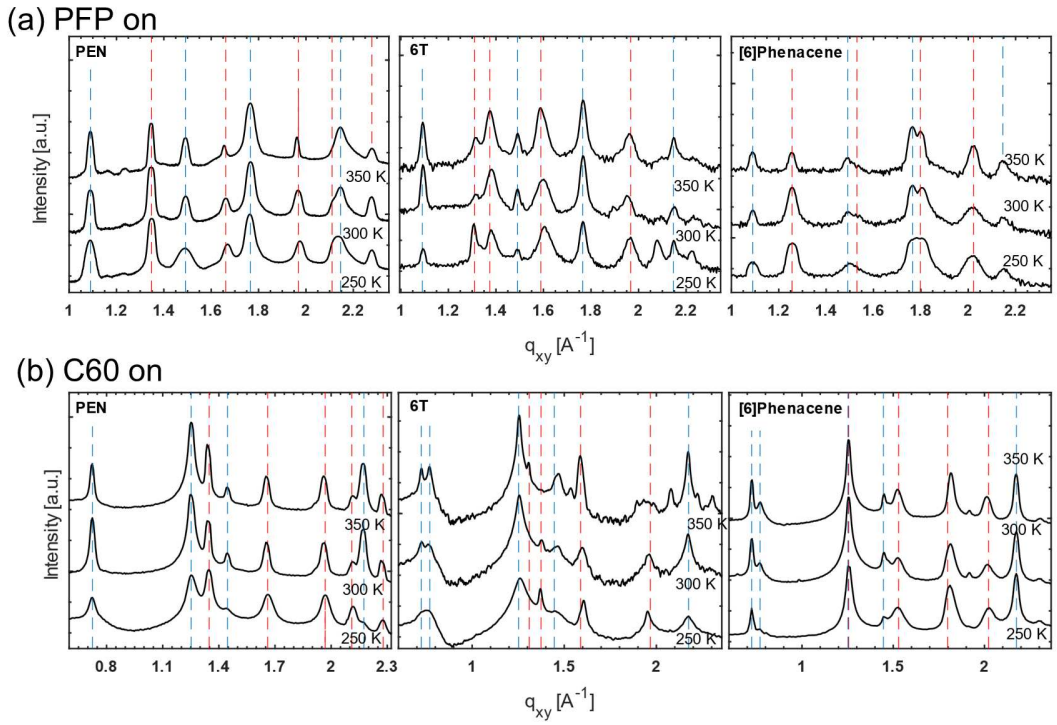

Figure 5.26: GIXD data of the investigated heterostructures: (a) PFP grown on top of PEN, 6T and [6]Phenacene. The Bragg reflections of PFP are indicated in blue, the reflections of the respective bottom layer in red. The substrate temperature during growth of the bottom layer was increased from 250 K to 300 K and 350 K. In all cases, the molecules adopt a standing up configuration, only slightly affected by the different temperatures. (b) shows the corresponding heterostructures with C60 as the top layer. The same molecular arrangement of the bottom layers is observed. From the position of C60 Bragg reflections, it can be concluded that, other than directly on SiO_2, the fcc-(111) crystal plane is parallel to the substrate surface.

First, the structural characterization of the investigated heterostructures with the underlayer grown at different substrate temperatures is presented. Figure 5.26 (a) shows GIXD data of PFP grown on 20 nm films of the respective donor molecules. All heterostructures exhibit several in-plane Bragg reflections corresponding to the bottom layer (indicated with red vertical lines) and from the PFP film (indicated in blue). The bottom layers are polycrystalline and exhibit a so-called fibre texture (2D powder), consistent with literature [197, 216, 217]. The two short unit cell axis are thereby oriented parallel to the substrate and the long axis in the out-of-plane direction. This observation is further confirmed by XRR data (shown in Fig. 5.27, for the PEN and [6]Phenacene

heterostructures), where a strong ordering in the direction perpendicular to the substrate surface is found and confirms that the molecules grow standing upright.

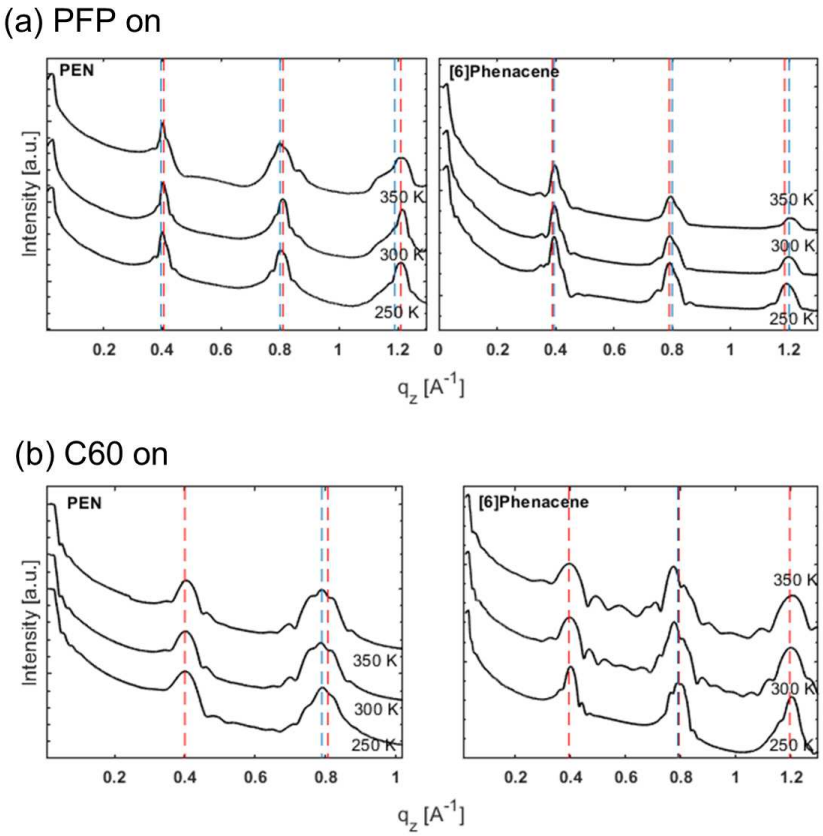

Figure 5.27: XRR data from the heterostructures with PFP (a) and C60 (b) grown on top of PEN and [6]Phenacene. The bottom layers were grwon at different substrate temperatures as indicated in the figure. For PFP, the spectra simply resembles a superposition of the pure films of both compounds grown on silicon (see, for example, Fig. 5.4). C60, however, now shows a distinct ordering in the out-of-plane direction and C60 Bragg reflections (indicated by blue lines) are observed.

The peak positions are generally only slightly affected by the different substrate temperature and no new peaks or vanishing of existing peaks is observed. The PFP grown on top shows reflections corresponding to nearly upright standing molecules with the bc-plane of the unit cell parallel to the substrate plane.

Figure 5.26 (b) shows the heterostructures involving C60 as the acceptor compound. When grown directly on SiO_2, C60 exhibits only low structural order and forms a 3D powder with randomly distributed domain orientations [218]. However, it crystallizes well on organic layers and the distribution of C60 Bragg peaks (indicated in blue) in GIXD and XRR scans reveal the alignment of the fcc-(111) crystal plane parallel to the substrate [215].

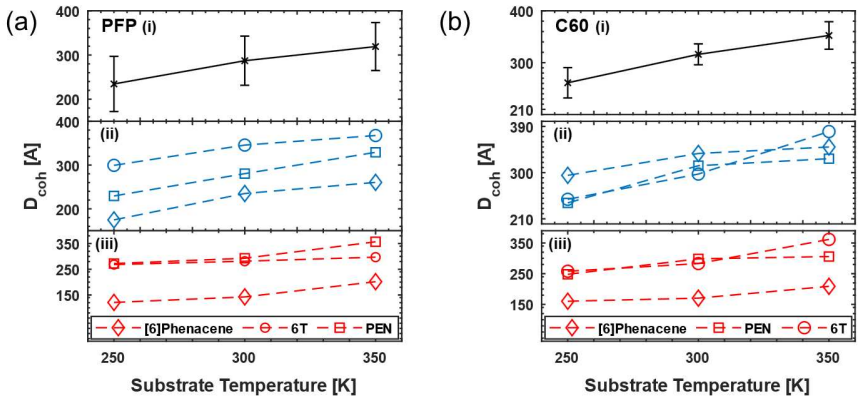

Figure 5.28: Collection of the coherently scattering island sizes D_{coh} of the heterostructures obtained from Scherrer's formula. In the bottom panel (iii), D_{coh} of the bottom layers PEN (squares), 6T (circles) and [6]Phenacene (diamonds) are shown. In the middle (ii), the corresponding D_{coh} of PFP (a) and C60 (b) grown on top are shown, the labels correspond to the respective bottom layer. The topmost panel (i) shows the averaged value of the top layer data. As a general trend, D_{coh} is increasing with increasing substrate temperature during growth, corresponding to less structural defects for elevated temperatures.

To get a measure for the defect density in the heterostructures, the in-plane coherently scattering island sizes, D_{coh}, were determined from the width of the respective in-plane Bragg reflections in Fig. 5.26. For the analysis, the widths of the bottom and top layer reflections were determined and the resulting D_{coh} averaged over all crystal directions. The results are shown in Fig. 5.28. While the absolute values differ between the compounds, as a general trend, D_{coh} is increasing with elevated substrate temperatures for the different bottom layers (shown in red) as well as the top PFP and C60 layers (shown in blue). This indicates a correlation between the crystalline quality of bottom and top layers through a templating effect. From the topmost plot in Fig. 5.28, where the average value of D_{coh} for the top layers is shown, an increase from 235 Å to 287 Å to 319 Å for PFP and from 261 Å to 316 Å to 352 Å for C60 when increasing the temperature from 250 K up to 350 K is found. As shown in previous the sections, this translates to generally less defects for higher substrate temperatures and correlates with the gap state density of the particular thin films.

5.2.1.2 Electronic properties of PFP/C60 on donor molecules

To obtain a thorough understanding of the electronic properties of the different heterostructures, UPS measurements were conducted after growth of the bottom and top layers, respectively. Figure 5.29 shows the UPS data for the heterostructures, with the PFP (a) and C60 (b) data depicted in blue and the bottom layer in red. On the respective left side, the HOMO region is plotted, on the right-hand side the corresponding SECO. The vertical lines indicate the onset of the HOMO density of states, defining the value of the binding energy (E_{Bind}) and the SECO onset, which gives the material's WF.

Interestingly, the overall HOMO shape is generally not affected by the different substrate temperatures, which is in good agreement with the preserved crystal structures observed in Figs. 5.26 and 5.27. The IEs stay constant for the top layers with only a small variation (average: $IE_{PFP} = 6.72 \pm 0.03$ eV and $IE_{C60} = 6.46 \pm 0.05$ eV). The IE of the bottom layer is partly slightly affected by the temperature variation, e.g. PEN under PFP, where the discrepancy between low and high temperature sample is found to be 140 meV (IE_{250K} = 4.84 eV compared to IE_{350K} =4.70 eV). The ELA between the SiO_2 substrates and the bottom layer shows only small IDs for all compounds and is, most importantly, not temperature dependent. This corresponds well with the gap state model of the ELA. Since the energy distance between the respective substrate Fermi energy to both, the HOMO and LUMO states is too large, no charges are transferred, and no gap state dependent ID is expected. The observed ID can by assigned to effects apparent at every interface, for example, a surface rearrangement of electrons due to the deposition of organic material on top of the inorganic substrate.

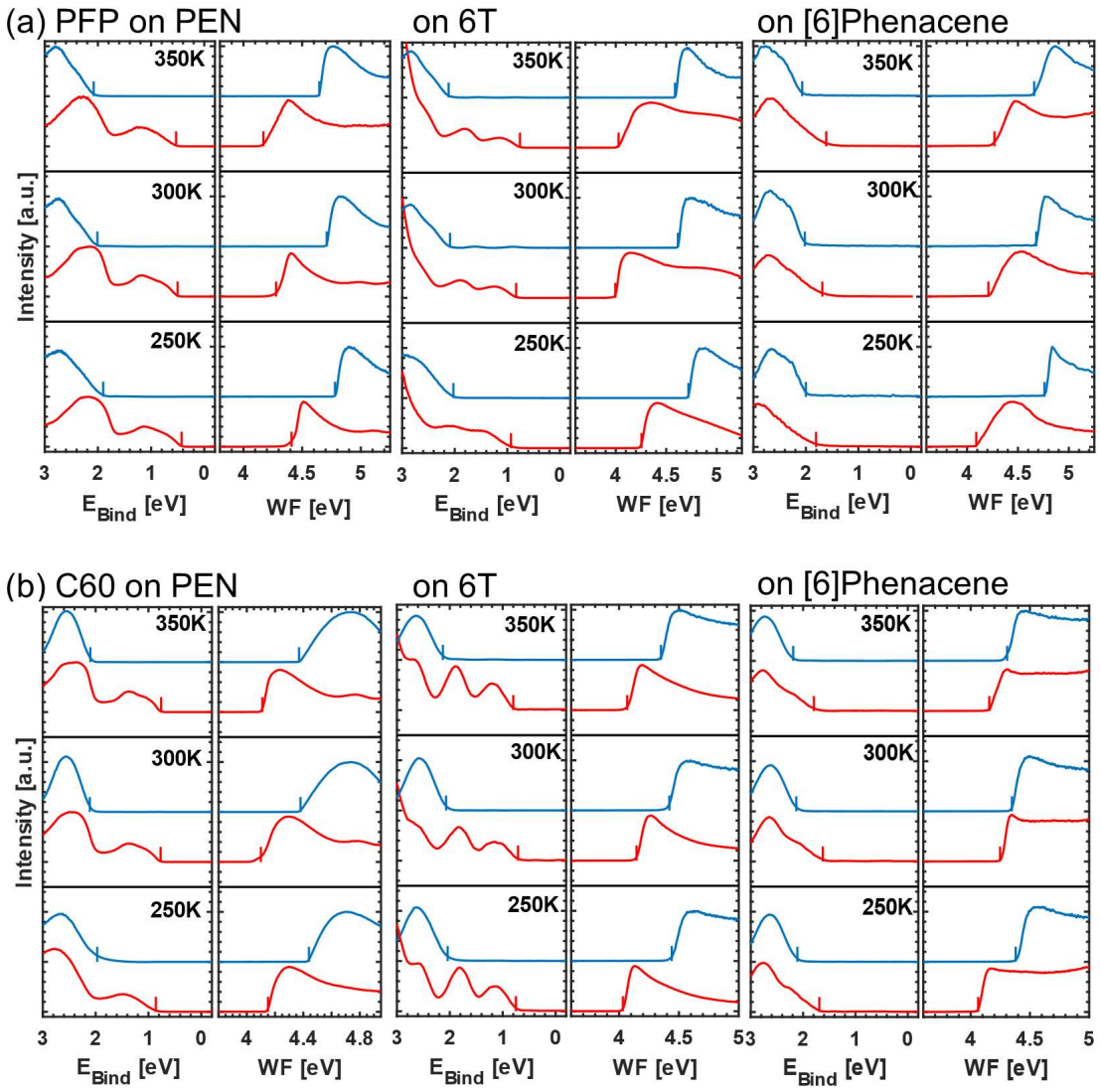

Figure 5.29: UPS data of the investigated heterostructures. (a) PFP on PEN, on 6T and on [6]Phenacene grown at different substrate temperatures. On the left side, the HOMO regions are plotted, on the right-hand side the corresponding secondary electron cut-offs. The vertical lines indicate the respective onsets from where the binding energy (E_{Bind}) and WF is determined. The IE of PFP stays constant in all heterostructures (6.72 eV) with only a small variation of ± 0.03 eV. (b) C60 on PEN, on 6T and [6]Phenacene grown at different substrate temperatures. Also, the IE of C60 stays constant with a value of 6.46 ± 0.05 eV.

The entire electronic situation for PFP grown on PEN is exemplarily depicted in Fig. 5.30. Independent of the growth temperature, a small ID between PEN and the substrate is observed. The top PFP layer, however, shows a positive ID in all three heterostructures and therefore for all substrate temperatures. The binding energy of PFP is shifted towards larger values, indicating, in fact, Fermi level pinning and transferred charges into the empty LUMO states. Compared to the situation in Sec. 5.1, where PFP was grown directly on SiO_2 the immediate correlation between lower substrate temperature and higher value of the ID is not obtained.

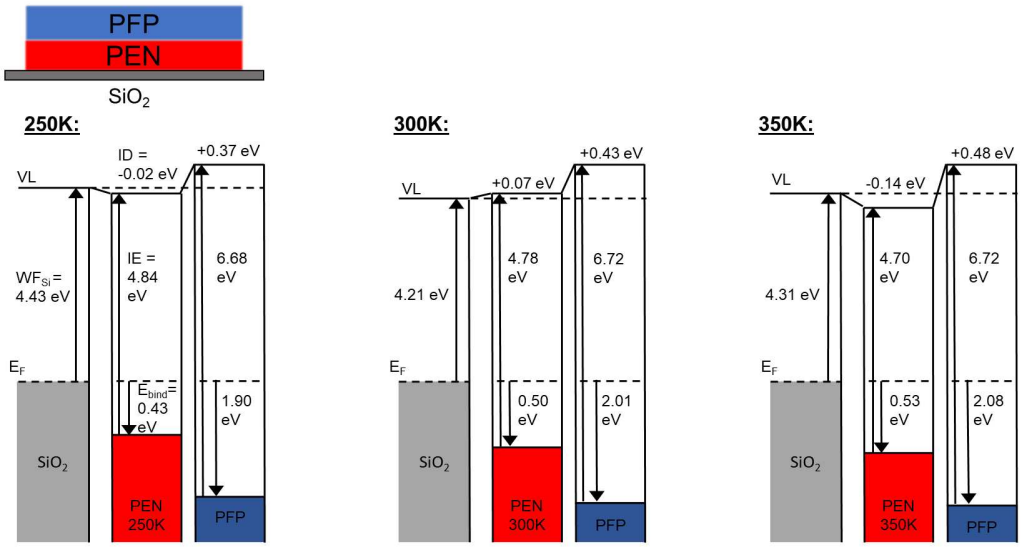

Figure 5.30: Schematic representation of the ELA in a PFP-on-PEN heterostrucutre. The bottom PEN layer exhibits a temperature independent ID ranging from -20 meV to -140 meV for the 250 K and 350 K sample, respectively. PFP, on the other hand, shows a positive ID in all three heterostructures and for all temperatures.

For C60 grown on [6]Phenacene, the situation is similar as depicted in Fig. 5.31. Also here, a small and temperature independent ID is observed between substrate and the bottom layer and a significant positive ID between bottom layer and top C60 layer. The absolute value is somewhat smaller compared to the ID observed for PFP. Which can be reasoned with the smaller EA of C60 and the resulting, slightly smaller overlap between E_F and the LUMO distribution and less transferred charges compared to PFP. Also for C60, the temperature dependence of the ID is somewhat indirect compared to the data of C60 directly grown on silicon (Sec. 5.1.). As will be shown in the following section, the reason for this lies in that not only the gap state density has to be taken into account when attempting to predict the resulting ID but also the impact of the bottom layer VL shift.

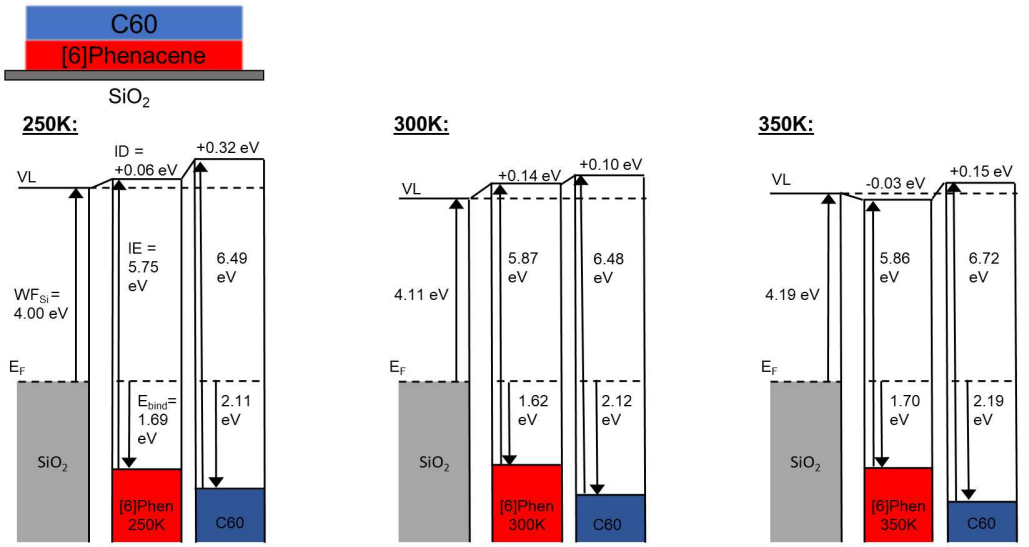

Figure 5.31: ELA of C60 on [6]Phenacene shown schematically in more detail. Just as in the PFP-on-PEN heterostructure, the bottom layer shows a small and temperature independent ID. For the top C60 layer, however, a positive ID is observed for all substrate temperatures. To reliably predict the ID, not only the gap state density has to be taken into account but also the VL shift mediated by the bottom layer.

5.2.1.3 Energy-level alignment of top acceptor layers

To investigate the ELA of the top layer in more detail, the measured IDs between all of the donor/acceptor layers and the binding energies of PFP and C60 are summarised and plotted in Figure 5.32. The colours correspond to the growth temperature of the bottom layer with 250 K (blue), 300 K (brown) and 350 K (yellow). As pointed out before, within the gap state model, the defining property for the magnitude of the ID is the energy distance between the HOMO and LUMO levels relative to the substrate E_F. If E_F comes to lie deep within the fundamental gap of the OSC, no or only a negligible amount of charges are transferred and no systematic, gap state-dependent ID is observed. For example, this is the case for the ELA of the bottom donor molecules discussed before. However, if E_F lies within the HOMO or LUMO distribution of states, charges are transferred from or to the substrate to establish a thermodynamic equilibrium. As discussed by Oehzelt et al. [29], this assumption is not only valid for single-component films but also holds for the case of organic heterostructures. Even if the substrate and the acceptor are separated by a wide gap organic layer, electrons will be transferred and equilibrium across the entire heterostructure is reached.

In the case of the investigated systems involving PFP and C60, the LUMO distribution of states and the substrate Fermi energy are in close proximity and "empty" electronic states are accessible for electrons in the top organic layer. As a result, a positive ID is observed in all heterostructures. To understand how the magnitude of the ID comes about, it is important to realise that it is, in fact, determined by two factors: the bottom layer WF and the gap state density. Assuming a fixed gap state density for two different samples but an increase of the bottom layer's WF would shift the LUMO distribution upwards. There would be less accessible states in the organic layer and, as a result, the observed ID would be smaller. In Fig. 5.32 (a) and (b), this behaviour can be seen in the top rows independent of the different temperatures, with an increase of bottom layer WF leading to a generally smaller ID between PFP/C60 and the donor molecules.

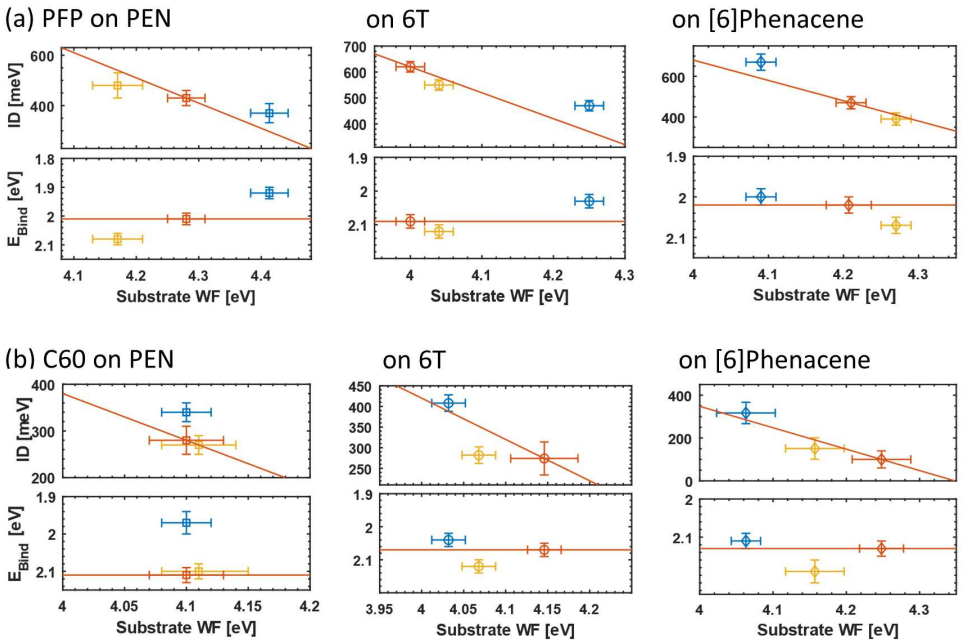

Figure 5.32: ID between the donor and acceptor thin films and E_{Bind} of the respective top layers (PFP (a) and C60 (b)) as a function of bottom layer WF. The colour corresponds to the growth temperature of the bottom layer with 250 K (blue), 300 K (brown) and 350 K (yellow). Two effects determine the magnitude of the ID: the bottom layer WF and the gap state density. As a general trend, a decrease of ID for an increase of WF in all samples, independent of the growth temperature (top rows) is found. Indicated by the brown lines are the expected ID values for a fixed gap state density of the 300 K sample. For the samples grown at a lower temperature, an ID above this line, for the samples grown at higher temperatures the ID is smaller is obtained. This behaviour can be explained with an altered gap state density correlated with the defect densities obtained from the GIXD measurements. A decrease of substrate temperature leads to more defects, more gap states and, in turn, to an increased ID. The bottom rows show the binding energies of the top layers. Also, here, an impact of a changed gap state density is observed, with low temperature samples showing a shift towards smaller binding energies and high temperature samples towards larger energies.

However, also a second effect is at play and correlated to the gap state densities. For a fixed WF, altering the gap state density leads to more or less states being accessible in the organic layer and a higher gap state density would lead to a higher ID. To visualise this effect in the data, the brown lines in the top rows of Fig. 5.32 (a) and (b) indicate the expected ID (for pure Fermi level pinning behaviour) for the sample grown at 300 K over the whole WF range. An ID value above this line corresponds to a higher value than expected and a value below this line to lower ID values than expected compared to the reference sample. As a general trend, the IDs of the low temperature samples (blue) lie above the line and the ones of high temperature samples (yellow) lie below. From previous sections, where the correlation between the in-plane defect density in terms of D_{coh} and the density of gap states was shown, the observed ID behaviour can be related to the crystal quality of the samples. It is found that increasing the substrate temperature during growth of the bottom layer leads to less structural defects, which are, in turn, responsible for less gap states and a smaller ID.

This conclusion is further supported by the analysis of the binding energy of PFP and C60 (Fig. 5.32 (a) and (b), bottom row). For an ELA in the pure Fermi level pinning regime and a fixed LUMO distribution of states, the LUMO level is expected to be shifted to the same energy position, independent of the bottom layer WF and, with that, also the HOMO level is shifted upwards. Since the gap state density is increased for the low temperature sample, the LUMO state distribution is shifted increasingly upwards and the HOMO onset is shifted towards smaller binding energies accordingly. This behaviour is indicated by the brown lines, for a fixed gap state density of the room temperature sample. For the high temperature sample, the situation is reversed. Due to a smaller gap state density, less charges are transferred, and the HOMO onset is located at a higher E_{Bind}.

For a better comparison, Figure 5.33 shows the ID and E_{Bind} data points summarised in one plot. Indicated by the coloured lines are the different temperature regimes of ID and E_{Bind} for the low, room and high temperature samples, calculated from the average value. The averaged ID values for PFP increase by 40 meV between high temperature and medium temperature and 80 meV from medium to high temperature. For C60 the difference is a bit smaller, and the values increase by 40 and 35 meV, respectively. This result shows that the impact of an altered gap state density is generally rather small and is often overlooked in experiments.

Interestingly, the distance of the bottom layer's HOMO level to the top layer's LUMO level has in fact only a small impact on the ID. One could argue that the closer they are in energy, the easier and more efficiently charges could be transferred. However, the values for the respective temperature sample are all in the same range, regardless of the energy level positions of the bottom layer. The difference is especially apparent when comparing the ELA of PFP-on-PEN and PFP-on-[6]Phenacene. The binding energy of

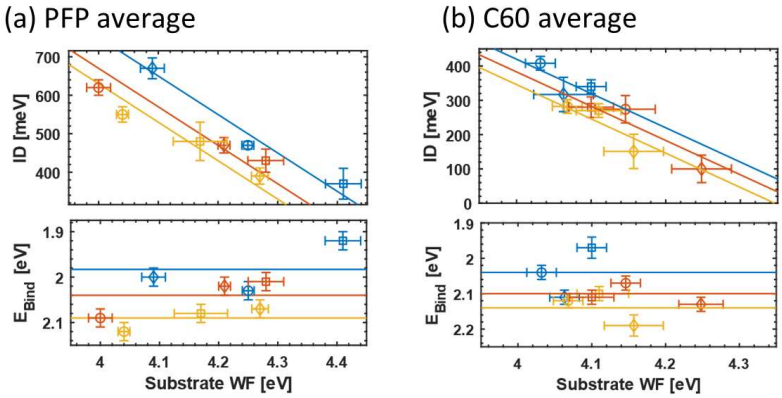

Figure 5.33: Data points from Fig. 5 summarized in one plot. (a) Shows the ID and E_{Bind} of PFP. Indicated by the coloured lines are the expected trends of ID and E_{Bind} calculated from the respective average value. The difference between high temperature samples and medium temperature is +80 meV, between medium temperature and low temperature +80 meV. The difference for C60 (b) is even smaller, with the values increasing by 40 and 35 meV, respectively.

[6]Phenacene is roughly 1.5 eV larger compared to PEN (see Fig. 5.29) and rather close to the HOMO onset of PFP. Nevertheless, the observed IDs only differ slightly indicating that a comparable number of electrons were transferred and highlighting the validity of the model introduced by Oehzelt et al. [46], where the amount of transferred charges is expected to be basically independent of the bottom layer's HOMO position.

5.2.1.4 Summary and Conclusion

The dependence of the ELA of PFP and C60 acceptor molecules was studied in organic-organic heterostructures. PFP and C60 thin films were grown on top of thin film of the donor molecules PEN, 6T and [6]Phenacene grown at different substrate temperatures. The temperature variation only has a small impact on the crystal structure but influences the crystal quality in terms of the coherently scattering island size, D_{coh}, not only for the bottom but also the top layer. As a result, an increased gap state density is for the low temperature samples can be assumed.

The ELA between the SiO_2 substrate and the donor layers only show small and temperature-independent IDs. The top layer ELA, however, is found to be defined by two parameters. For one, the overall variation of the bottom WF. The higher the WF, the smaller the overlap between the substrate E_F and the respective LUMO distribution of states independent of any altered gap state density. However, ultimately, the gap state density is responsible for the exact value of the observed ID, although the impact is found to be rather small and in the range of only 40 to 80 meV for PFP and 40 and 35 meV in the case of C60.

From the present study, it can be concluded that a key factor affecting the ELA at organic-organic interfaces is the electron transfer from or to the organic layers, for which the electronic and structural properties of the bottom layer play a crucial role.

5.2.2 PFP as bottom layer

In the second part of this section, PFP serves as the bottom layer in organic-organic heterostructures and thin film of the donor molecules PEN and [6]Phenacene as well as the other acceptor, C60, are grown on top. This has interesting consequences compared to the situation in the preceding part. There, the ELA of PFP was ultimately defined by the bottom layer WF and the gap state density, since both parameters determine the amount of transferred charges to PFP's LUMO levels. Now, PFP should show a Fermi level pinning behaviour directly on the silicon substrate (see Sec. 5.1), thereby shifting the HOMO and LUMO distributions of the top layers closer or further away to the substrate Fermi energy. In the following, the impact of this shift on the ELA of the top layers is briefly studied.

5.2.2.1 Structural characterization

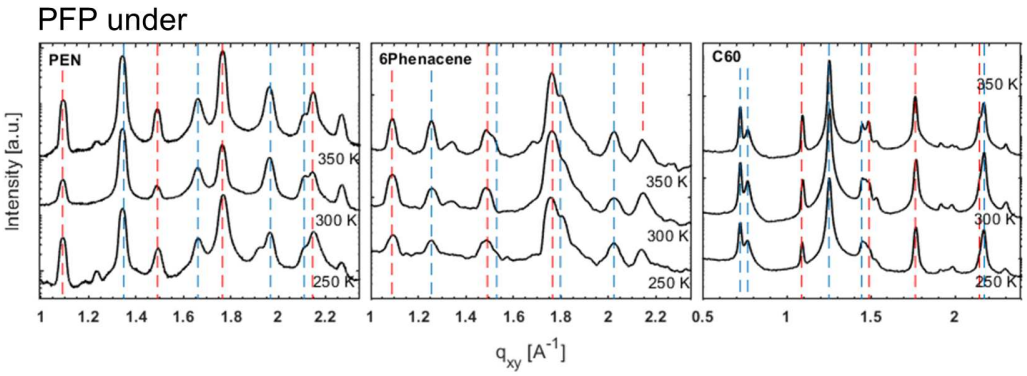

Figure 5.34: GIXD of heterostructures with PFP as the bottom layer in the heterostructure and PEN, [6]Phenacene and C60 as the top layer. The molecular arrangement in the respective layers is similar to the one described above. PFP, PEN and [6]Phenacene molecules adopt a standing up orientation, while C60 shows Bragg reflections from an orientation of fcc-(111) crystal planes parallel to the substrate surface.

Just as before, the substrate temperature during growth of the bottom layer was varied to control the density of structural defects and, accordingly, the gap state density. Figure 5.34 shows the GIXD data of the reversed heterostructures. If grown directly on SiO_2, PFP shows the Bragg reflections associated with the molecules standing and the two shorter unit cell axes oriented parallel to the substrate plane. PEN, [6]Phenacene and C60 adopt the molecular arrangement described before and the same Bragg reflections as in Fig. 5.26 are observed.

5.2.2.2 Electronic properties and ELA

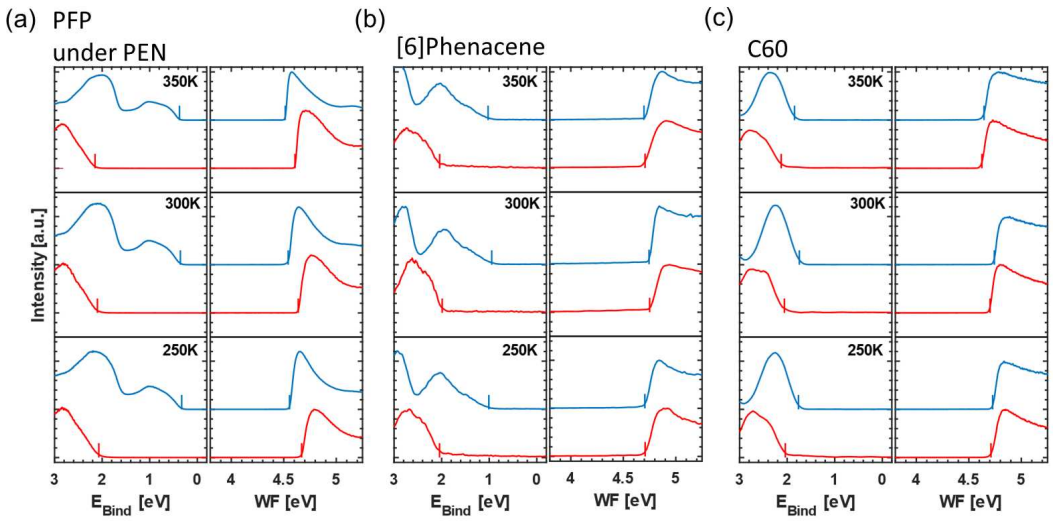

Figure 5.35: UPS data of the heterostructures with PFP as the bottom layer and (a) PEN, (b) [6]Phenacene and (c) C60 as top layers. Also in this case, the altered substrate temperature during growth has only a minor impact on the HOMO shape of the compounds. Compared to the deposition directly on SiO_2, PEN shows a small negative ID of ~ 100 meV for all temperatures. This can be explained with the HOMO distribution of states of PEN being shifted upwards due to the ID of the bottom PFP layer. In this case, HOMO gap states are located above the substrate Fermi energy and electrons are transferred from the organic layer to the substrate. [6]Phenacene, on the other hand, has such a large energy gap that the shift mediated by the PFP is not enough to bring the HOMO distribution in close enough proximity to E_F for charges being transferred and close to no ID is observed. In the case of C60, the VL shift of PFP leads to the C60 LUMO distribution shifted upwards and basically no or only a very small amount of LUMO gap states are accessible. As a result, only a small positive ID is observed between PFP and C60.

As shown in Fig. 5.35 and as expected, also when directly grown on SiO_2 PFP shows a pure Fermi level pinning behaviour with an ID in the range as described before, which is due to an overlap of the LUMO state distribution and the substrate Fermi energy. For PEN as the top layer, a small negative ID between the two organic layers of $\sim$ 100 meV for all three temperatures is found. Compared to the situation where PEN was grown directly on the substrate, due to the ID of the PFP bottom layer, the HOMO distribution is now shifted upwards and electrons are able to transfer from the PEN layer to the substrate as a result of HOMO gap states above E_F. For [6]Phenacene as the top layer, on the other hand, due to the large energy gap of [6]Phenacene the shift is not large enough to bring the HOMO level into close enough proximity to E_F and no or only a very small ID is observed (< 20 meV). Interestingly, for C60 as the top layer, the ID of PFP leads to the C60 LUMO distribution shifted upwards and no or only a small

amount of LUMO gap states are accessible. As a result, only a small and positive ID is observed between PFP and C60.

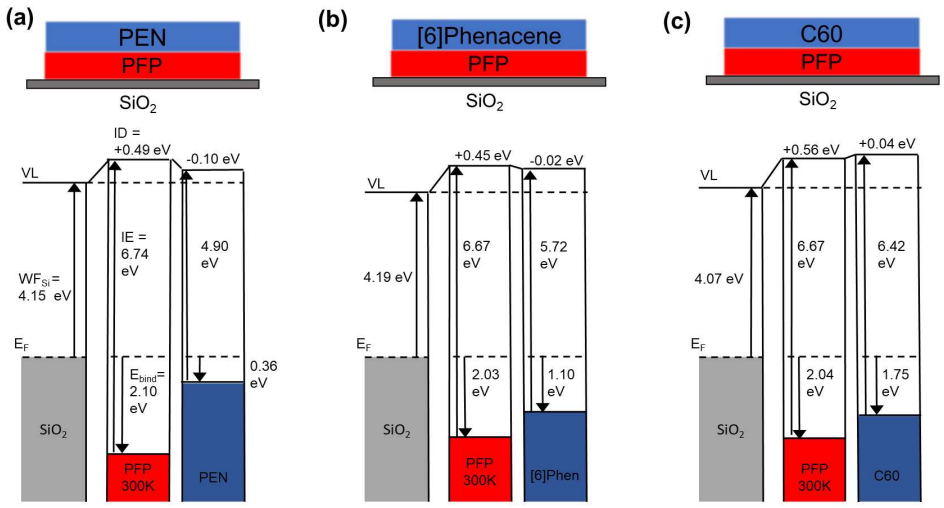

Figure 5.36: Schematic representation of the ELA between the room temperature samples of PFP and (a) PEN, (b) [6]Phenacene and (c) C60. For PEN and C60 the situation is different compared to the growth directly on the silicon substrate. PEN now exhibits a small negative ID, due to the HOMO distribution of states being shifted upwards and in close proximity to the substrate Fermi energy, as a result of the bottom PFP layer VL shift. Compared to the situation described in the section before, the ID between C60 and the bottom layer is now rather small and a ID of only 40 meV is observed. Again, the reason is the HOMO and LUMO distributions being shifted upwards by the ELA the bottom PFP layer. Only for [6]Phenacene no distinct difference was found. In this case, the energy gap between HOMO and LUMO is too large to be affected by an upwards shift and vacuum level alignemtn prevails.

In Fig. 5.36, the situation for the respective room temperature samples is depicted. For (a), PEN grown of PFP, the binding energy is located only 360 meV away from the substrate Fermi energy, which is generally in close enough proximity for gap states to be accessible and one expects charges to be transferred from the HOMO to the substrate. As a result a negative ID between PEN and PFP is observed. In (b), the [6]Phenacene binding energy shows a significantly larger distance and also the LUMO distribution of states is sufficiently far away (since the fundamental gap of [6]Phenacene is ~ 2.7 eV). In this case vacuum level alignment prevails. For C60 on PFP (c), as a result of the VL shift of the bottom layer, the C60 LUMO as well as the HOMO distributions are also too far away from the substrate Fermi energy to allow for any efficient charge transfer. This result is particularly interesting since when grown directly on $SiO2_2$, C60 showed a the same Fermi level pinning behaviour as PFP.

5.2.2.3 Summary and conclusion

To further investigate the impact and influence of a bottom layer on the ELA in between organic layers, heterostructures with PFP as the bottom layer were grown. Structurally, the situation did not change significantly compared to the reversed order of deposition. However, the VL shift of the PFP did lead to change in ELA for PEN and C60. For the former a small negative ID, for the latter only a small positive ID was observed. This can be explained with the responsible HOMO and LUMO distributions being shifted upwards according to the PFP ID. The ELA from [6]Phenacene was not affected by the bottom layer as a result of the rather large band gap of [6]Phenacene and the shift being too small to lead to any overlap between substrate Fermi energy and HOMO distribution.

5.3 Thickness-dependent energy-level alignment in [6]Phenacene/PFP heterostructures

In this section, the thickness-dependent impact of different substrate temperatures on the structural and electronic properties of a planar [6]Phenacene/perfluoropentacene ([6]Phen/PFP) heterostructure on silicon oxide (SiO_2), investigated by in-situ X-ray reflectivity (XRR) and grazing incidence X-ray diffraction (GIXD) as well as ultralow background, high-sensitivity UPS is presented. Both materials were grown to a thickness of 18 nm. The results presented here are part of [**hagenlocher2021thickness**].

5.3.1 Structural characterization

First, the structure of the different heterostructures are discussed, since this information is vital for the evaluation of the electronic properties in the next section. Figure 5.37(a) shows the real-time XRR data of the heterostructures where the bottom [6]Phenacene (thickness 0 to 18 nm) layer was grown at a substrate temperature of T = (i) 250, (ii) 300 and (iii) 350 K. After the growth of [6]Phenacene was finished the system was given time to equilibrate to room temperature before the growth of the top PFP layer (thickness 18 to 36 nm) was started, so that all PFP films were deposited at the same substrate temperature on the [6]Phenacene layer.

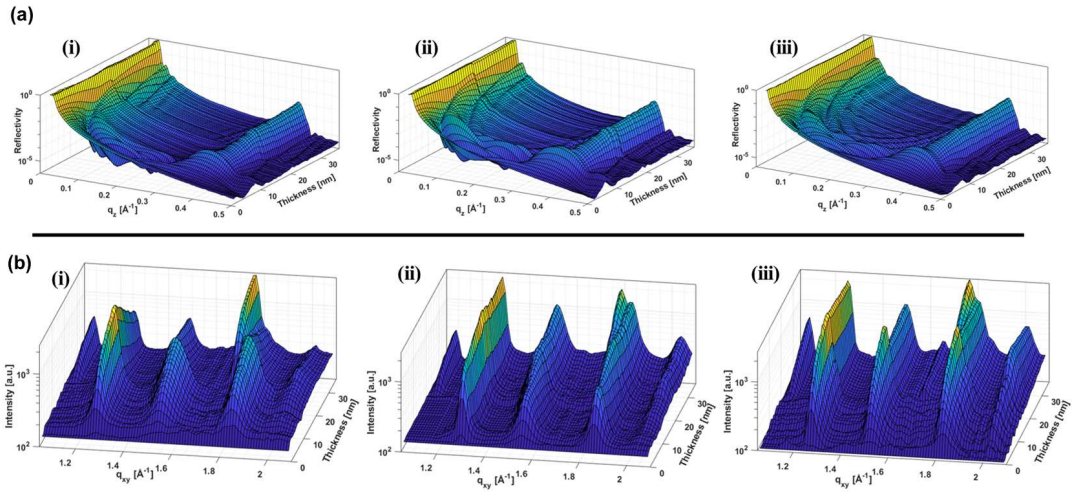

Figure 5.37: In-situ measurements of the PFP-on-[6]Phenacene heterostructures grown at different temperatures. (a) shows the XRR data of (i) [6]Phenacene grown at 250 K substrate temperature, (ii) at 300 K and (iii) at 350 K. (b) the corresponding GIXD data of the same heterostructures.

Evident from the more pronounced Kiessig oscillations (q_z ∼0.05 – 0.15 Å^{-1}) in (ii) and (iii), increasing the substrate temperature leads to overall smoother [6]Phenacene films.

Interestingly, with deposition of PFP on top of the low temperature sample Kiessig oscillations appear, meaning the overall roughness is decreasing and, after 18 nm, does not differ compared to the higher temperatures. This behaviour can be explained with PFP molecules diffusing down the [6]Phenacene terraces where they accumulate and fill the space between grains [219].
Another feature are Laue fringes originating from the coherently scattering crystal size along the z-direction surrounding the Bragg reflection. Their appearance correlates with the length scale of crystalline coherence and indicates larger coherently scattering domains for higher temperatures.

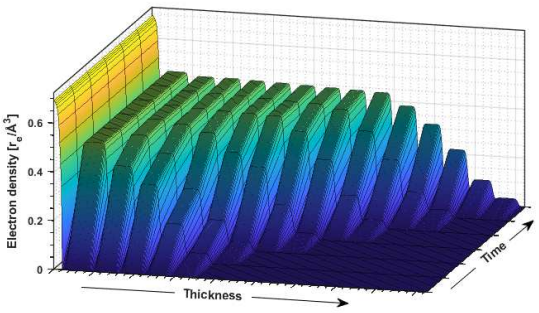

Figure 5.38: Thickness-dependent electron density profile of the [6]Phenacene thin film grown at 300 K. To further investigate the behaviour of the [6]Phenacene molecules especially within the first formed layers, the XRR data was fitted and the respective electron density profile extracted. The lattice spacing of the two first layers is significantly larger than for the subsequent layers, for which the spacing stays constant. This corresponds well to the observed thickness-dependent shift of the Bragg peak position. The respective fits to the XRR data as well as the individual electron density profile can be found in Fig. 5.39

Analysing the Bragg peak position for the different thicknesses, a shift towards higher q_z-values with higher film thickness for the bottom [6]Phenacene layer is found. Converted into a real-space value, this is equivalent to the lattice spacing decreasing, meaning the molecular tilt angle relative to the substrate is changing. This appears to be a generally thickness-dependent effect which was further investigated by a electron density fit for the sample grown at room temperature (Figure 5.38 and Figure 5.39 for the individual fits). The lattice spacing of the two first layers is found to be significantly larger (18.7 Å and 16.7 Å) than for the subsequent layers, for which the spacing stays constant. The same behaviour is found also for the samples grown at higher and lower temperature, however, the final out-of-plane lattice spacing is different (see Table 5.2). Since PFP also grows in a standing up configuration and due to its almost identical long axis length compared to [6]Phenacene molecules, the observed Bragg peak does not visibly deviate with the start of PFP deposition, but rather stays at a constant q_z position corresponding to a lattice spacing of ∼15.8Å and implying that the top layer PFP out-of-plane structure is not thickness dependent.

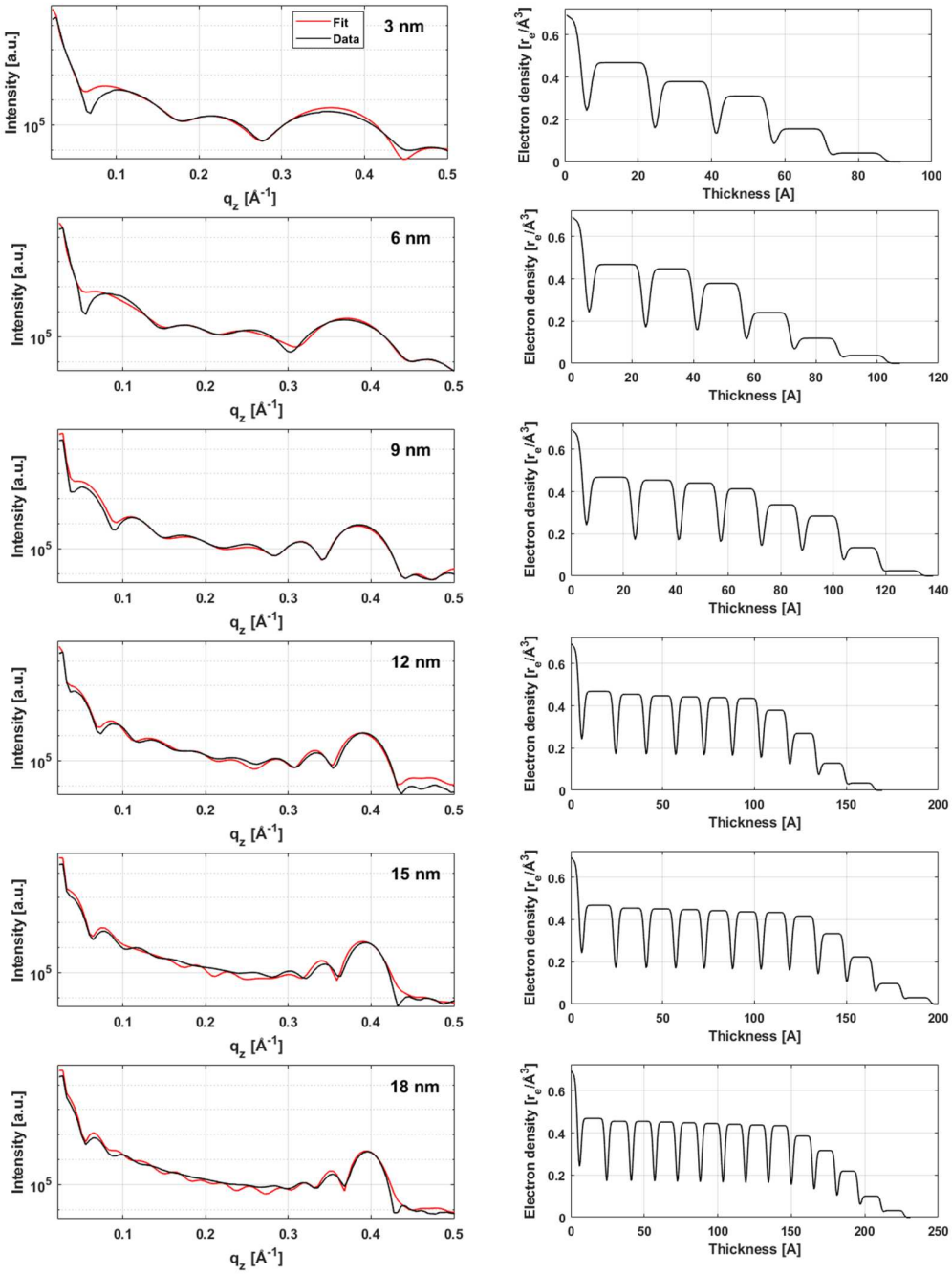

Figure 5.39: On the left hand side, the respective XRR data and the obtained fits for thicknesses up to 18 nm. The right side shows the extracted electron density profiles, from which the 3D plot in Fig. 5.38 was constructed. The two bottom layers are significantly larger than subsequent layers.

Table 5.2: Unit cell parameters and unit cell volume V_{UC} of the 18 nm [6]Phenacene and PFP films, respectively.

	[6]Phenacene				PFP
	a [Å]	b [Å]	c [Å]	V_{UC} [Å^3]	V_{UC} [Å^3]
250K	8.2(3)	6.2(2)	32.0(0)	1638.0(1)	839.0(2)
300K	8.3(8)	6.2(1)	31.6(8)	1648.6(2)	835.9(4)
350K	8.3(9)	6.2(4)	31.4(8)	1648.0(1)	834.2(5)

Figure 5.37 (b) shows GIXD data of [6]Phenacene/PFP heterostructures. All three heterostructures exhibit several in-plane Bragg reflections corresponding to nearly standing molecules and the short axis (ab-plane) of the unit cell parallel to the substrate plane. For [6]Phenacene, the Bragg reflection positions after deposition of 18 nm are moderately temperature dependent, leading to the unit cell parameters summarized in Table 5.2 and showing good agreement with a recently published crystal structure [197]. Figure 5.40 (a) (bottom) shows the thickness dependence of V_{UC} taking also the out-of-plane data into account. An overall decrease of V_{UC} between 6 and 12 nm and a weak decrease between 12 and 18 nm is found. V_{UC}, shown in Table 5.2, differs only slightly between the different substrate temperatures for the films at the final thickness of 18 nm.
From the peak width of the in-plane reflections, the in-plane coherently scattering island size (D_{coh}) of the three films is estimated. For $T = 350$ K, D_{coh} is increasing from 91.2 to 124.5 Å between 3 and 18 nm. The 300 and 250 K samples show only a negligible thickness dependence but depend on the temperature with D_{coh} being 96.5 Å (300 K) and 75.9 Å (250 K) (Figure 5.40 (b), bottom).

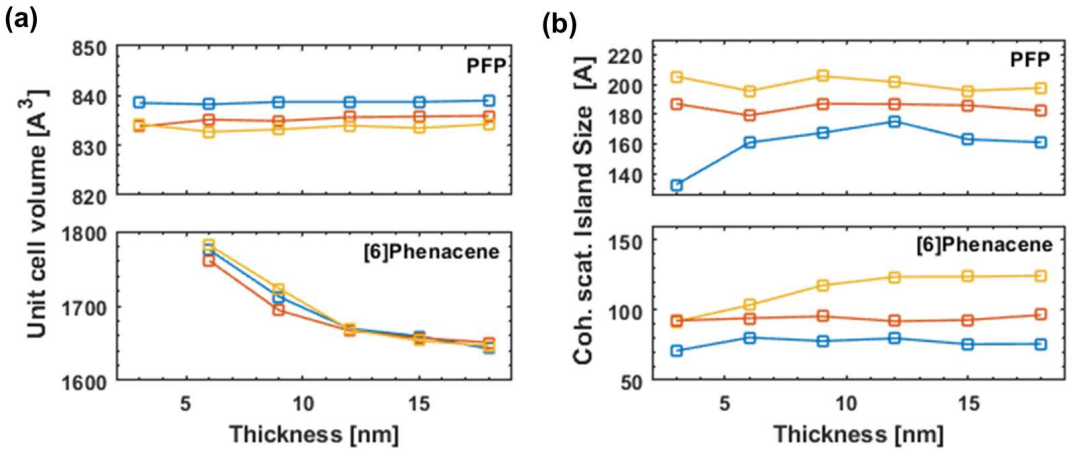

Figure 5.40: Thickness-dependent unit cell volume (V_{UC}) (a) and coherently scattering island size D_{coh} (b). V_{UC} of [6]Phenacene is changing with increasing thickness. This can related to a change in the tilt angle of molecules relative to the substrate. The V_{UC} of PFP stays constant for the entire thickness. D_{coh} is generally temperature dependent, with an increased size for elevated temperatures. Through a templating effect, this can also be found in the PFP layers grown on top.

Since D_{coh} depends on defects and strain which reduce the long-range crystalline order in the thin films, increasing the temperature leads to higher crystallinity. Interestingly, also PFP exhibits an increased crystallinity when the [6]Phenacene layer beneath was grown at high temperature, an templating effect also found in PFP grown on diindenoperylene layer [48]. D_{coh} for PFP is found to be 160.9, 182.3 and 197.5 Å for the 250, 300 and 350 K sample, respectively (Figure 5.40 (b), top). The Bragg reflection position is not affected by the bottom layer and thickness, as evident from Figure 5.40 (a), top), where the unit cell volume is given as a function of thickness (see also Table 5.2).

5.3.2 Thickness-dependent electronic structure

5.3.2.1 [6]Phenacene

In order to obtain a thorough understanding of the electronic properties of the entire heterostructure, the ELA of [6]Phenacene on the SiO_2 substrate is discussed next. Figure 5.41 shows the UPS data for the different substrate temperatures during growth dependent on film thickness.

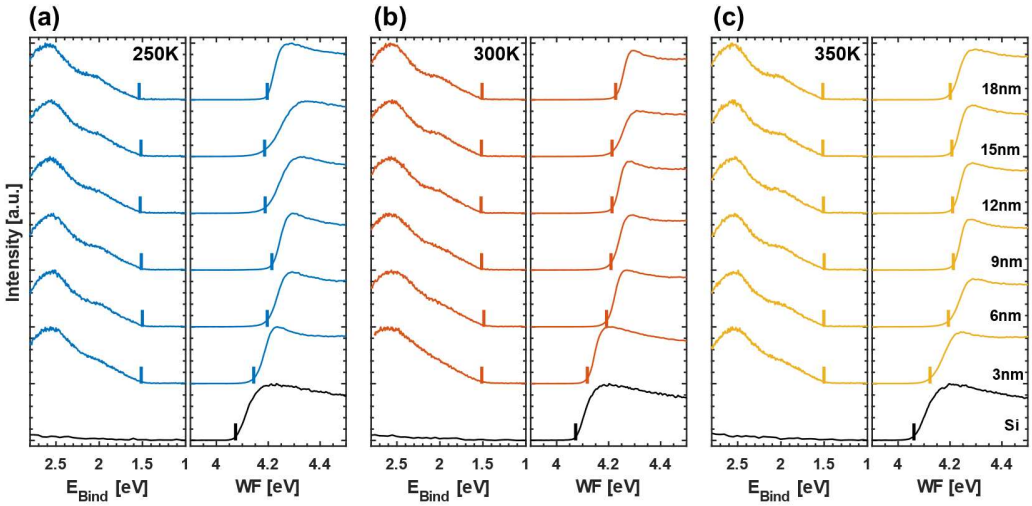

Figure 5.41: HOMO region (left) and SECO (right) of [6]Phenacene on SiO_2 for different substrate temperatures during growth: (a) 250 K (blue), (b) 300 K (brown) and (c) 350 K (yellow). For the actual UPS measurements, the samples were allowed to equilibrate to room temperature (∼300 K) and cooled or heated again afterwards.

On the respective left-hand side, the HOMO region is plotted, on the right-hand sight the corresponding secondary electron cut-off (SECO). Interestingly, the overall HOMO shape and the binding energy E_{Bind} (as determined from the HOMO onset and indicated by short vertical lines) is affected neither by the substrate temperature nor by the film thickness, with an average value of 1.51 ± 0.02 eV (see Figure 5.42, bottom).

However, the ionization energy (IE) of [6]Phenacene appears to be thickness dependent. The IE is determined by adding the respective binding energy to the WF, measured from the SECO onset (also indicated by short vertical lines and plotted in Figure **??**, top). As can be seen from Figure 5.42, the value of the IE is mainly governed by the thickness dependence of the WF. It was shown that the precise molecular orientation in ordered molecular assemblies can have a strong impact on the electrostatic surface potential and is influencing the WF and therefore the IE.[208, 220, 221] In the present case the thickness dependence of the IE can be assigned to the structural change [6]Phenacene is undergoing with increasing film thickness (see Figure 5.40 (d)). This argument is further

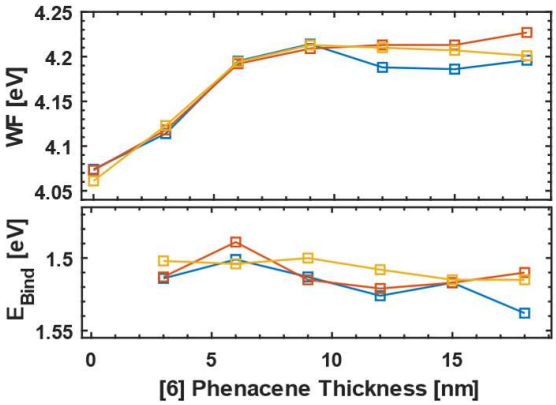

Figure 5.42: Change of work function (WF) and binding energy (E_{Bind}) as a function of [6]Phenacene thickness.

strengthened when comparing the respective trends for unit cell volume and WF. In both cases the change is most significant for film thicknesses between 3 and 9 nm and comparatively constant for film thicknesses above. The change of IE ranges from 106 meV for the low and room temperature sample to 91 meV for the high temperature sample respectively. Since the substrate Fermi energy (E_F) lies approximately in the middle of the energy gap given by the [6]Phenacene HOMO onset ($E_{Bind} \approx 1.5$ eV below E_F) and the estimated LUMO onset position ($\sim$1.6 eV above E_F, obtained by adding the optical band gap of [6]Phenacene ($\sim$3.1 eV) to E_F), any effects of gap states on the ELA at the [6]Phenacene/SiO_2 interface are unlikely and vacuum level alignment is expected. Since the gap states density is known to reach only a few hundred meV into the gap, there is a too large energy difference to allow for efficient electron transfer between substrate and organic material [52, 53].

5.3.2.2 PFP on [6]Phenacene

Figure 5.43 shows the thickness dependent UPS data of PFP grown on top of different [6]Phenacene bottom layers. On the left-hand side, the PFP HOMO regions are shown. The background signal from [6]Phenacene was subtracted for the 3 and 6 nm measurements. The right-hand side shows the WFs obtained from the SECO onset, up to a PFP thickness of 18 nm.

First, a temperature dependent initial interface dipole (ID, i.e. difference between WF values) between [6]Phenacene and the first 3 nm thick layer of PFP, with values of +100 meV for the low temperature and +30 meV for the higher temperatures is noted. The PFP shows a thickness dependent shift of the WF (Figure 3(b), top). However, in comparison to [6]Phenacene the trend appears to be more linear with a comparably

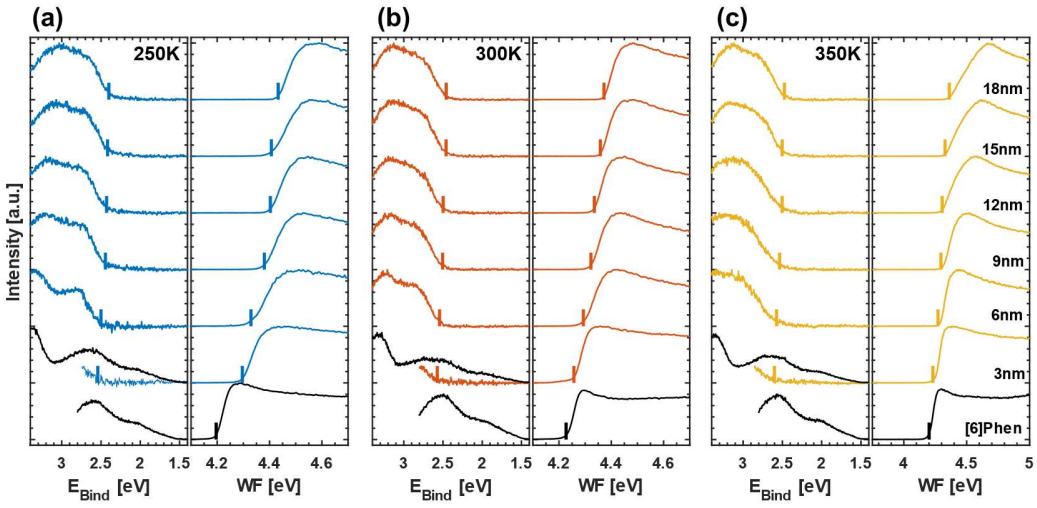

Figure 5.43: HOMO region (left) and SECO (right) of PFP on [6]Phenacene grown at different substrate temperatures: (a) 250 K, (b) 300 K and (c) 350 K. The [6]Phenacene background was fitted and subtracted for the 3 and 6 nm measurements.

constant interface dipole when adding an additional material. Furthermore, the observed ID shows a temperature dependence with the total ID between 3 and 18 nm being 137 meV for PFP grown on the low temperature [6]Phenacene and 115 meV and 110 meV for the 300 and 350 K samples respectively. Examining E_{Bind} more closely, it is found that, contrary to [6]Phenacene, the binding energy does not stay constant, but is decreasing with increasing thickness (Figure 5.44, bottom).

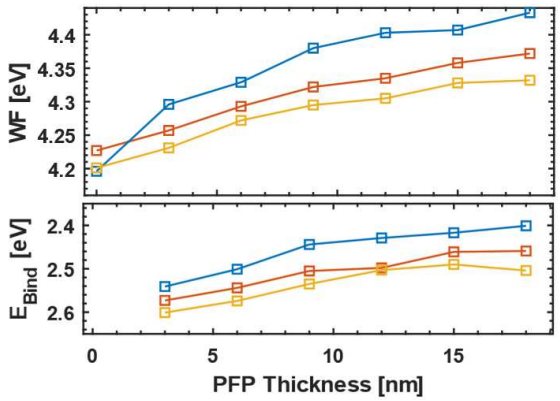

Figure 5.44: Change of work functin (WF) and binding energy (E_{Bind}) as a function of PFP thickness.

In addition, this behaviour is also temperature dependent with E_{Bind} changing from 2.54 eV to 2.40 eV (Δ = 140 meV) for low temperature, from 2.57 eV to 2.46 eV (Δ = 110 meV) for room temperature and from 2.60 eV to 2.50 eV (Δ = 100 meV) for the

high temperature sample. Calculating the IE for PFP a rigid shift for E_{Bind} and WF is obtained and consequentially, the IE stays constant at an average value of 6.83 ± 0.03 eV for all thicknesses and temperatures. This result is further confirmed by the X-ray data, where a thickness independent V_{UC} for PFP was found and therefore the IE is not expected to change.
The ELA of PFP on [6]Phenacene can be rationalized considering structural parameters. As can be seen in Figure 5.40 (b), top), D_{coh} of PFP shows a template effect when grown on top of [6]Phenacene, with a higher crystal quality for elevated substrate temperatures. As was previously shown, an increase in the density of structural disorder is directly correlated with an increase in the gap state density.
So far, due to experimental restrictions, only a direct measurement of HOMO gap states is possible. The direct detection of gap states reaching out from the LUMO level, which is principally accessible with inverse photoelectron spectroscopy (IPES), is still elusive. However, the impact of an altered LUMO gap state density on the ELA can be studied using a conventional UPS set-up. This is apparent when adding PFP's band gap of 2.5 eV to the observed E_{Bind} [205]. One finds that the E_F of the substrate lies well within the PFP LUMO distribution, with therefore accessible "empty" electronic states. To establish the thermodynamic equilibrium, electrons are transferred from the SiO_2 into those states in the PFP layer and change the measured WF accordingly. The amount of transferred charges and the absolute value of the ID is now directly dependent on the number of accessible states beneath the substrate E_F (i.e. the density of gap states) which, in turn, can be controlled by changing the crystallinity of the sample [29, 222]. Applying this model to the data presented here, a qualitative agreement between the density of defects and the observed ID is found.

5.3.3 Summary and conclusion

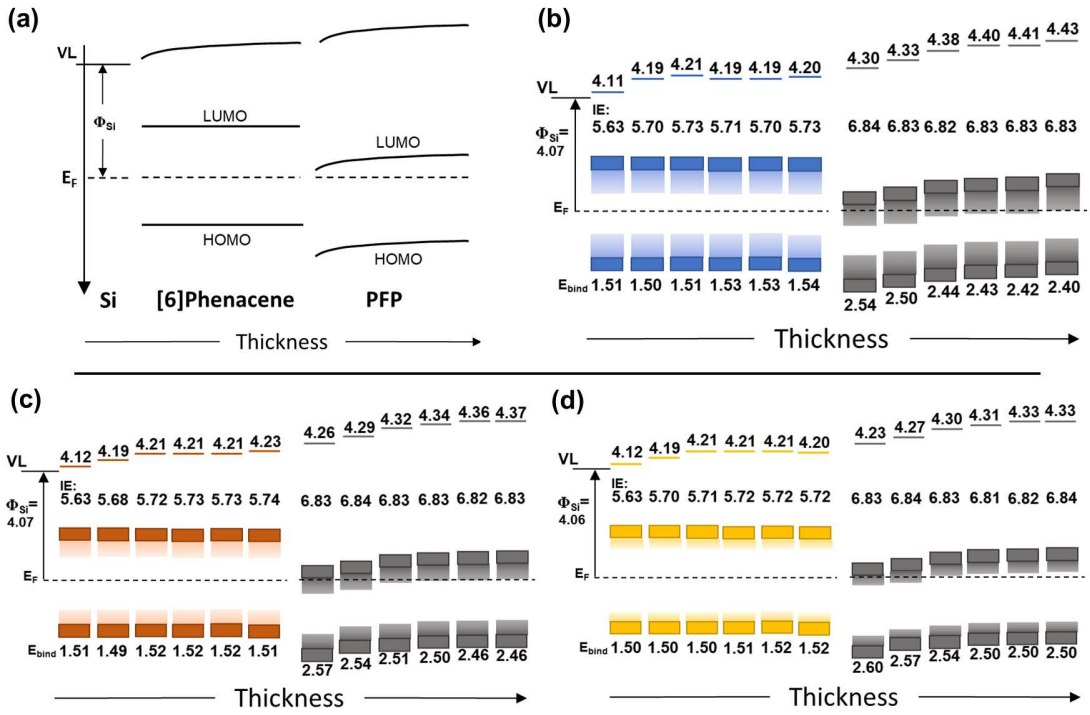

Figure 5.45: (a) Schematic representation of the energy level alignment. (b)-(d) ELA of the three heterostructures with the bottom [6]Phenacene layer grown at different substrate temperatures: 250 K (blue), 300 K (brown) and 350 K (yellow). The shading above the HOMO and below the LUMO levels represents the respective gap state density.

A detailed investigation of the thickness- and temperature-dependent structural and electronic properties of a [6]Phenacene/PFP heterostructure grown on SiO_2, using in-situ X-ray scattering and ultralow background UPS was presented. The molecular arrangement of the bottom [6]Phenacene layer was found to be strongly depending on the film thickness, but only slightly impacted by a different growth temperature, additionally, the crystallinity is enhanced for elevated temperatures. A fact that is adopted by the PFP film grown on top via a templating effect. The unit cell parameters of PFP are not changing with increasing thickness and do not show a dependence on the bottom layer's substrate temperature during growth.
Two key findings arise regarding the electronic properties of the heterostructures, which are summarized in Figure 5.45. The ionization energy of [6]Phenacene is found to be thickness dependent and correlated with the structural rearrangement the molecules undergo with continuing growth, while no HOMO shift is observed [221]. In contrast, the ELA of PFP depends on the density of gap states that can be attributed to structural imperfections apparent from different sizes of coherently scattering domains. An increased

density of gap states due to an increase of structural defects enables a larger number of electrons to transfer from the substrate to unoccupied gap states lying beneath the substrate E_F. Electronically, the bottom [6]Phenacene layer thereby simply acts as charge transport layer, however, due to the structural templating effect is ultimately responsible for the magnitude of the level shift of PFP.
The findings show that the spatial distribution of gap states is a key factor affecting the ELA at organic-organic interfaces as well as interfaces between an inert inorganic and an organic material. Moreover, the thickness dependence of the energy shift indicates that an accurate control of the molecular arrangement in thin organic semiconductor films may represent another key factor for controlling the efficiency and functionality of different organic devices.

6 Conclusion and Outlook

The main topic of this work was to investigate the connection between structural properties on gap states and their impact on the energy-level alignment in single component thin films and organic heterostructures. The results and conclusions are summarized in the following section, which ends with an outlook on possible future projects.

6.1 Results on the origin of gap states

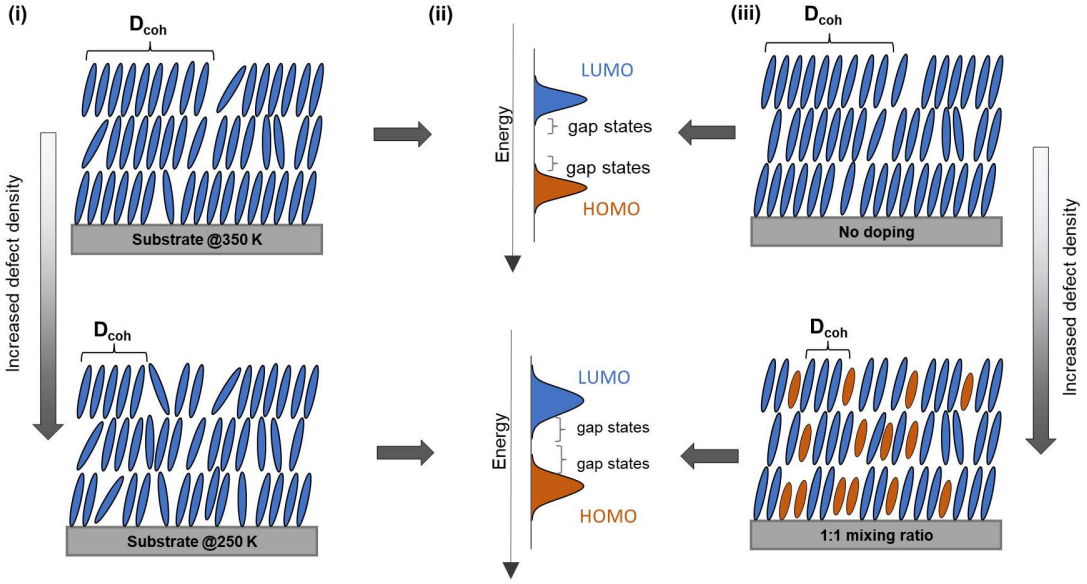

Figure 6.1: The gap state density can be controlled by temperature variation of the substrate during growth or by statistical intermixing of two alike compounds. In both cases, areal in-plane defects, obtained from the coherently scattering island size, can be identified as the main source of gap states.

The density of structural defects was effectively controlled in Sec. 5.1 by choosing different substrate temperatures during growth. In all four materials, a general trend towards an increasing number of defects with a decrease of substrate temperature was found and explained with a hindered mobility of molecules on the substrate surface in combination with an altered inter-layer transport. Upon closer investigation of the different kinds of defects, the dependence on substrate temperature was particularly apparent for large

domain boundaries and for in-plane areal defects. The defects acting in the out-of-plane direction were not as strongly affected.
The ionization energies of the materials only exhibited a minor variation for different substrate temperatures. This is in good agreement with the well preserved molecular arrangement as observed from GIXD and XRR measurements.

The gap state density, observed as exponential tails reaching into the band gap, scales with the crystal quality and is increased when more defects are present. From a comparison of the dependence of gap states and structural defect density on the growth temperature, the gap states can be successfully linked to the in-plane defect density obtained from the coherently scattering island size (Fig. 6.1). For PFP and C60, a correlation between gap state density and interface dipole is observed (Fermi-level pinning). Since the substrate work function shows only a slight deviation for one set of samples, the number of transferred charges is ultimately defined by the overlap of the LUMO distribution's gap states and the substrates Fermi energy. The higher the gap state density, the more states are accessible and more charges are transferred resulting in a larger interface dipole.

In a second part, the gap state density was varied by structural doping. Intermixing of [5]- and [6]Phenacene leads to the formation of a solid solution with statistical occupation of lattice sites depending on the mixing ratio. The overall morphology and the domain size are strongly affected by mixing and a linear increase of domain boundaries between adjacent domains is observed. While the unit cell arrangement is not affected by mixing, the crystal quality in terms of the in-plane coherent scattering island size varies significantly with a minimum observed for the 1:1 mixing ratio. From a comparison with the two defect parameters, the gap state density of the blends can be correlated with the density of small in-plane areal defects, confirming the results obtained above. For the system, no dependence of the interface dipole on the gap state density is found. Since the energy positions between HOMO and LUMO onset and substrate Fermi energy are sufficiently large for no efficient charge transfer, vacuum level prevails.

6.2 Results on the energy-level alignment in organic heterostructures

In Sec. 5.2, the interplay of structural properties and the ELA was investigated for planar heterostructures consisting of films of different combinations of donor and acceptor molecules. Interestingly, the bottom layer had a strong impact on the crystal quality of the top layer and a correlation of the coherently scattering island size of the two was observed. The interface dipole of the top layer was found to correlate, on the one hand, with the crystallinity of the film and, on the other hand, with the substrate work function of the bottom layer. Since these features ultimately define the overlap of the

HOMO or LUMO distribution with the substrate Fermi energy, both are responsible for the amount of transferred charges and the magnitude of the obtained energy-level shift. No impact of the energy distance between the HOMO of the bottom layer and the LUMO of the top layers on the observed ID was found. This indicated that the charges are in fact transferred from the substrate, through the bottom layer into the top layer.

Reversing the order of deposition and applying a PFP thin film as the bottom layer allowed further insight into the electronic properties of heterostructures. As expected, a Fermi-level pinning between the substrate and the PFP layer accompanied by an interface dipole is observed. However, the materials deposited as the top layer, in parts, show a different ELA compared to the deposition directly on the inorganic substrate. For PEN, a small negative ID is observed, indicating an overlap of HOMO states with the substrate Fermi energy. [6]Phenacene, on the other hand, shows no considerable ID due to its larger band gap and the still to big energy barriers. Using C60 as the top layer, only a small positive interface dipole is observed, which coincides with its LUMO distribution being shifted upwards due to the bottom PFP layer and the gap state overlap is decreased.

These findings highlight the importance of the electronic *and* electronic properties of the bottom layer on the ELA of the top layer, which ultimately defines the functionality and efficiency of devices.

6.3 Results on the thickness-dependent energy-level alignment in heterostructures

A detailed investigation of the thickness- and temperature-dependent structural properties of a [6]Phenacene/PFP heterostructure was presented in Sec. 5.3. The molecular arrangement of the bottom [6]Phenacene layer, grown at different substrate temperatures, was found to strongly depend on the film thickness but only slightly on the substrate temperature. The unit cell parameters were calculated and an electron density fit of the sample grown at room temperature was produced. Apparently, the first three layers show a different lattice spacing compared to the others. Due to the slightly changing direction of the polar C-H bond, the ionization energy of [6]Phenacene is thickness-dependent and increases by $\sim 100\,\mathrm{meV}$ between the first layer up to a thickness of 18 nm, while the HOMO energy stays at a constant binding energy (Fig. 6.2). The unit cell parameters of PFP are not changing with increasing thickness and do not show a dependence on the substrate temperature. However, the before described templating effect in crystal quality is also observed for this heterostructure. As a result, the ELA of PFP depends on the density of gap states that can be attributed to the structural imperfections.

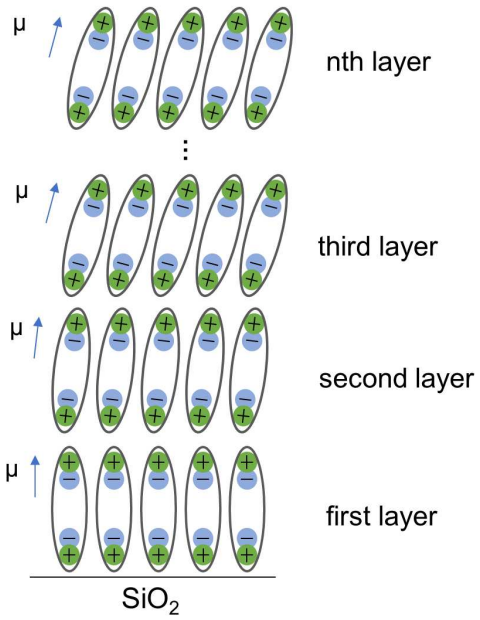

Figure 6.2: Thickness-dependent change of tilt angle of the [6]Phenacene molecules. Since the C-H bond is polar, the direction of the dipole moment is changed and alters the observed WF with increasing thickness.

Electronically, the bottom [6]Phenacene layer is simply acting as a charge transport layer, however, due to the structrual templating effect is ultimately responsible for the magnitude of the level shift of PFP. The findings indicate that an accurate control of the molecular arrangement in OSC thin films are another key factor in device design.

6.4 Outlook

The presented results offered new insights into the interplay of structural and electronic defects. Based on the results, new questions and ideas arise, which are briefly outlined in the following and which could be the topic of follow-up studies.

- For a more thorough understanding of the origin of gap states described in Sec. 5.1, more and different molecules may be included in systematic studies. While no dependence on shape or polarity of the gap state density between the different compounds was found, in a next step disc-like compounds such as phthalocyanins could be incorporated. Also, the slight deviation from ideal exponential tails in the low temperature gap state densities of PEN and [6]Phenacene should be studied in greater detail, since they could point towards the influence of a predominant type of structural defect resulting in a hump-like feature.

- Diffraction and UPS experiments on single crystals of the compounds could be used as a limiting case for a very low defect density and compared to the presented results. Especially, the dependence of the coherently scattering island size on the crystallite sizes and its impact on the gap state density could be studied.

- In order to further study the role of the substrate in the ELA of organic materials, the selection of substrates could be increased. Doing so, the proposed mechanisms could be confirmed for materials with smaller or larger work functions, surface terminations and reactivities.

- The gap states densities investigated in this work were all measured with UPS and therefore HOMO gap states tailing into the gap. Although, the observed level shifts are thought to be a result of an altered gap state density reaching out from the LUMO. In principle, a measurement of LUMO gap states is possible using *inverse photoelectron spectroscopy* (IPES). However, due to experimental restrictions (e.g. sample damage and high signal-to-noise ratio), a direct measurement of LUMO gap states is still elusive. If in some years, the experimental set-ups have reached a high enough quality, the same experimental strategy could be deployed to study the connection between structural defects and the LUMO gap state density.

Acronyms

Materials

[5]Phen	[5]Phenacene
[6]Phen	[6]Phenacene
6T	α-sexithiophene
C60	Buckminsterfullerene
PEN	Pentacene
PFP	Perfluoropentacene
Si	Silicon
SiO_2	Silicon oxide

Experimental techniques

AFM	Atomic force microscopy
FWHM	Full width at half maximum
GIXD	Grazing incidence X-ray diffraction
UHV	Ultra-high vacuum
UPS	Ultraviolet photoelectron spectroscopy
WHA	Williamson-Hall analysis
XRR	X-ray reflectivity

Miscellaneous

D_{coh}	Coherently scattering island size
EA	Electron affinity
E_{Bind}	Binding energy
E_F	Fermi energy
EEL/HEL	Electron/Hole extraction layer
ELA	Energy-level alignment
ETL/HTL	Electron/Hole transport layer

HOMO	Highest occupied molecular orbital
IE	Ionization energy
K	Kelvin
LUMO	Lowest unoccupied molecular orbital
OLED	Organic light emitting diode
OPV	Organic photovoltaic
OSC	Organic semiconductor
SECO	Secondary electron cut-off
VL	Vacuum level
WF	Work function

Bibliography

[1] G. Schweicher, G. Garbay, R. Jouclas, F. Vibert, F. Devaux, and Y. H. Geerts, "Molecular semiconductors for logic operations: Dead-end or bright future?" *Advanced Materials*, vol. 32, no. 10, p. 1 905 909, 2020.

[2] J. Ajayan, D. Nirmal, P. Mohankumar, M. Saravanan, M. Jagadesh, and L. Arivazhagan, "A review of photovoltaic performance of organic/inorganic solar cells for future renewable and sustainable energy technologies," *Superlattices and Microstructures*, p. 106 549, 2020.

[3] J. H. Burroughes, D. D. Bradley, A. Brown, R. Marks, K. Mackay, R. H. Friend, P. L. Burns, and A. B. Holmes, "Light-emitting diodes based on conjugated polymers," *Nature*, vol. 347, no. 6293, pp. 539–541, 1990.

[4] M. A. Baldo, D. F. O'Brien, Y. You, A. Shoustikov, S. Sibley, M. E. Thompson, and S. R. Forrest, "Highly efficient phosphorescent emission from organic electroluminescent devices," *Nature*, vol. 395, no. 6698, pp. 151–154, 1998.

[5] G. Schwartz, K. Fehse, M. Pfeiffer, K. Walzer, and K. Leo, "Highly efficient white organic light emitting diodes comprising an interlayer to separate fluorescent and phosphorescent regions," *Applied Physics Letters*, vol. 89, no. 8, p. 083 509, 2006.

[6] C. D. Dimitrakopoulos and P. R. Malenfant, "Organic thin film transistors for large area electronics," *Advanced Materials*, vol. 14, no. 2, pp. 99–117, 2002.

[7] G. Horowitz, "Organic field-effect transistors," *Advanced Materials*, vol. 10, no. 5, pp. 365–377, 1998.

[8] M. Muccini, "A bright future for organic field-effect transistors," *Nature Materials*, vol. 5, no. 8, pp. 605–613, 2006.

[9] B. Kippelen and J.-L. Brédas, "Organic photovoltaics," *Energy & Environmental Science*, vol. 2, no. 3, pp. 251–261, 2009.

[10] S. B. Darling and F. You, "The case for organic photovoltaics," *Rsc Advances*, vol. 3, no. 39, pp. 17 633–17 648, 2013.

[11] K. Leo, "Organic photovoltaics," *Nature Reviews Materials*, vol. 1, no. 8, pp. 1–2, 2016.

[12] E. Ma, Y. Wang, Q. Lu, M. Sui, L. Lu, and K. Lu, "Strain hardening and large tensile elongation in ultrahigh-strength nano-twinned copper," *Applied Physics Letters*, vol. 85, no. 21, pp. 4932–4934, 2004.

[13] Y. Yang, J. Ouyang, L. Ma, R.-H. Tseng, and C.-W. Chu, "Electrical switching and bistability in organic/polymeric thin films and memory devices," *Advanced Functional Materials*, vol. 16, no. 8, pp. 1001–1014, 2006.

[14] A. Loi, I. Manunza, and A. Bonfiglio, "Flexible, organic, ion-sensitive field-effect transistor," *Applied Physics Letters*, vol. 86, no. 10, p. 103 512, 2005.

[15] V. Savvate'Ev, Z. Chen-Esterlit, J. Aylott, B. Choudhury, C.-H. Kim, L. Zou, J. Friedl, R. Shinar, J. Shinar, and R. Kopelman, "Integrated organic light-emitting device/fluorescence-based chemical sensors," *Applied Physics Letters*, vol. 81, no. 24, pp. 4652–4654, 2002.

[16] M. R. Cavallari, L. M. Pastrana, C. D. F. Sosa, A. M. R. Marquina, J. E. E. Izquierdo, F. J. Fonseca, C. A. d. Amorim, L. G. Paterno, and I. Kymissis, "Organic thin-film transistors as gas sensors: A review," *Materials*, vol. 14, no. 1, p. 3, 2021.

[17] G. P. Neupane, W. Ma, T. Yildirim, Y. Tang, L. Zhang, and Y. Lu, "2d organic semiconductors, the future of green nanotechnology," *Nano Materials Science*, vol. 1, no. 4, pp. 246–259, 2019.

[18] H. Iino and J.-i. Hanna, "Liquid crystalline organic semiconductors for organic transistor applications," *Polymer Journal*, vol. 49, no. 1, pp. 23–30, 2017.

[19] C. Yumusak, N. S. Sariciftci, and M. Irimia-Vladu, "Purity of organic semiconductors as a key factor for the performance of organic electronic devices," *Materials Chemistry Frontiers*, vol. 4, no. 12, pp. 3678–3689, 2020.

[20] H. Bronstein, C. B. Nielsen, B. C. Schroeder, and I. McCulloch, "The role of chemical design in the performance of organic semiconductors," *Nature Reviews Chemistry*, vol. 4, no. 2, pp. 66–77, 2020.

[21] Y. Yang, Z. Liu, G. Zhang, X. Zhang, and D. Zhang, "The effects of side chains on the charge mobilities and functionalities of semiconducting conjugated polymers beyond solubilities," *Advanced Materials*, vol. 31, no. 46, p. 1 903 104, 2019.

[22] J. Yang, Z. Zhao, S. Wang, Y. Guo, and Y. Liu, "Insight into high-performance conjugated polymers for organic field-effect transistors," *Chem*, vol. 4, no. 12, pp. 2748–2785, 2018.

[23] N. Koch, "Organic electronic devices and their functional interfaces," *ChemPhysChem*, vol. 8, no. 10, pp. 1438–1455, 2007.

[24] D. Z. Pudenz. "Red, green and blue oleds with an acative surface area of 2x2 mm." (2011), [Online]. Available: `https://www.ineffableisland.com/2011/12/electronics-made-of-plastic-with.html` (visited on 07/08/2021).

[25] A. Opitz, "Energy level alignment at planar organic heterojunctions: Influence of contact doping and molecular orientation," *Journal of Physics: Condensed Matter*, vol. 29, no. 13, p. 133 001, 2017.

[26] A. Hinderhofer and F. Schreiber, "Organic–organic heterostructures: Concepts and applications," *ChemPhysChem*, vol. 13, no. 3, pp. 628–643, 2012.

[27] M. Knupfer and H. Peisert, "Electronic properties of interfaces between model organic semiconductors and metals," *physica status solidi (a)*, vol. 201, no. 6, pp. 1055–1074, 2004.

[28] N. Koch, "Energy levels at interfaces between metals and conjugated organic molecules," *Journal of Physics: Condensed Matter*, vol. 20, no. 18, p. 184 008, 2008.

[29] M. Oehzelt, K. Akaike, N. Koch, and G. Heimel, "Energy-level alignment at organic heterointerfaces," *Science Advances*, vol. 1, no. 10, e1501127, 2015.

[30] R. A. K. Yadav, D. K. Dubey, S.-Z. Chen, T.-W. Liang, and J.-H. Jou, "Role of molecular orbital energy levels in oled performance," *Scientific Reports*, vol. 10, no. 1, pp. 1–15, 2020.

[31] S. Li, L. Zhan, Y. Jin, G. Zhou, T.-K. Lau, R. Qin, M. Shi, C.-Z. Li, H. Zhu, X. Lu, *et al.*, "Asymmetric electron acceptors for high-efficiency and low-energy-loss organic photovoltaics," *Advanced Materials*, vol. 32, no. 24, p. 2 001 160, 2020.

[32] H. Ishii, K. Sugiyama, E. Ito, and K. Seki, "Energy level alignment and interfacial electronic structures at organic/metal and organic/organic interfaces," *Advanced Materials*, vol. 11, no. 8, pp. 605–625, 1999.

[33] S. Braun, W. Osikowicz, Y. Wang, and W. R. Salaneck, "Energy level alignment regimes at hybrid organic–organic and inorganic–organic interfaces," *Organic Electronics*, vol. 8, no. 1, pp. 14–20, 2007.

[34] M. S. Khoshkhoo, H. Peisert, T. Chassé, and M. Scheele, "The role of the density of interface states in interfacial energy level alignment of ptcda," *Organic Electronics*, vol. 49, pp. 249–254, 2017.

[35] F. Zhang, A. Vollmer, J. Zhang, Z. Xu, J. Rabe, and N. Koch, "Energy level alignment and morphology of interfaces between molecular and polymeric organic semiconductors," *Organic Electronics*, vol. 8, no. 5, pp. 606–614, 2007.

[36] I. Hill and A. Kahn, "Energy level alignment at interfaces of organic semiconductor heterostructures," *Journal of Applied Physics*, vol. 84, no. 10, pp. 5583–5586, 1998.

[37] S. Braun, W. R. Salaneck, and M. Fahlman, "Energy-level alignment at organic/metal and organic/organic interfaces," *Advanced Materials*, vol. 21, no. 14-15, pp. 1450–1472, 2009.

[38] P. Li and Z.-H. Lu, "Interface engineering in organic electronics: Energy-level alignment and charge transport," *Small Science*, vol. 1, no. 1, p. 2 000 015, 2021.

[39] T. Schultz, D. Lungwitz, E. Longhi, S. Barlow, S. R. Marder, and N. Koch, "The interlayer method: A universal tool for energy level alignment tuning at inorganic/organic semiconductor heterojunctions," *Advanced Functional Materials*, vol. 31, no. 10, p. 2 010 174, 2021.

[40] S. Blumstengel and N. Koch, "Energy-level alignment at organic–inorganic heterojunctions," in *Optoelectronic Organic–Inorganic Semiconductor Heterojunctions*, CRC Press, 2021, pp. 9–35.

[41] R. Warren, A. Privitera, P. Kaienburg, A. E. Lauritzen, O. Thimm, J. Nelson, and M. K. Riede, "Controlling energy levels and fermi level en route to fully tailored energetics in organic semiconductors," *Nature Communications*, vol. 10, no. 1, pp. 1–7, 2019.

[42] H. Vázquez, W. Gao, F. Flores, and A. Kahn, "Energy level alignment at organic heterojunctions: Role of the charge neutrality level," *Physical Review B*, vol. 71, no. 4, p. 041 306, 2005.

[43] C. Tengstedt, W. Osikowicz, W. R. Salaneck, I. D. Parker, C.-H. Hsu, and M. Fahlman, "Fermi-level pinning at conjugated polymer interfaces," *Applied Physics Letters*, vol. 88, no. 5, p. 053 502, 2006.

[44] A. Franco-Cañellas, S. Duhm, A. Gerlach, and F. Schreiber, "Binding and electronic level alignment of π-conjugated systems on metals," *Reports on Progress in Physics*, vol. 83, no. 6, p. 066 501, 2020.

[45] K. Yonezawa, A. Hinderhofer, T. Hosokai, K. Kato, R. Makino, F. Schreiber, N. Ueno, and S. Kera, "Structural defects control the energy level alignment at organic/organic interfaces," *Advanced Materials Interfaces*, vol. 1, no. 5, p. 1 400 004, 2014.

[46] M. Oehzelt, N. Koch, and G. Heimel, "Organic semiconductor density of states controls the energy level alignment at electrode interfaces," *Nature Communications*, vol. 5, no. 1, pp. 1–8, 2014.

[47] N. D. Treat, P. Westacott, and N. Stingelin, "The power of materials science tools for gaining insights into organic semiconductors," *Annual Review of Materials Research*, vol. 45, pp. 459–490, 2015.

[48] A. Hinderhofer, T. Hosokai, C. Frank, J. Novák, A. Gerlach, and F. Schreiber, "Templating effect for organic heterostructure film growth: Perfluoropentacene on diindenoperylene," *The Journal of Physical Chemistry C*, vol. 115, no. 32, pp. 16 155–16 160, 2011.

[49] A. Hinderhofer, U. Heinemeyer, A. Gerlach, S. Kowarik, R. M. Jacobs, Y. Sakamoto, T. Suzuki, and F. Schreiber, "Optical properties of pentacene and perfluoropentacene thin films," *The Journal of Chemical Physics*, vol. 127, no. 19, p. 194 705, 2007.

[50] F. Bussolotti, S. Kera, K. Kudo, A. Kahn, and N. Ueno, "Gap states in pentacene thin film induced by inert gas exposure," *Physical Review Letters*, vol. 110, no. 26, p. 267 602, 2013.

[51] H. Y. Mao, F. Bussolotti, D.-C. Qi, R. Wang, S. Kera, N. Ueno, A. T. S. Wee, and W. Chen, "Mechanism of the fermi level pinning at organic donor–acceptor heterojunction interfaces," *Organic Electronics*, vol. 12, no. 3, pp. 534–540, 2011.

[52] F. Bussolotti, J. Yang, M. Hiramoto, T. Kaji, S. Kera, and N. Ueno, "Direct detection of density of gap states in c 60 single crystals by photoemission spectroscopy," *Physical Review B*, vol. 92, no. 11, p. 115 102, 2015.

[53] F. Bussolotti, J. Yang, A. Hinderhofer, Y. Huang, W. Chen, S. Kera, A. T. Wee, and N. Ueno, "Origin of the energy level alignment at organic/organic interfaces: The role of structural defects," *Physical Review B*, vol. 89, no. 11, p. 115 319, 2014.

[54] W. Brütting, *Physics of Organic Semiconductors*. Wiley Online Library, 2005.

[55] A. Köhler and H. Bässler, *Electronic processes in organic semiconductors: An introduction*. John Wiley & Sons, 2015.

[56] F. So, *Organic electronics: materials, processing, devices and applications*. CRC press, 2009.

[57] L. Ficke and M. Cahay, "The bright future of organic leds," *IEEE Potentials*, vol. 23, no. 5, pp. 31–34, 2004.

[58] M. Pope and C. E. Swenberg, "Electronic processes in organic solids," *Annual Review of Physical Chemistry*, vol. 35, no. 1, pp. 613–655, 1984.

[59] P. J. Collings, "Simple measurement of the band gap in silicon and germanium," *American Journal of Physics*, vol. 48, no. 3, pp. 197–199, 1980.

[60] H. Bässler and A. Köhler, "Charge transport in organic semiconductors," *Unimolecular and supramolecular electronics I*, pp. 1–65, 2011.

[61] J. B. Birks, "Photophysics of aromatic molecules," 1970.

[62] D. Beljonne, J. Cornil, L. Muccioli, C. Zannoni, J.-L. Brédas, and F. Castet, "Electronic processes at organic- organic interfaces: Insight from modeling and implications for opto-electronic devices," *Chemistry of Materials*, vol. 23, no. 3, pp. 591–609, 2011.

[63] J. Zhang, W. Xu, P. Sheng, G. Zhao, and D. Zhu, "Organic donor–acceptor complexes as novel organic semiconductors," *Accounts of Chemical Research*, vol. 50, no. 7, pp. 1654–1662, 2017.

[64] K. Ide, K. Nomura, H. Hosono, and T. Kamiya, "Electronic defects in amorphous oxide semiconductors: A review," *physica status solidi (a)*, vol. 216, no. 5, p. 1 800 372, 2019.

[65] E. A. Silinsh, *Organic molecular crystals: their electronic states*. Springer Science & Business Media, 2012, vol. 16.

[66] J. D. Wright, *Molecular crystals*. Cambridge University Press, 1995.

[67] T. K. Das and S. Prusty, "Review on conducting polymers and their applications," *Polymer-plastics technology and engineering*, vol. 51, no. 14, pp. 1487–1500, 2012.

[68] P. W. Atkins and R. S. Friedman, *Molecular quantum mechanics*. Oxford university press, 2011.

[69] W. Demtröder, *Molekülphysik*. Oldenbourg Wissenschaftsverlag, 2013.

[70] Vladsinger. "The various representations of benzene." (2009), [Online]. Available: `https://en.wikipedia.org/wiki/Benzene#/media/File:Benzene_Representations.svg` (visited on 07/08/2021).

[71] M. Pope, C. E. Swenberg, *et al.*, *Electronic processes in organic crystals and polymers*. Oxford University Press on Demand, 1999, vol. 39.

[72] G. Pfister, "Hopping transport in a molecularly doped organic polymer," *Physical Review B*, vol. 16, no. 8, p. 3676, 1977.

[73] S. Kera and N. Ueno, "Photoelectron spectroscopy on the charge reorganization energy and small polaron binding energy of molecular film," *Journal of Electron Spectroscopy and Related Phenomena*, vol. 204, pp. 2–11, 2015.

[74] A. A. Dulov, "Electronic properties and structure of polymeric organic semiconductors," *Russian Chemical Reviews*, vol. 35, no. 10, pp. 773–789, 1966.

[75] S. Aftergut and G. Brown, "Electronic properties of phenazine," *Nature*, vol. 189, no. 4767, pp. 827–828, 1961.

[76] L. Friedman, "Transport properties of organic semiconductors," *Physical Review*, vol. 133, no. 6A, A1668, 1964.

[77] R. Haddon, T. Siegrist, R. Fleming, P. Bridenbaugh, and R. Laudise, "Band structures of organic thin-film transistor materials," *Journal of Materials Chemistry*, vol. 5, no. 10, pp. 1719–1724, 1995.

[78] H. F. Haneef, A. M. Zeidell, and O. D. Jurchescu, "Charge carrier traps in organic semiconductors: A review on the underlying physics and impact on electronic devices," *Journal of Materials Chemistry C*, vol. 8, no. 3, pp. 759–787, 2020.

[79] M. Geiger, L. Schwarz, U. Zschieschang, D. Manske, J. Pflaum, J. Weis, H. Klauk, and R. T. Weitz, "Quantitative analysis of the density of trap states in semiconductors by electrical transport measurements on low-voltage field-effect transistors," *Physical Review Applied*, vol. 10, no. 4, p. 044 023, 2018.

[80] S. Park, S. H. Kim, H. H. Choi, B. Kang, and K. Cho, "Recent advances in the bias stress stability of organic transistors," *Advanced Functional Materials*, vol. 30, no. 20, p. 1 904 590, 2020.

[81] T.-P. Nguyen, "Defect analysis in organic semiconductors," *Materials science in semiconductor processing*, vol. 9, no. 1-3, pp. 198–203, 2006.

[82] J. E. Anthony, A. Facchetti, M. Heeney, S. R. Marder, and X. Zhan, "N-type organic semiconductors in organic electronics," *Advanced Materials*, vol. 22, no. 34, pp. 3876–3892, 2010.

[83] M. Kuik, G.-J. A. Wetzelaer, H. T. Nicolai, N. I. Craciun, D. M. De Leeuw, and P. W. Blom, "25th anniversary article: Charge transport and recombination in polymer light-emitting diodes," *Advanced Materials*, vol. 26, no. 4, pp. 512–531, 2014.

[84] J.-L. Brédas, J. P. Calbert, D. da Silva Filho, and J. Cornil, "Organic semiconductors: A theoretical characterization of the basic parameters governing charge transport," *Proceedings of the National Academy of Sciences*, vol. 99, no. 9, pp. 5804–5809, 2002.

[85] A. Troisi and G. Orlandi, "Dynamics of the intermolecular transfer integral in crystalline organic semiconductors," *The Journal of Physical Chemistry A*, vol. 110, no. 11, pp. 4065–4070, 2006.

[86] V. Arkhipov, P. Heremans, E. Emelianova, G. Adriaenssens, and H. Bässler, "Weak-field carrier hopping in disordered organic semiconductors: The effects of deep traps and partly filled density-of-states distribution," *Journal of Physics: Condensed Matter*, vol. 14, no. 42, p. 9899, 2002.

[87] A. Völkel, R. Street, and D. Knipp, "Carrier transport and density of state distributions in pentacene transistors," *Physical Review B*, vol. 66, no. 19, p. 195 336, 2002.

[88] S. Baranovskii, "Theoretical description of charge transport in disordered organic semiconductors," *physica status solidi (b)*, vol. 251, no. 3, pp. 487–525, 2014.

[89] J. Thomas and J. Williams, *Progress in solid-state chemistry; h. reiss and jo mccaldin, ed*, 1971.

[90] H. Hintz, H.-J. Egelhaaf, L. Lüer, J. Hauch, H. Peisert, and T. Chassé, "Photodegradation of p3ht- a systematic study of environmental factors," *Chemistry of Materials*, vol. 23, no. 2, pp. 145–154, 2011.

[91] T. Sueyoshi, H. Kakuta, M. Ono, K. Sakamoto, S. Kera, and N. Ueno, "Band gap states of copper phthalocyanine thin films induced by nitrogen exposure," *Applied Physics Letters*, vol. 96, no. 9, p. 39, 2010.

[92] J. E. Northrup and M. L. Chabinyc, "Gap states in organic semiconductors: Hydrogen-and oxygen-induced states in pentacene," *Physical Review B*, vol. 68, no. 4, p. 041 202, 2003.

[93] I. Fishchuk, A. Kadashchuk, J. Genoe, M. Ullah, H. Sitter, T. B. Singh, N. Sariciftci, and H. Bässler, "Temperature dependence of the charge carrier mobility in disordered organic semiconductors at large carrier concentrations," *Physical Review B*, vol. 81, no. 4, p. 045 202, 2010.

[94] S. Fratini, D. Mayou, and S. Ciuchi, "The transient localization scenario for charge transport in crystalline organic materials," *Advanced Functional Materials*, vol. 26, no. 14, pp. 2292–2315, 2016.

[95] P. W. Anderson, "Absence of diffusion in certain random lattices," *Physical Review*, vol. 109, no. 5, p. 1492, 1958.

[96] J. Hagenlocher, N. Scheffczyk, K. Broch, G. Duva, N. Rußegger, L. Egenberger, R. Banerjee, S. Kera, F. Schreiber, and A. Hinderhofer, "On the origin of gap states in molecular semiconductors—a combined ups, afm, and x-ray diffraction study," *The Journal of Physical Chemistry C*, vol. 125, no. 32, pp. 17 929–17 938, 2021.

[97] T. Michely and J. Krug, *Islands, mounds and atoms*. Springer Science & Business Media, 2012, vol. 42.

[98] P. K. Nayak, R. Rosenberg, L. Barnea-Nehoshtan, and D. Cahen, "O2 and organic semiconductors: Electronic effects," *Organic Electronics*, vol. 14, no. 3, pp. 966–972, 2013.

[99] J. H. Kang, D. da Silva Filho, J.-L. Bredas, and X.-Y. Zhu, "Shallow trap states in pentacene thin films from molecular sliding," *Applied Physics Letters*, vol. 86, no. 15, p. 152 115, 2005.

[100] F. Lohmann and W. Mehl, "Dark injection and radiative recombination of electrons and holes in naphthalene crystals," *The Journal of Chemical Physics*, vol. 50, no. 1, pp. 500–506, 1969.

[101] S. Verlaak and P. Heremans, "Molecular microelectrostatic view on electronic states near pentacene grain boundaries," *Physical Review B*, vol. 75, no. 11, p. 115 127, 2007.

[102] M. Schwoerer and H. C. Wolf, *Organic molecular solids*. John Wiley & Sons, 2007.

[103] J. Krug, "Boundary-induced phase transitions in driven diffusive systems," *Physical Review Letters*, vol. 67, no. 14, p. 1882, 1991.

[104] H. H. Choi, A. F. Paterson, M. A. Fusella, J. Panidi, O. Solomeshch, N. Tessler, M. Heeney, K. Cho, T. D. Anthopoulos, B. P. Rand, *et al.*, "Hall effect in polycrystalline organic semiconductors: The effect of grain boundaries," *Advanced Functional Materials*, vol. 30, no. 20, p. 1 903 617, 2020.

[105] J. Rivnay, L. H. Jimison, J. E. Northrup, M. F. Toney, R. Noriega, S. Lu, T. J. Marks, A. Facchetti, and A. Salleo, "Large modulation of carrier transport by grain-boundary molecular packing and microstructure in organic thin films," *Nature Materials*, vol. 8, no. 12, pp. 952–958, 2009.

[106] A. Dürr, F. Schreiber, M. Münch, N. Karl, B. Krause, V. Kruppa, and H. Dosch, "High structural order in thin films of the organic semiconductor diindenoperylene," *Applied Physics Letters*, vol. 81, no. 12, pp. 2276–2278, 2002.

[107] A. Hinderhofer, K. Yonezawa, K. Kato, and F. Schreiber, "Structure matters: Combining x-ray scattering and ultraviolet photoelectron spectroscopy for studying organic thin films," in *Electronic Processes in Organic Electronics*, Springer, 2015, pp. 109–129.

[108] H. Peisert, D. Kolacyak, and T. Chassé, "Site-specific charge-transfer screening at organic/metal interfaces," *The Journal of Physical Chemistry C*, vol. 113, no. 44, pp. 19 244–19 250, 2009.

[109] T. Kirchartz, W. Gong, S. A. Hawks, T. Agostinelli, R. C. MacKenzie, Y. Yang, and J. Nelson, "Sensitivity of the mott–schottky analysis in organic solar cells," *The Journal of Physical Chemistry C*, vol. 116, no. 14, pp. 7672–7680, 2012.

[110] H. Peisert, A. Petr, L. Dunsch, T. Chassé, and M. Knupfer, "Interface fermi level pinning at contacts between pedot: Pss and molecular organic semiconductors," *ChemPhysChem*, vol. 8, no. 3, pp. 386–390, 2007.

[111] S. Zhong, J. Q. Zhong, H. Y. Mao, J. L. Zhang, J. D. Lin, and W. Chen, "The role of gap states in the energy level alignment at the organic–organic heterojunction interfaces," *Physical Chemistry Chemical Physics*, vol. 14, no. 41, pp. 14 127–14 141, 2012.

[112] J. Tang, C. Lee, and S. Lee, "Electronic structures of organic/organic heterojunctions: From vacuum level alignment to fermi level pinning," *Journal of Applied Physics*, vol. 101, no. 6, p. 064 504, 2007.

[113] S. Hüfner, *Photoelectron spectroscopy: principles and applications*. Springer Science & Business Media, 2013.

[114] C. Brundle, "The application of electron spectroscopy to surface studies," *Journal of Vacuum Science and Technology*, vol. 11, no. 1, pp. 212–224, 1974.

[115] Y. Nakayama, S. Kera, and N. Ueno, "Photoelectron spectroscopy on single crystals of organic semiconductors: Experimental electronic band structure for optoelectronic properties," *Journal of Materials Chemistry C*, vol. 8, no. 27, pp. 9090–9132, 2020.

[116] A. Einstein, "Einstein 1906," *Annalen der Physik*, vol. 20, p. 199, 1906.

[117] H. Yoshida, "Low-energy inverse photoemission spectroscopy using a high-resolution grating spectrometer in the near ultraviolet range," *Review of Scientific Instruments*, vol. 84, no. 10, p. 103 901, 2013.

[118] J. D. van der Waals, *Lehrbuch der Thermodynamik*. BoD–Books on Demand, 2012, vol. 7.

[119] A. Tkatchenko, L. Romaner, O. T. Hofmann, E. Zojer, C. Ambrosch-Draxl, and M. Scheffler, "Van der waals interactions between organic adsorbates and at organic/inorganic interfaces," *MRS bulletin*, vol. 35, no. 6, pp. 435–442, 2010.

[120] R. Chakrabarti and P. G. Vekilov, "Attraction between permanent dipoles and london dispersion forces dominate the thermodynamics of organic crystallization," *Crystal Growth & Design*, vol. 20, no. 11, pp. 7429–7438, 2020.

[121] M. A. Strauss and H. A. Wegner, "Molecular systems for the quantification of london dispersion interactions," *European Journal of Organic Chemistry*, vol. 2019, no. 2-3, pp. 295–302, 2019.

[122] Y. Zhao, H. T. Ng, E. Hanson, J. Dong, D. S. Corti, and E. I. Franses, "Computation of nonretarded london dispersion coefficients and hamaker constants of copper phthalocyanine," *Journal of chemical theory and computation*, vol. 6, no. 2, pp. 491–498, 2010.

[123] A. Baskaran and P. Smereka, "Mechanisms of stranski-krastanov growth," *Journal of Applied Physics*, vol. 111, no. 4, p. 044 321, 2012.

[124] U. Heinemeyer, "Optical properties of organic semiconductor thin films: Static spectra and real-time growth studies.," Ph.D. dissertation, Eberhard-Karls-Universität Tübingen, 2009.

[125] F. Schreiber, "Structure and growth of self-assembling monolayers," *Progress in Surface Science*, vol. 65, no. 5-8, pp. 151–257, 2000.

[126] L. Casalis, M. Danisman, B. Nickel, G. Bracco, T. Toccoli, S. Iannotta, and G. Scoles, "Hyperthermal molecular beam deposition of highly ordered organic thin films," *Physical Review Letters*, vol. 90, no. 20, p. 206 101, 2003.

[127] A. Hinderhofer, J. Hagenlocher, A. Gerlach, J. Krug, M. Oettel, and F. Schreiber, "Non-equilibrium roughness evolution of small molecule mixed films reflecting equilibrium phase behavior," *arXiv preprint arXiv:2103.04754*, 2021.

[128] A.-L. Barabási, H. E. Stanley, *et al.*, *Fractal concepts in surface growth*. Cambridge university press, 1995.

[129] P. Meakin, *Fractals, scaling and growth far from equilibrium*. Cambridge university press, 1998, vol. 5.

[130] E. Empting, M. Klopotek, A. Hinderhofer, F. Schreiber, and M. Oettel, "Lattice gas study of thin-film growth scenarios and transitions between them: Role of substrate," *Physical Review E*, vol. 103, no. 2, p. 023 302, 2021.

[131] J. Krug, "Origins of scale invariance in growth processes," *Advances in Physics*, vol. 46, no. 2, pp. 139–282, 1997.

[132] "Schematic representation of the ehrlich-schwöbel barrier." (2002), [Online]. Available: `https://pubs.rsc.org/services/images/RSCpubs.ePlatform.Service.FreeContent.ImageService.svc/ImageService/Articleimage/2002/FD/b110802f/b110802f-s1.gif` (visited on 07/08/2021).

[133] G. Hlawacek, P. Puschnig, P. Frank, A. Winkler, C. Ambrosch-Draxl, and C. Teichert, "Characterization of step-edge barriers in organic thin-film growth," *Science*, vol. 321, no. 5885, pp. 108–111, 2008.

[134] X. Zhang, E. Barrena, D. Goswami, D. G. de Oteyza, C. Weis, and H. Dosch, "Evidence for a layer-dependent ehrlich-schwöbel barrier in organic thin film growth," *Physical Review Letters*, vol. 103, no. 13, p. 136 101, 2009.

[135] H. Yoshida, K. Yamada, J. Tsutsumi, and N. Sato, "Complete description of ionization energy and electron affinity in organic solids: Determining contributions from electronic polarization, energy band dispersion, and molecular orientation," *Physical Review B*, vol. 92, no. 7, p. 075 145, 2015.

[136] M. Kitamura and Y. Arakawa, "Pentacene-based organic field-effect transistors," *Journal of Physics: Condensed Matter*, vol. 20, no. 18, p. 184 011, 2008.

[137] G. Cady, A. Grosse, E. Barber, L. Burger, and Z. Sheldon, "Preparation of fluorocarbons by catalytic fluorination of hydrocarbons," *Industrial & Engineering Chemistry*, vol. 39, no. 3, pp. 290–292, 1947.

[138] J. Liu, N. Zheng, Z. Hu, Z. Wang, X. Yang, F. Huang, and Y. Cao, "Self-doped n-type small molecular electron transport materials for high-performance organic solar cells," *Science China Chemistry*, vol. 60, no. 8, pp. 1136–1144, 2017.

[139] E. Katz, "Fullerene-based thin films as a novel polycrystalline semiconductor," in *Solid State Phenomena*, Trans Tech Publ, vol. 67, 1999, pp. 435–446.

[140] A. Ray, "Fullerence (c60) molecule–a review," *Asian Journal of Pharmaceutical Research*, vol. 2, no. 2, pp. 47–50, 2012.

[141] E. A. Katz, "Fullerene thin films as photovoltaic material," in *Nanostructured materials for solar energy conversion*, Elsevier, 2006, pp. 361–443.

[142] T. Tada, N. Uchida, T. Kanayama, H. Hiura, and K. Kimoto, "Charge-transfer doping by fullerenes on oxidized si surfaces," *Journal of Applied Physics*, vol. 102, no. 7, p. 074 504, 2007.

[143] P. A. Heiney, J. E. Fischer, A. R. McGhie, W. J. Romanow, A. M. Denenstein, J. P. McCauley Jr, A. B. Smith, and D. E. Cox, "Orientational ordering transition in solid c 60," *Physical Review Letters*, vol. 66, no. 22, p. 2911, 1991.

[144] Y. Kubozono, X. He, S. Hamao, K. Teranishi, H. Goto, R. Eguchi, T. Kambe, S. Gohda, and Y. Nishihara, "Transistor application of phenacene molecules and their characteristics," *European Journal of Inorganic Chemistry*, vol. 2014, no. 24, pp. 3806–3819, 2014.

[145] A. Al Ruzaiqi, H. Okamoto, Y. Kubozono, U. Zschieschang, H. Klauk, P. Baran, and H. Gleskova, "Low-voltage organic thin-film transistors based on [n] phenacenes," *Organic Electronics*, vol. 73, pp. 286–291, 2019.

[146] H. Okamoto, R. Eguchi, S. Hamao, H. Goto, K. Gotoh, Y. Sakai, M. Izumi, Y. Takaguchi, S. Gohda, and Y. Kubozono, "An extended phenacene-type molecule,[8] phenacene: Synthesis and transistor application," *Scientific Reports*, vol. 4, no. 1, pp. 1–8, 2014.

[147] T. Hosokai, A. Hinderhofer, F. Bussolotti, K. Yonezawa, C. Lorch, A. Vorobiev, Y. Hasegawa, Y. Yamada, Y. Kubozoro, A. Gerlach, *et al.*, "Thickness and substrate dependent thin film growth of picene and impact on the electronic structure," *The Journal of Physical Chemistry C*, vol. 119, no. 52, pp. 29 027–29 037, 2015.

[148] P. I. Djurovich, E. I. Mayo, S. R. Forrest, and M. E. Thompson, "Measurement of the lowest unoccupied molecular orbital energies of molecular organic semiconductors," *Organic Electronics*, vol. 10, no. 3, pp. 515–520, 2009.

[149] E. L. Granstrom and C. D. Frisbie, "Field effect conductance measurements on thin crystals of sexithiophene," *The Journal of Physical Chemistry B*, vol. 103, no. 42, pp. 8842–8849, 1999.

[150] J. Kalinowski, W. Stampor, P. Di Marco, and F. Garnier, "Photogeneration of charge in solid films of α-sexithiophene," *Chemical Physics*, vol. 237, no. 1-2, pp. 233–243, 1998.

[151] C. Lorch, R. Banerjee, J. Dieterle, A. Hinderhofer, A. Gerlach, J. Drnec, and F. Schreiber, "Templating effects of α-sexithiophene in donor–acceptor organic thin films," *The Journal of Physical Chemistry C*, vol. 119, no. 40, pp. 23 211–23 220, 2015.

[152] M. Riede, C. Uhrich, J. Widmer, R. Timmreck, D. Wynands, G. Schwartz, W.-M. Gnehr, D. Hildebrandt, A. Weiss, J. Hwang, *et al.*, "Efficient organic tandem solar cells based on small molecules," *Advanced Functional Materials*, vol. 21, no. 16, pp. 3019–3028, 2011.

[153] K. Asadi, Y. Wu, F. Gholamrezaie, P. Rudolf, and P. W. Blom, "Single-layer pentacene field-effect transistors using electrodes modified with self-assembled monolayers," *Advanced Materials*, vol. 21, no. 41, pp. 4109–4114, 2009.

[154] S. R. Forrest, "Ultrathin organic films grown by organic molecular beam deposition and related techniques," *Chemical Reviews*, vol. 97, no. 6, pp. 1793–1896, 1997.

[155] S. Kowarik, A. Gerlach, and F. Schreiber, "Organic molecular beam deposition: Fundamentals, growth dynamics, and in situ studies," *Journal of Physics: Condensed Matter*, vol. 20, no. 18, p. 184 005, 2008.

[156] K. D. Carlson, P. W. Gilles, and R. Thorn, "Molecular and hydrodynamical effusion of mercury vapor from knudsen cells," *The Journal of Chemical Physics*, vol. 38, no. 11, pp. 2725–2735, 1963.

[157] M. Kytka, "Ph.d. thesis," Ph.D. dissertation, Slovak University of Technology in Bratislava and Eberhard-Karls-Universität Tübingen, 2008.

[158] E. Benes, "Improved quartz crystal microbalance technique," *Journal of Applied Physics*, vol. 56, no. 3, pp. 608–626, 1984.

[159] G. A. Somorjai, "Modern surface science and surface technologies: An introduction," *Chemical Reviews*, vol. 96, no. 4, pp. 1223–1236, 1996.

[160] P. W. Palmberg, "Ultrahigh vacuum and surface science," *Journal of Vacuum Science & Technology A: Vacuum, Surfaces, and Films*, vol. 12, no. 4, pp. 946–952, 1994.

[161] G. F. Weston, *Ultrahigh vacuum practice*. Elsevier, 2013.

[162] J. Als-Nielsen and D. McMorrow, *Elements of Modern X-ray Physics*. John Wiley & Sons, 2011.

[163] M. Birkholz, *Thin Film analysis by X-ray Scattering*. John Wiley & Sons, 2006.

[164] M. Tolan and M. Tolan, *X-ray Scattering from Soft-Matter Thin Films: Materials Science and Basic Research*. Springer, 1999, vol. 148.

[165] M. K. Huss-Hansen, J. Kjelstrup-Hansen, and M. Knaapila, "Structural effects of electrode proximity in vacuum deposited organic semiconductors studied by microfocused x-ray scattering," *Advanced Engineering Materials*, 2021.

[166] E. Vlieg, "Integrated intensities using a six-circle surface x-ray diffractometer," *Journal of Applied Crystallography*, vol. 30, no. 5, pp. 532–543, 1997.

[167] B. Nickel, R. Barabash, R. Ruiz, N. Koch, A. Kahn, L. Feldman, R. Haglund, and G. Scoles, "Dislocation arrangements in pentacene thin films," *Physical Review B*, vol. 70, no. 12, p. 125 401, 2004.

[168] S. Kowarik, "Real-time studies of thin film growth of organic semiconductors," Ph.D. dissertation, Wadham College, Oxford, 2006.

[169] P. Scherrer, "Bestimmung der inneren struktur und der grösse von kolloidteilchen mittels röntgenstrahlen," in *Kolloidchemie Ein Lehrbuch*, Springer, 1912, pp. 387–409.

[170] C. Nicklin, T. Arnold, J. Rawle, and A. Warne, "Diamond beamline i07: A beamline for surface and interface diffraction," *Journal of Synchrotron Radiation*, vol. 23, no. 5, pp. 1245–1253, 2016.

[171] G. Renaud, Y. Garreau, P. Betinelli, A. Tournieux, J. Bisou, P. Monteiro, and X. Elattaoui, "Beamline fast and automatic attenuation system for x-ray detectors at synchrotron soleil," in *Journal of Physics: Conference Series*, IOP Publishing, vol. 425, 2013, p. 082 003.

[172] O. Balmes, R. van Rijn, D. Wermeille, A. Resta, L. Petit, H. Isern, T. Dufrane, and R. Felici, "The id03 surface diffraction beamline for in-situ and real-time x-ray investigations of catalytic reactions at surfaces," *Catalysis Today*, vol. 145, no. 3-4, pp. 220–226, 2009.

[173] Y. Chushkin, F. Zontone, E. Lima, L. De Caro, P. Guardia, L. Manna, and C. Giannini, "Three-dimensional coherent diffractive imaging on non-periodic specimens at the esrf beamline id10," *Journal of Synchrotron Radiation*, vol. 21, no. 3, pp. 594–599, 2014.

[174] F. Schreiber, "Organic molecular beam deposition: Growth studies beyond the first monolayer," *physica status solidi (a)*, vol. 201, no. 6, pp. 1037–1054, 2004.

[175] V. J. Rao, M. Matthiesen, K. P. Goetz, C. Huck, C. Yim, R. Siris, J. Han, S. Hahn, U. H. Bunz, A. Dreuw, *et al.*, "Afm-ir and ir-snom for the characterization of small molecule organic semiconductors," *The Journal of Physical Chemistry C*, vol. 124, no. 9, pp. 5331–5344, 2020.

[176] F. J. Giessibl, "Principle of nc-afm," in *Noncontact Atomic Force Microscopy*, Springer, 2002, pp. 11–46.

[177] J. Te Riet, A. J. Katan, C. Rankl, S. W. Stahl, A. M. van Buul, I. Y. Phang, A. Gomez-Casado, P. Schön, J. W. Gerritsen, A. Cambi, *et al.*, "Interlaboratory round robin on cantilever calibration for afm force spectroscopy," *Ultramicroscopy*, vol. 111, no. 12, pp. 1659–1669, 2011.

[178] D. Nečas and P. Klapetek, "Gwyddion: An open-source software for spm data analysis," *Open Physics*, vol. 10, no. 1, pp. 181–188, 2012.

[179] F. Bussolotti, "High-sensitivity ultraviolet photoemission spectroscopy technique for direct detection of gap states in organic thin films," *Journal of Electron Spectroscopy and Related Phenomena*, vol. 204, pp. 29–38, 2015.

[180] Z. Xie, I. Baldea, and C. D. Frisbie, "Determination of energy-level alignment in molecular tunnel junctions by transport and spectroscopy: Self-consistency for the case of oligophenylene thiols and dithiols on ag, au, and pt electrodes," *Journal of the American Chemical Society*, vol. 141, no. 8, pp. 3670–3681, 2019.

[181] K. Cnops, G. Zango, J. Genoe, P. Heremans, M. V. Martinez-Diaz, T. Torres, and D. Cheyns, "Energy level tuning of non fullerene acceptors in organic solar cells," *Journal of the American Chemical Society*, vol. 137, no. 28, pp. 8991–8997, 2015.

[182] W. Chen, D. C. Qi, Y. L. Huang, H. Huang, Y. Z. Wang, S. Chen, X. Y. Gao, and A. T. S. Wee, "Molecular orientation dependent energy level alignment at organic organic heterojunction interfaces," *Journal of Physical Chemistry C*, vol. 113, no. 29, pp. 12 832–12 839, 2009.

[183] I. Salzmann, S. Duhm, G. Heimel, M. Oehzelt, R. Kniprath, R. L. Johnson, J. P. Rabe, and N. Koch, "Tuning the ionization energy of organic semiconductor films: The role of intramolecular polar bonds," *Journal of the American Chemical Society*, vol. 130, no. 39, pp. 12 870–12 871, 2008.

[184] H. Wang, S. V. Levchenko, T. Schultz, N. Koch, M. Scheffler, and M. Rossi, "Modulation of the work function by the atomic structure of strong organic electron acceptors on h-si (111)," *Advanced Electronic Materials*, vol. 5, no. 5, p. 1 800 891, 2019.

[185] J.-P. Yang, F. Bussolotti, S. Kera, and N. Ueno, "Origin and role of gap states in organic semiconductor studied by ups: As the nature of organic molecular crystals," *Journal of Physics D: Applied Physics*, vol. 50, no. 42, p. 423 002, 2017.

[186] S.-C. Li, J.-g. Wang, P. Jacobson, X.-Q. Gong, A. Selloni, and U. Diebold, "Correlation between bonding geometry and band gap states at organic inorganic interfaces: Catechol on rutile tio2 (110)," *Journal of the American Chemical Society*, vol. 131, no. 3, pp. 980–984, 2009.

[187] I. Lange, J. C. Blakesley, J. Frisch, A. Vollmer, N. Koch, and D. Neher, "Band bending in conjugated polymer layers," *Physical Review Letters*, vol. 106, no. 21, p. 216 402, 2011.

[188] K. Gmucova, V. Nadazdy, F. Schauer, M. Kaiser, and E. Majkova, "Electrochemical spectroscopic methods for the fine band gap electronic structure mapping in organic semiconductors," *Journal of Physical Chemistry C*, vol. 119, no. 28, pp. 15 926–15 934, 2015.

[189] T.-P. Nguyen, "Defect analysis in organic semiconductors," *Materials Science in Semiconductor Processing*, vol. 9, no. 1-3, pp. 198–203, 2006.

[190] H. J. Queisser and E. E. Haller, "Defects in semiconductors: Some fatal, some vital," *Science*, vol. 281, no. 5379, pp. 945–950, 1998.

[191] T.-P. Nguyen, "Defects in organic electronic devices," *physica status solidi (a)*, vol. 205, no. 1, pp. 162–166, 2008.

[192] Y. S. Yang, S. H. Kim, J.-I. Lee, H. Y. Chu, L.-M. Do, H. Lee, J. Oh, T. Zyung, M. K. Ryu, and M. S. Jang, "Deep level defect characteristics in pentacene organic thin films," *Applied Physics Letters*, vol. 80, no. 9, pp. 1595–1597, 2002.

[193] B. Nickel, R. Barabash, R. Ruiz, N. Koch, A. Kahn, L. C. Feldman, R. Haglund, and G. Scoles, "Dislocation arrangements in pentacene thin films," *Physical Review B*, vol. 70, no. 12, p. 125 401, 2004.

[194] J. Krug, "Origins of scale invariance in growth processes," *Advances in Physics*, vol. 46, no. 2, pp. 139–282, 1997.

[195] C. Frank, J. Novak, A. Gerlach, G. Ligorio, K. Broch, A. Hinderhofer, A. Aufderheide, R. Banerjee, R. Nervo, and F. Schreiber, "Real time x ray scattering studies on temperature dependence of perfluoropentacene thin film growth," *Journal of Applied Physics*, vol. 114, no. 4, p. 043 515, 2013.

[196] N. Komura, H. Goto, X. He, H. Mitamura, R. Eguchi, Y. Kaji, H. Okamoto, Y. Sugawara, S. Gohda, K. Sato, *et al.*, "Characteristics of [6] phenacene thin film field-effect transistor," *Applied Physics Letters*, vol. 101, no. 8, p. 083 301, 2012.

[197] M. Zwadlo, J. Hagara, G. Duva, J. Hagenlocher, A. Gerlach, I. Zaluzhnyy, M. Hodas, A. Hinderhofer, P. Siffalovic, and F. Schreiber, "Structure of thin films of [6] and [7] phenacene and impact of potassium deposition," *Advanced Optical Materials*, p. 2 002 193, 2021.

[198] A. Hinderhofer, A. Gerlach, K. Broch, T. Hosokai, K. Yonezawa, K. Kato, S. Kera, N. Ueno, and F. Schreiber, "Geometric and electronic structure of templated c60 on diindenoperylene thin films," *Journal of Physical Chemistry C*, vol. 117, no. 2, pp. 1053–1058, 2013.

[199] A. Dürr, F. Schreiber, K. Ritley, V. Kruppa, J. Krug, H. Dosch, and B. Struth, "Rapid roughening in thin film growth of an organic semiconductor (diindenoperylene)," *Physical Review Letters*, vol. 90, no. 1, p. 016 104, 2003.

[200] T. Ungar, G. Tichy, J. Gubicza, and R. Hellmig, "Correlation between subgrains and coherently scattering domains," *Powder Diffraction*, vol. 20, no. 4, pp. 366–375, 2005.

[201] N. Camillone III, C. E. Chidsey, P. Eisenberger, P. Fenter, J. Li, K. Liang, G.-Y. Liu, and G. Scoles, "Structural defects in self assembled organic monolayers via combined atomic beam and x ray diffraction," *Journal of Chemical Physics*, vol. 99, no. 1, pp. 744–747, 1993.

[202] N. Yamoah, M. Koten, D. Thompson, C. Nannuri, J. Narayan, J. Shield, and D. Kumar, "Dependence of grain size and defect density on the magnetic properties of mechanically alloyed fe90w10 powder," *Journal of Applied Physics*, vol. 120, no. 14, p. 143 903, 2016.

[203] T. Kamei, M. Kondo, and A. Matsuda, "A significant reduction of impurity contents in hydrogenated microcrystalline silicon films for increased grain size and reduced defect density," *Japanese Journal of Applied Physics*, vol. 37, no. 3A, p. L265, 1998.

[204] H. Vazquez, F. Flores, and A. Kahn, "Induced density of states model for weakly-interacting organic semiconductor interfaces," *Organic Electronics*, vol. 8, no. 2-3, pp. 241–248, 2007.

[205] H. Yoshida, K. Yamada, J. Tsutsumi, and N. Sato, "Complete description of ionization energy and electron affinity in organic solids: Determining contributions from electronic polarization, energy band dispersion, and molecular orientation," *Physical Review B*, vol. 92, no. 7, p. 075 145, 2015.

[206] H. Yoshida, "Low-energy inverse photoemission study on the electron affinities of fullerene derivatives for organic photovoltaic cells," *The Journal of Physical Chemistry C*, vol. 118, no. 42, pp. 24 377–24 382, 2014.

[207] S. Verlaak, D. Beljonne, D. Cheyns, C. Rolin, M. Linares, F. Castet, J. Cornil, and P. Heremans, "Electronic structure and geminate pair energetics at organic organic interfaces: The case of pentacene/c60 heterojunctions," *Advanced Functional Materials*, vol. 19, no. 23, pp. 3809–3814, 2009.

[208] S. Duhm, G. Heimel, I. Salzmann, H. Glowatzki, R. L. Johnson, A. Vollmer, J. P. Rabe, and N. Koch, "Orientation-dependent ionization energies and interface dipoles in ordered molecular assemblies," *Nature Materials*, vol. 7, no. 4, pp. 326–332, 2008.

[209] J. Hagenlocher, A. Hinderhofer, C. Zeiser, K. Broch, A. Greco, Q. Wang, G. Duva, N. Russegger, R. Banerjee, A. Gerlach, F. Bussolotti, J.-P. Yang, N. Ueno, S. Duhm, S. Kera, F. Schreiber, and A. Hinderhofer, "Energy-level alignment governed by templated gap states in organic-organic heterostructures," *in preparation*, 2021.

[210] S. M. Menke, W. A. Luhman, and R. J. Holmes, "Tailored exciton diffusion in organic photovoltaic cells for enhanced power conversion efficiency," *Nature Materials*, vol. 12, no. 2, pp. 152–157, 2013.

[211] M. Mesta, M. Carvelli, R. J. De Vries, H. Van Eersel, J. J. Van Der Holst, M. Schober, M. Furno, B. Lüssem, K. Leo, P. Loebl, *et al.*, "Molecular-scale simulation of electroluminescence in a multilayer white organic light-emitting diode," *Nature Materials*, vol. 12, no. 7, pp. 652–658, 2013.

[212] C. J. Brabec, A. Cravino, D. Meissner, N. S. Sariciftci, T. Fromherz, M. T. Rispens, L. Sanchez, and J. C. Hummelen, "Origin of the open circuit voltage of plastic solar cells," *Advanced Functional Materials*, vol. 11, no. 5, pp. 374–380, 2001.

[213] S. E. Gledhill, B. Scott, and B. A. Gregg, "Organic and nano-structured composite photovoltaics: An overview," *Journal of Materials Research*, vol. 20, no. 12, pp. 3167–3179, 2005.

[214] S.-M. Lee, J. H. Kwon, S. Kwon, and K. C. Choi, "A review of flexible oleds toward highly durable unusual displays," *IEEE Transactions on Electron Devices*, vol. 64, no. 5, pp. 1922–1931, 2017.

[215] A. Hinderhofer, A. Gerlach, K. Broch, T. Hosokai, K. Yonezawa, K. Kato, S. Kera, N. Ueno, and F. Schreiber, "Geometric and electronic structure of templated c60 on diindenoperylene thin films," *The Journal of Physical Chemistry C*, vol. 117, no. 2, pp. 1053–1058, 2013.

[216] R. Ruiz, D. Choudhary, B. Nickel, T. Toccoli, K.-C. Chang, A. C. Mayer, P. Clancy, J. M. Blakely, R. L. Headrick, S. Iannotta, *et al.*, "Pentacene thin film growth," *Chemistry of Materials*, vol. 16, no. 23, pp. 4497–4508, 2004.

[217] C. Lorch, K. Broch, V. Belova, G. Duva, A. Hinderhofer, A. Gerlach, M. Jankowski, and F. Schreiber, "Growth and annealing kinetics of α-sexithiophene and fullerene c60 mixed films," *Journal of Applied Crystallography*, vol. 49, no. 4, pp. 1266–1275, 2016.

[218] R. Banerjee, A. Hinderhofer, M. Weinmann, B. Reisz, C. Lorch, A. Gerlach, M. Oettel, and F. Schreiber, "Interrupted growth to manipulate phase separation in dip: C60 organic semiconductor blends," *The Journal of Physical Chemistry C*, vol. 122, no. 3, pp. 1839–1845, 2018.

[219] A. Hinderhofer, A. Gerlach, S. Kowarik, F. Zontone, J. Krug, and F. Schreiber, "Smoothing and coherent structure formation in organic-organic heterostructure growth," *EPL (Europhysics Letters)*, vol. 91, no. 5, p. 56 002, 2010.

[220] U. Aygül, D. Batchelor, U. Dettinger, S. Yilmaz, S. Allard, U. Scherf, H. Peisert, and T. Chassé, "Molecular orientation in polymer films for organic solar cells studied by nexafs," *The Journal of Physical Chemistry C*, vol. 116, no. 7, pp. 4870–4874, 2012.

[221] H. Peisert, I. Biswas, M. Knupfer, and T. Chassé, "Orientation and electronic properties of phthalocyanines on polycrystalline substrates," *physica status solidi (b)*, vol. 246, no. 7, pp. 1529–1545, 2009.

[222] A. L. Foggiatto, H. Suga, Y. Takeichi, K. Ono, Y. Takahashi, K. Kutsukake, T. Ueba, S. Kera, and T. Sakurai, "Dependence of substrate work function on the energy-level alignment at organic–organic heterojunction interface," *Japanese Journal of Applied Physics*, vol. 58, 2019.

List of contributions

Contributions by others in this work mainly result from joint visits at synchrotrons during X-ray beamtimes or assistance during UPS experiments at the FUNSOM Institute in Soochow, China and the Institute for Molecular Science in Okazaki, Japan. The name of the cooperation partner group head is given in parentheses.

Sec. 5.1 - "On the origin of gap states"

Sample preparation	-	J.H.
X-ray measurements	-	J.H., K. Broch, R. Banerjee, G. Duva
Structure data analysis	-	J.H.
AFM	-	J.H., N. Scheffczyk
UPS measurements	-	J.H., Y. Hasegawa (Prof. Kera)
UPS data analysis	-	J.H.

Sec. 5.2 - "Energy-level alignment in organic heterostructures"

Sample preparation	-	J.H.
X-ray measurements	-	J.H., G. Duva, K. Broch, A. Hinderhofer, N. Russegger
Structure data analysis	-	J.H.
UPS measurements	-	J.H., W. Qi, H. Jiaxin (Prof. Duhm), M. Meister (Prof. Kera)
UPS measurements C60-on-PEN	-	A.Hinderhofer
UPS data analysis	-	J.H.

Sec. 5.3 - "Thickness-dependent energy-level alignment"

Sample preparation	-	J.H.
X-ray measurements	-	J.H., K. Broch, M. Zwadlo, D. Lepple
Structure data analysis	-	J.H.
UPS measurements	-	J.H.
UPS data analysis	-	J.H.

Publication list

- J. Hagenlocher, K. Broch, M. Zwadlo, D. Lepple, J. Rawle, F. Carla, S. Kera, F. Schreiber, and A. Hinderhofer, "Thickness-dependent energy-level alignment at the organic-organic interface induced by templated gap states", 2022, *Advanced Materials Interfaces*, 9(3), 2101382

- J. Hagenlocher, N. Scheffczyk, K. Broch, G. Duva, N. Russegger, L. Egenberger, R. Banerjee, S. Kera, F. Schreiber, and A. Hinderhofer, "On the origin of gap states in molecular semiconductors - A combined UPS, AFM and X-ray diffraction study", 2021, *J. Phys. Chem. C.*, 125(32), 17929-17938

- M. I. Dar, N. Arora, M. Abdi-Jalebi, A. Hinderhofer, G. Delport, S. Feldmann, G. Jacopin, J. Hagenlocher, Y. Liu, F. Deschler, S. Stranks, S. Zakeeruddin, F. Schreiber, M. Graetzel, R. Friend, "Low-energetic disorder in highly luminescent perovskite films", 2021, *submitted*

- N. Arora, A. Greco, S. Meloni, A. Hinderhofer, A. Mattoni, U. Rothlisberger, J. Hagenlocher, C. Caddeo, S. Zakeeruddin, F. Schreiber, M. Graetzel, R. Friend, M. I. Dar, "Kinetics and energetics of Metal Halide Perovskite Conversion Reactions at the Nanoscale", 2022, *Communications Materials*, 3(1), 22

- C. Zeiser, C. Cruz, D.R. Reichmann, M. Seitz, J. Hagenlocher, E.L. Chronister, C. Bardeem, R. Tempelaar, and K. Broch, "Acene: spacer blends show exothermic singlet fission to proceed coherently, while endothermic fission proceeds incoherently,", 2020 *arXiv preprint*, arXiv:2002.11354, 2021

- L. Merten, A. Hinderhofer, T. Baumeler, N. Arora, J. Hagenlocher, S. Zakeeruddin, M. Dar, M. Grätzel, and F. Schreiber, "Quantifying stabilized phase purity in formamidinium-based multiple-cation hybrid perovskites," *Chem. Mater.*, vol. 33, no. 8, pp. 2769-2776, 2021

- B. Reisz, E. Empting, M. Zwadlo, M. Hodas, G. Duva, V. Belova, C. Zeiser, J. Hagenlocher, S. Maiti, A. Hinderhofer, A. Gerlach, M. Oettel, and F. Schreiber, "Thin film growth of phase-separating phthalocyanine-fullerene blends: A combined experimental and computational study," *Phys. Rev. Materials*, vol. 5, no. 4, 2021

- M. Zwadlo, J. Hagara, G. Duva, J. Hagenlocher, A. Gerlach, M. Hodas, A. Hinderhofer, P. Siffalovic, and F. Schreiber, "Structure of thin films of [6] and [7]phenacene and impact of potassium deposition," *Adv. Optical Mater.*, 2002193, 2021

- A. Hinderhofer, J. Hagenlocher, A. Gerlach, J. Krug, and F. Schreiber, "Non-equilibrium Roughness Evolution of Small Molecule Mixed Films Reflecting Equilibrium Phase Behavior," *arXiv preprint*, arXiv:2103.04754, 2020

- J. Hagara, N. Mrkyvkova, L. Feriancová, M. Putala, P. Nádaždy, M. Hodas, A. Shaji, V. Nádazdy, M. Huss-Hansen, M. Knaapila, J. Hagenlocher, N. Russegger, M. Zwadlo, L. Merten, M. Sojková, M. Hulman, A. Vlad, P. Pandit, S. Roth, M. Jergel, E. Majková, A. Hinderhofer, P. Siffalovic, and F. Schreiber, "Novel highly substituted thiophene-based n-type organic semiconductor: Structural study, optical anisotropy and molecular control," *CrystEngComm*, vol. 22, no. 42, pp. 7095-7103, 2020

- V. Belova, A. Hinderhofer, C. Zeiser, T. Storzer, J. Rozboril, J. Hagenlocher, J. Novak, A. Gerlach, R. Scholz, and F. Schreiber, "Structure-dependent charge transfer in molecular perylene-based donor/acceptor systems and role of side chains," *J. Phys. Chem. C*, vol. 124, no. 21, pp. 11639-1165, 2020

- G. Duva, A. Mann, L. Pithan, P. Beyer, J. Hagenlocher, A. Gerlach, A. Hinderhofer, and F. Schreiber, "Template-free orientation selection of rod-like molecular semiconductors in polycrystalline films," *J. Phys. Chem. Lett.*, vol. 10, pp. 1031, 2019

- S. Maiti, S. Maiti, A. Maier, J. Hagenlocher, A. Chumakov, F. Schreiber, and M. Scheele, "Understanding the formation of conductive mesocrystalline superlattices with cubic PbS nanocrystals at the liquid/air interface," *J. Phys. Chem. C*, vol. 123, no. 2, pp. 1519-1526, 2019

- A. Greco, A. Hinderhofer, M. Dar, A. Ibrahim, N. Arora, J. Hagenlocher, A. Chumakov, M. Grätzel, and F. Schreiber, "Kinetics of ion-exchange reactions in hybrid organic-inorganic perovskite thin films studied by in situ real-time X-ray scattering," *J. Phys. Chem. Lett.*, vol. 9, no. 23, pp. 6750-6754, 2018

- S. Maiti, A. André, R. Banerjee, J. Hagenlocher, O. Konovalov, F. Schreiber, and M. Scheele, "Monitoring self-assembly and ligand exchange of PbS nanocrystal superlattices at the liquid/air interface in real time," *J. Phys. Chem. Lett.*, vol. 9, no. 4, pp. 739-744, 2018

Danksagung

Last but not least möchte ich mir für die Unterstützung bedanken, die ich in den letzten Jahren und beim Erstellen dieser Arbeit erhalten habe. An erster Stelle danke ich Prof. Frank Schreiber für die Möglichkeit, diese Doktorarbeit in seiner Arbeitsgruppe zu verfassen, sowie die jederzeit hervorragende Betreuung.
Bei JProf. Katharina Broch bedanke ich mich für die Zweitbetreuung, sowie die Unterstützung bei diversen Strahlzeiten. Prof. Heiko Peisert danke ich sehr herzlich für das Erstellen eines zweiten Gutachtens dieser Arbeit.
Bei Dr. Alexander Hinderhofer möchte ich mich nachdrücklich für die zahlreichen wissenschaftlichen Diskussionen, seine Anregungen und Ideen und die Unterstützung beim Schreiben der Publikationen und der Arbeit bedanken. Ich hätte gerne deine Geduld und Coolness.
Prof. Steffen Duhm und Prof. Kera danke ich für das zur Verfügung stellen ihrer Labore und Geräte, außerdem für die mir entgegengebrachte Gastfreundschaft in China und Japan. Außerdem den netten Mitgliedern ihrer jeweiligen Gruppen, die mich ebenfalls sehr herzlich aufgenommen haben, zu nennen sind besonder Hu Jiaxin, Wang Qi in Soochow und Matthias Meissner und Yuri Hasegawa in Okazaki.
Der Japan Society for the Promotion of Science danke ich für das Stipendium zum Summer Programm 2019, es war eine großartige Zeit in der ich viele neue Freunde gefunden habe (Eva-san, Jana-san, Jenny-san und Jojo-san, das geht an euch).
Katharina Broch, Rupak Banerjee, Lisa Egenberger, Matthias Zwadlo, Giuliano Duva, Nadine Russegger und Daniel Lepple danke ich für ihre Unterstützung während der Strahlzeiten in England und Frankreich. Vielen Dank, dass ihr für mich die auf so viel Schlaf verzichtet habt.
Bei Aleksandra Rötschke, Susanne Kern und Hanna Maurer bedanke ich mich für die, in allen Belangen, kompetente und freundliche Unterstützung bei jeglichen Formalien und dienstlichen Angelegenheiten.
Meinen zahlreichen Bürokollegen über die Jahre: Johannes Dieterle, Alexander Hinderhofer, Valentina Belova, Giuliano Duva, Sonam Maiti, Santanu Maiti, Niels Scheffczyk, Viktoria Wedler, Lisa Egenberger, Nina Conzelmann, Ingrid Dax und Ivan Zaluzhnyy danke ich für die stets sehr freundliche, kollegiale und oft auch sehr lustige Atmosphäre. Dasselbe gilt für die gesamte Arbeitsgruppe, egal ob in Tübingen oder in Oberjoch, es war immer eine schöne Zeit.
Bei Clemens Zeiser, Madeleine Fries, Alexander Hinderhofer, Nina Conzelmann, Berthold

Reisz, Giuliano Duva, Nadine Russegger und Ingrid Dax möchte ich mich für das Korrekturlesen von Teilen dieser Arbeit bedanken.
Wenn aus Kollegen Freunde werden. Clemens Zeiser und Madeleine Fries, vielen Dank für die gemeinsame Zeit in der Arbeitsgruppe und noch viel mehr für die Zeit darüber hinaus. Der Alltag mit euch wird mir fehlen.
Ein letzter Dank geht an meine Eltern, meine Schwester und meine gesamte Familie für die Unterstützung.
An meine Partnerin Anne, vielen Dank für deine Geduld und Nachsicht in der letzten Zeit. Ich freue mich riesig auf das, was da noch kommt.